Probing the free electron density and diffusion length in dye-sensitized solar cells

Dunn, Halina

Award date:
2009

Awarding institution:
University of Bath

Probing the free electron density and diffusion length in dye-sensitized solar cells

Halina K. Dunn

A thesis submitted for the degree of Doctor of Philosophy

University of Bath

Department of Chemistry

December 2009

Abstract.

Highly time-resolved laser induced photovoltage transients have been obtained for a range of steady state background photovoltages on a 4 μm N719-sensitised DSC. The technique, first proposed by O'Regan, allows the determination of the apparent electron diffusion coefficient from the time taken for the photovoltage to rise from a steady state value as a consequence of a small extra pulse of light. We have extended the technique to measure the apparent electron lifetime and diffusion coefficient under the same operating conditions, at open circuit. This has allowed computation of the diffusion length without the need to make assumptions about the average electron density throughout the TiO_2 under short circuit conditions. The diffusion length, which was found to increase from approximately 40 to 70 microns over the range studied, was in reasonable agreement with the results of IMVS and IMPS, once the latter had been corrected for the equivalent quasi Fermi level position under open circuit conditions.

A microwave reflectivity technique, designed to probe the free electron density by measuring the conductivity in TiO_2, was developed and applied to a working DSC for the first time. This allowed simultaneous measurement of the photovoltage and conductivity as a function of light intensity. In order to cross check the validity of these measurements, modelling based on the Fresnel reflection coefficients was carried out and the conductivity was also measured directly across a *ca.* 250 μm insulating gap between two FTO electrodes. Assuming a constant electron mobility, these conductivity measurements provide an estimate of the free electron concentration, which is a key parameter in DSC modelling and characterisation, and yet has not been measured until now. These measurements have allowed us to begin to unlock some deep-rooted unknowns of DSC function, namely the well-documented, but poorly understood non-ideality in the relationship between the photovoltage and the light intensity. Finally, the microwave reflectivity technique was adapted to make preliminary measurements of the free electron density at short circuit, and frequency-resolved measurements of the apparent electron lifetime which were in good agreement with that measured by IMVS.

Acknowledgements.

First and foremost, I would like to thank my supervisor, Prof Laurie Peter, for setting me an interesting topic, and for his help and guidance throughout my PhD. I have learnt a lot over the past four years, and if Laurie has taught me anything, it's how to gut mackerel on the beach!

I would also like to thank all the members of the LMP group, past and present, for always being great company. Particular thanks go to James, Oanh, Killian and Wendy for their help when I started.

From outside the Chemistry Department, I would like to thank Prof Alison Walker, Eric Maluta and Stephen Bingham for their work on the modelling of my microwave experiments. A very special thanks goes to Stephen for being my "microwave hero" towards the end of my thesis, his insight into both experimental and theoretical aspects was invaluable. My gratitude also goes to Dr Stephen Pennock and Dr Robert Watson for diagnosing my faulty microwave detector.

Many thanks to the various people who helped me finalise this thesis, Jon, Petra and Grandad for proofreading, and Claire for her expert printing assistance! Grazie mille to Alberto for sharing the writing up experience.

Thank you to my parents, Louise and Peter, for their support and encouragement. A special thanks also goes to my "Bath parents", Trish and Tony Wilkinson, for always looking after me over the last eight years. I dedicate this thesis to the memory of Trish.

In terms of four legged creatures, I must thank Karma for keeping me sane these last few years, and I would also like to thank his associated two legged creatures, Steph, Becky and Steffi, who have been a great help.

Work done in conjunction with others.

All of the work presented in this thesis was carried out by the author apart from the following exceptions:

The modelling in Chapter 5 was carried out by Eric Maluta under the supervision of Prof Alison Walker and Dr Stephen Bingham from the Department of Physics, University of Bath.

The gap cells described in Chapter 6 were fabricated by Dr Hongxia Wang.

Table of Contents

1 Introduction 1

1.1 The need for renewable energy sources. 1

1.2 The history of photovoltaics. 1

1.3 Conventional solar cells. 2

1.4 Excitonic solar cells 5

1.5 Dye sensitised solar cells. 5

1.6 Aims of the present thesis. 7

2 Theory. 9

2.1 Basic principles of DSC operation. 9

2.2 i-V characteristics. 11

2.3 Photocurrent. 12

2.4 Thermodynamics, traps, and the quasi-static approximation. 14

2.5 Kinetic considerations and the origin of the photovoltage. 18

2.6 The continuity equation. 20

2.7 The diffusion length. 21

2.8 Frequency resolved techniques 25

3 Experimental. 27

3.1 Cell preparation. 27

3.1.1 Electrode preparation 27

3.1.2 Counter electrode preparation. 28

3.1.3 Electrolyte. 29

3.1.4 Cell construction. 29

3.2 Cell architectures for specific applications. 30

3.2.1 Laser transient experiments. 30

3.2.2 Microwave reflectivity measurements. 30

3.3 Standard characterisation techniques. 32

3.3.1 Physical properties of the solar cells. 32

3.3.2 Photovoltaic performance. 33

3.3.3 Dynamic techniques. 35

3.4 Probing the trapped electron density. 39
3.4.1 Infrared transmittance. 39
3.4.2 “Short circuit” photovoltage. 40
3.4.3 Charge extraction. 42
3.4.4 Comparison of the different methods. 43
4 Laser induced photovoltage rise time. 45
4.1 Introduction and theory. 45
4.2 Photovoltage transients. 47
4.2.1 Rise-time measurements. 47
4.3 Results and discussion 51
4.3.1 Determination of D_n by the photovoltage transient method. 51
4.3.2 Determination of D_n by the IMPS method. 53
4.3.3 Comparison of the two methods, and determination of L_n. 54
4.4 Conclusions and outlook. 57
5 Development of the microwave reflectivity technique. . 61
5.1 Introduction. 61
5.2 Microwave reflectivity 62
5.2.1 Principles. 62
5.2.2 Applications. 65
5.3 Modelling. 69
5.3.1 Theory. 69
5.3.2 Literature survey of the complex dielectric constant for the materials of interest. 71
5.3.3 Experiments performed to refine parameters. 71
5.3.4 One dimensional model. 73
5.4 First steps in microwave reflectivity on TiO_2 76
5.4.1 Microwave components. 76
5.4.2 Preliminary measurements. 78
5.5 Optimisation 82
5.5.1 Cell design. 82
5.5.2 Active area positioning and back reflection. 83
5.5.3 Improvements to the waveguide 85
5.5.4 Optimised experimental set up 86

6 Microwave reflectivity as a tool to provide further insight into the inner workings of DSCs. 91

6.1 Introduction. 91

6.2 Exploring the unexpected. 93

6.2.1 Investigating the origin of the curvature. 93

6.2.2 Estimation of the sensitivity factor. 99

6.2.3 How do the various non-idealities relate? 100

6.2.4 Non-ideality between the photovoltage and the free electron concentration. 105

6.2.5 Non-ideality between the free electron concentration and the light intensity. 109

6.3 Effect of electrolyte composition on the free electron concentration. 112

6.3.1 Effect of tert-Butyl Pyridine. 112

6.3.2 Steps towards determining the trapping/de-trapping term in the quasi static approximation. 114

6.3.3 Effect of the tri-iodide concentration. 119

6.4 Frequency resolved microwave conductivity. 121

6.4.1 Experimental set up. 121

6.4.2 Comparison with IMVS. 122

6.4.3 Possible improvements to the system. 123

6.5 Investigation of the free electron concentration at short circuit. 124

6.6 Conclusions and outlook. 126

7 Conclusions and outlook. 127

7.1 The diffusion length. 127

7.2 Conductivity measurements as a measure of the free electron density. 127

7.3 Non-ideal behaviour in DSCs. 128

8 References 131

9 Appendices. 135

9.1 Appendix A: glossary of symbols. 135

9.2 Appendix B: Parameters used in modelling in Figure 5.3.5. 137

9.3 Appendix C: Non ideality factors in Chapter 6. 139

9.4 Appendix D: Additional information on cells in chapters 4, 5 and 6. 141

1 Introduction

1.1 *The need for renewable energy sources.*

In 1957, Charles David Keeling began measuring atmospheric CO_2 levels. He noticed the average CO_2 level rose steadily, from 316 parts per million, or ppm in 1957. Since then, it has continued to rise, reaching 370 ppm in 2003. It is now broadly acknowledged that CO_2, and other so-called "greenhouse gases" are responsible for climate change.[1]

In 1998, mankind's overall energy consumption came to 12.7 TW. It has been predicted that by the year 2050, between 26.4 and 32.9 TW will be required to meet our insatiable greed for energy. If energy continues to be sourced mostly from fossil fuels, this could lead to atmospheric CO_2 levels exceeding 750 ppm, with devastating effects on ecosystems, animal species and populations throughout the globe. If this catastrophe is to be averted, production of CO_2-neutral energy is of utmost importance. There are many so-called renewable energy sources, of which the most abundant, but also the most difficult to harness, is solar energy. Indeed, the solar energy reaching the Earth's surface in one hour surpasses the yearly expenditure of energy by humankind. The challenge that now faces a section of the scientific community is to find an economically viable way to utilize this energy.[2] There are essentially three ways to harness the sun's energy. The simplest is by capturing the thermal energy, which can either be used directly for domestic use, or concentrated as a heat engine to drive a turbine to generate electricity. The second has been implemented by nature since the beginnings of life on Earth. Photosynthesis is an example of a photochemical energy converter, whereby the photon's energy is stored in the form of chemical energy. A promising example of a renewable energy source is using sunlight to drive water splitting into hydrogen which can later be used as a fuel.[3-4] Photovoltaic devices constitute the third method to harness the sun's energy.

1.2 *The history of photovoltaics.*

The term *photovoltaic* derives from the Greek word *phos* for light, and the name of the Italian physicist Volta, honouring his work on electrical potentials. Literally,

photovoltaic signifies *electricity from light*. The photovoltaic effect was discovered in 1839 by Edmund Bequerel, and in the following decades, researchers constructed various photovoltaic devices, although at the time it was photoconductivity which was of interest, for photographic applications. In the 1950s, thanks to the emergence of the silicon industry, the first silicon solar cell was fabricated, with an initial efficiency of 6%. These early solar cells were soon adopted by space projects as a source of power in satellites and spacecraft. It was not until the energy crises of the 70s that the potential of photovoltaics began to be recognised as a viable terrestrial power source.

1.3 *Conventional solar cells.*

Any atom can absorb light of frequency corresponding to the energetic separation between the electron shell levels. The key to making a photovoltaic device is to not only to absorb light of a suitable wavelength, but also to extract the promoted electrons, by building in some form of asymmetry. Silicon solar cells, which remain the most widespread photovoltaic devices, are made up of a thick (300 μm) base layer of p-type silicon, and an emitter layer, 0.3 μm of n-type silicon. The emitter layer is created on the surface of the p-type base by doping with donor impurities (e.g. phosphorus). The p-n junction formed by the juxtaposition of these different forms of silicon, with different Fermi levels, drives photo-generated holes and electrons to opposite contacts.

When an n- and a p-type semiconductor are brought into contact, electrons diffuse from the n- to the p-type material, leaving, close to the junction, a positive charge in the n-type semiconductor, and a negative charge in the p-type semiconductor. This displacement of charge results in an electric field at the junction, resulting in a force driving the holes into the p-type material, and the electrons into the n-type material. At the same time, since there is a higher density of holes in the p-type material, and electrons in the n-type material, the concentration gradient creates diffusive forces tending to drive the carriers in the opposite direction. It is the resultant force which, when multiplied by the conductivity, gives the total current. In the dark, the Fermi level is the same for holes as for electrons. Under illumination, electrons are promoted from the valence band to the conduction band, resulting in the Fermi level

for holes and electrons moving away from the equilibrium position, towards the valence and conduction bands, respectively. At the surface, recombination of holes and electrons means that the Fermi levels take on their dark equilibrium values. Since, in each material, the conductivity is highest for the majority carriers, a smaller gradient is required to drive equal densities of each type of carrier to the surface. This results in the Fermi levels at the surface being close to that of electrons in the n-type material, and close to that of holes in the p-type material. The open circuit voltage is the difference in potential between these values.[5]

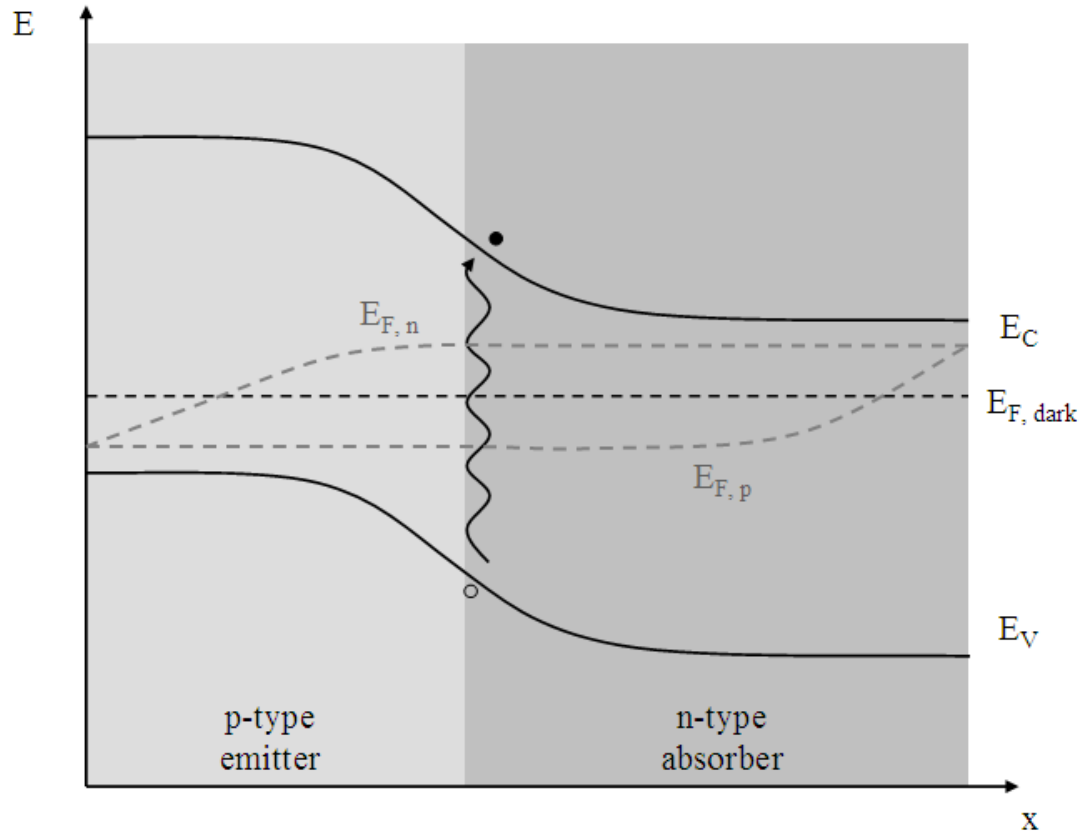

Figure 1.3.1: Schematic representation of light absorption and charge separation in an illuminated p-n junction solar cell, such as single crystal silicon at open circuit.

Despite holding one of the highest single junction efficiencies of 25%, the success of silicon as a photovoltaic material is principally due to the technological know-how as a result of its use in micro electronics. It is, in fact, a relatively poor contender for photovoltaic applications, due to its small indirect bandgap. Calculations of the maximum theoretical efficiency, based upon "detailed balance", which considers radiative losses, has found it to be 33 % at the optimal bandgap of 1.4 eV under AM

1.5 illumination.[6 5] Direct bandgaps are also favourable because the maximum of the valance band occurs at the same wave vector as the minimum in the conduction band energy, so that any photon with the energy of the bandgap or above causes excitation of a valence electron to the conduction band. In indirect semiconductors, on the other hand, the conduction band minimum and valence band maximum occur at different wave vectors, meaning that additional momentum must be simultaneously provided by phonons to promote electrons to the conduction band, making photon absorption less likely. The bandgap of a semiconductor is the first consideration in terms of its photovoltaic potential. A very small bandgap will absorb many photons of a wide range of wavelengths, but with a low photovoltage. A large bandgap, on the other hand, allows a larger photovoltage, but since only photons with energies higher than the bandgap are absorbed, the current will be lower. Since the purpose of a solar cell is to do electrical work, a compromise inherently exists between these two limiting cases.[6]

Other materials with more favourable bandgaps include gallium arsenide, copper indium, indium phosphide and cadmium telluride. Due to their better absorptive properties – namely a direct bandgap – these materials can be made much thinner, which has given the general term "thin film solar cells" to any semiconductor-semiconductor solar cell which is not based on crystalline silicon. Films are typically prepared by methods such as physical or chemical vapour deposition, or electroplating. By avoiding the high-energy, labour intensive processes required to produce single crystalline solar cells, mass-producible thin films may allow us to address the crucial issue of bringing down production costs. Of course there is a trade-off between production cost and maximum efficiency, the lower quality materials introducing defects which act as recombination centres, reducing the electron diffusion length and the lifetime, and increasing the resistivity. Because of their complex defect chemistry, most of the thin film absorber materials cannot be doped easily. Heterojunction thin film solar cells have an emitter made from a different, wider, bandgap material, for instance cadmium sulphide. The mismatch at the interface between the absorber and the emitter often creates extra recombination sites. Nonetheless, thin film solar cells with very respectable efficiencies have been fabricated for cells based on CdTe (16.7%) and $Cu(In,Ga)(Se,S)_2$ (19.4%) compared to the benchmark of single crystalline cells; Si (25%) and GaAs (26.1%)[7]. In recent

years, the focus for thin film solar cells has turned to materials which not only fulfil all the requirements of a good photovoltaic material, but are also made from abundant and non toxic elements, such as Cu_2ZnSnS_4.[8]

1.4 *Excitonic solar cells*

In conventional solar cells, free electrons and holes photogenerated throughout the bulk of the semiconductor diffuse towards the p-n junction where they are finally separated. Any solar cell in which charge carriers are formed and simultaneously injected into separate phases is known as an excitonic solar cell.[9] The term derives from the exciton, which is an excitable bound state which can diffuse to an interface between hole and electron conducting materials. There, the exciton dissociates by simultaneous injection of an electron and a hole into their respective conducting media. One way in which conventional and excitonic solar cells apparently differ is that the open circuit voltage, V_{oc} of a conventional cell is limited to the built in voltage, whereas in excitonic solar cells, photovoltaic activity is possible in the absence of a built in voltage. This is simply due to the fact that charge separation in any solar cell is driven by the combination of two opposing forces, caused by the gradient in electrical and chemical potential energies. Due to the large kinetic asymmetry at the junction between the hole and electron conducting materials in some excitonic solar cells, efficient charge separation can be achieved without any electrical asymmetry. Better photoconversion can be achieved by coating the contacts in order to enhance carrier-selectivity. For instance, an electron-selective contact should not be oxidised by the absorber material. Examples of excitonic solar cells include molecular semiconductor solar cells, conducting polymer solar cells and dye sensitized solar cells.[9] The dye sensitised solar cell, or DSC, stands out from other excitonic solar cells, as excitons are created within a single monolayer of dye, which is both thin and immobile, meaning that exciton recombination does not tend to be a limiting factor.

1.5 *Dye sensitised solar cells.*

The idea of using a pigment to absorb light in a solar cell can be traced to the 1980's[10-11], and in 1991, Grätzel and O'Regan published a paper announcing a solar

cell made of a high surface area dye-sensitized TiO_2 electrode. For a 10 μm thick film consisting of 15 nm particles sensitized with dye, an overall conversion efficiency exceeding 7 % was obtained.[12]

The photoactive component of a DSC is a monolayer of dye, typically ruthenium 535-bisTBA, or N719, adsorbed to the surface of an array of interconnected TiO_2 nanoparticles, of typical diameter 10-30 nm. A liquid electrolyte, typically containing the I^-/I_3^- redox couple, interpenetrates this network, allowing reduction of the oxidised dye molecule by I^-. It is the most successful example of an excitonic solar cell, and thanks to a liquid electrolyte typically acting as the hole conductor, has the highest internal surface area. This allows just a monolayer of dye to absorb the incident light strongly, while allowing efficient charge separation. The large internal surface area also introduces more scope for back reaction of electrons in the TiO_2 with oxidised species in the electrolyte, but thanks to a remarkably well suited redox couple, I^-/I_3^-, this reaction is sufficiently slow to allow films to be made thick enough for efficient light harvesting, without compromising on the collection efficiency.

Despite having continued to attract a great deal of interest since their introduction in 1991,[12] relatively small improvements to the efficiency of DSCs have been made, which now stands at 11 %.[7] With the commercial prospects of DSCs beginning to materialise, in particular for low power, light weight applications, the need to further improve cell performance is more critical than ever. There have essentially been two approaches to improving the cell efficiency. The most obvious, and the one which has lead to most advances, has been to tinker with the cell composition. Almost every component of the cell has been investigated, leading to various optimised combinations. The other, more fundamental approach, is to develop a detailed understanding of the complexities of DSC operation, in the hope that this will enable educated changes, which should lead to greater improvements.

1.6 *Aims of the present thesis.*

The main component of the dye sensitised solar cell under study here is the nano-porous TiO_2 film. The electron diffusion length – an important parameter which places an upper limit on how far the light harvesting efficiency can be improved by increasing the film thickness – is studied by two dynamic techniques in chapter 4. A technique first proposed by O'Regan[13] *et al.* relies on the time taken for the photovoltage to rise from a steady state value following a short pulse of light to obtain the apparent electron diffusion coefficient, a parameter needed for the calculation of the diffusion length. The method is based upon the RC time constants for discharging the TiO_2 chemical capacitance and charging the substrate capacitance. Since the measurement is carried out at open circuit, both the apparent electron lifetime and diffusion coefficient are obtained under the same conditions, and can therefore be meaningfully used to calculate the diffusion length. The results of this method are found to be similar to the result of intensity modulated photocurrent, and photovoltage spectroscopies, IMPS and IMVS. These methods are routinely used to obtain the apparent electron diffusion coefficient and lifetime, and can be used to compute the diffusion length provided they are performed at the same electron quasi Fermi level.

Perhaps the most exciting part of this work has been an attempt to measure the free electron density by microwave reflectance studies. This method, which has been widespread for the measurement of minority carriers in semiconductors for several decades, is based upon the measurement of changes in reflected power, ΔP_r, as a result of a change in conductivity, $\Delta\sigma$, according to;

$$\frac{\Delta P_r}{P_r} = S\Delta\sigma$$

1.6.1

This expression, in which S is a sensitivity factor, is expected to be linear for small changes in conductivity. Although never performed on a working DSC, time resolved microwave reflectance, TRMC, has been performed on isolated nano-porous TiO_2. Here, the technique has been applied to a working DSC, allowing the change in reflectivity to be monitored simultaneously with the photovoltage over a range of incident light intensities. Due to the experiments being carried out on a

working DSC, no attempts were made to enclose the sample within the microwave waveguide, as was the case in most previous studies. This inherently complicates the measurement, due to leakage of the field around the edges of the sample. A collaboration with the group of Professor Alison Walker and Dr Stephen Bingham has attempted to determine a value for the sensitivity factor in expression 1.6.1. This has proven problematic, firstly because certain simplifications, which can be made if the sample is enclosed in a waveguide, could not be made in this case due to the experimental arrangement, and secondly because the changes in conductivity were large, meaning that S was not a constant over the range of light induced conductivities studied. In spite of this, some interesting observations have been made, not least that the free electron concentration does not seem to behave in accordance with the expectations based on the accepted current understanding of DSCs, which will be discussed in detail in chapters 2, 5 and 6. However this non-ideal behaviour has been found to be intimately related to the well-documented deviation from ideality found in the relationship between photovoltage and light intensity, and helps to further our understanding of it. Finally the technique has been modified to allow measurement of the electron lifetime using a frequency resolved technique, and preliminary measurements have been carried out on a cell at short circuit, although no firm conclusions have been reached due to time limitations.

2 Theory.

2.1 *Basic principles of DSC operation.*

The photoactive component of a DSC is a monolayer of dye, typically $[RuL_2(NCS)_2]$: 2 TBA, commonly known as N719, where L=2,2'-bipyridyl-4,4'-dicarboxylic acid and TBA=tetra-n-butylammonium, adsorbed to the surface of an array of interconnected TiO_2 nanoparticles, of typical diameter 10-30 nm. A liquid electrolyte containing the I^-/I_3^- redox couple interpenetrates this network, allowing reduction of the oxidised dye molecule by I^-. Under short circuit conditions, electrons diffuse to the FTO back contact, where they are extracted. Electrons re-enter the cell via a platinised FTO counter electrode and reduce I_3^-. Under open circuit conditions, electrons are lost to recombination with I_3^- via the mesoporous TiO_2 or the FTO. The sequence reaction of TiO_2 electrons with I_3^- is thought to be[14]:

$$e^- + I_3^- \rightarrow I^- + I_2^{-\bullet}$$

2.1.1

followed by:

$$e^- + I_2^{-\bullet} \rightarrow 2I^-$$

2.1.2

or;

$$2I_2^{-\bullet} \rightarrow I^- + I_3^- .$$

2.1.3

Recently, Rowley and Meyer[15] have reported that they have found no evidence that TiO_2 electrons interact with the iodine radical, implying that equation 2.1.3 may be the more likely second step.

Figure 2.1.1 illustrates the main electron transfer processes in a DSC. Electrons are injected into the TiO_2 conduction band with a rate υ_{inj} – 1, after which they are involved in trapping – 3 and thermal de-trapping – 4, or are lost to reaction via the oxidised dye – 5, or to I_3^- in the electrolyte with a rate of $\upsilon_{I_3^-}$ – 6. Those electrons

that are not lost via these pathways will diffuse in between trapping and de-trapping events towards the FTO contact with a diffusion constant, D_0 – 2. The photovoltage in any solar cell is defined as the difference in electric potential between two external contacts of the same material (eg copper). In the case of a DSC, the FTO contact constitutes the anode, in which the electric potential is equivalent to the quasi Fermi level in the TiO_2, which is the energy level of the highest filled trap state. The cathode is the platinised FTO, which is at equilibrium with the electrolyte at open circuit, while at short circuit, a small potential drop, or over potential, is expected between the cathode and the electrolyte redox level. Hence the photovoltage is defined as the difference in energy levels between the quasi Fermi level and the redox Fermi level of the electrolyte.

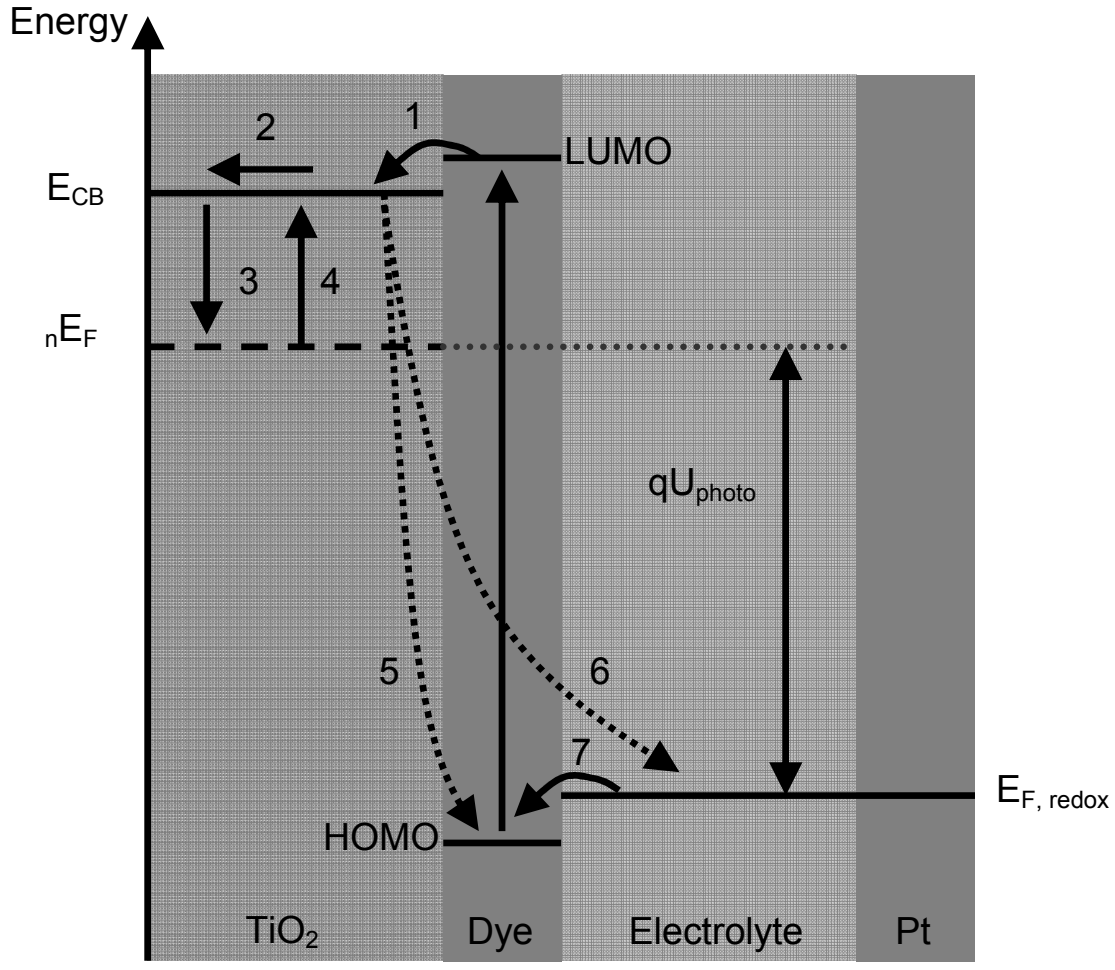

Figure 2.1.1: Kinetic processes occurring in a DSSC.

2.2 *i-V characteristics.*

For any solar cell, the aim is to convert the power carried by the incident photons into useful electrical power. When the two contacts are connected by a negligible external load, the cell is said to be at short circuit, and the current flowing in the external circuit is known as the short circuit current. When the contacts are connected via an infinite load, the cell is at open circuit, and the build up of photogenerated electrons leads to the open circuit voltage between the two terminals. If the load resistance is reduced, current begins to flow in the external circuit, and the voltage between the contacts drops as a result. Thus, by changing the load resistance, values of voltage and current can make up an current voltage curve. The power delivered at any given load resistance can be calculated, with the maximum power point being of particular practical interest, the corresponding current and voltage are I_m and V_m, respectively. The efficiency of the cell is equal to the ratio of the maximum output power to the incident solar power, P_{in}. The standard incident solar power, AM 1.5 is defined to be 100 mWcm^{-2}.

$$\eta = \frac{V_m I_m}{P_{in}}$$

2.2.1

The current begins to drop off as the cell approaches open circuit and the fill factor is a measure of how "square" the *i-V* curve is. The fill factor is defined as;

$$FF = \frac{V_m I_m}{V_{OC} I_{SC}}$$

2.2.2

Rearranging equations 2.2.1 and 2.2.2, the routinely used expression for the overall cell efficiency is found;

$$\eta = \frac{V_{OC} I_{SC} FF}{P_{in}}$$

2.2.3

As can be seen from equation 2.2.3, the overall efficiency of a device can be improved by increasing the fill factor, open circuit voltage or short circuit current. Reductions in the fill factor are caused mostly by series resistance in the conductive glass contacts. Broadly speaking, the short circuit current can be increased by improving light harvesting, either by increasing the film thickness, dye coverage or the extinction coefficient of the dye. The open circuit voltage is defined as the

difference in energy level between the quasi Fermi level and the redox potential of the electrolyte. Typically, improvements are achieved by altering the composition of the electrolyte, for instance by the addition of tert-butyl pyridine (t-BP) which is understood to raise the conduction band of the TiO_2.

Figure 2.2.1 shows an *i-V* curve for a cell investigated as part of the microwave reflectivity study. The cell has an efficiency of 2.9 % at one Sun, and has a modest fill factor of 0.43. It should be noted that these cells were not optimised for performance, due to experimental requirements for thin glass substrates, 15Ω/□ glass was used, which significantly increases the series resistance.

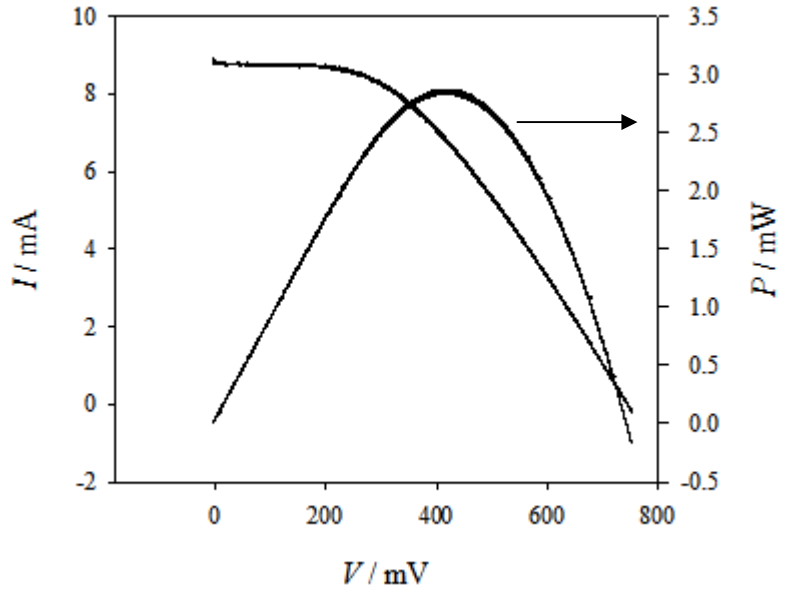

Figure 2.2.1: Measured i-V characteristics of cell 21, as part of the microwave reflectivity study in chapter 6.

2.3 *Photocurrent.*

A measure of the light harvesting ability of a solar cell is its incident photon to electron conversion efficiency, or IPCE. It can be expressed as the product of the efficiencies of light harvesting, electron injection and electron collection.

$$IPCE = \eta_{LH} \times \eta_{inj} \times \eta_{col}$$

2.3.1

For a non-scattering film, the light absorption profile across the film, which can be expressed by the Beer-Lambert law, is integrated to quantify the light harvesting efficiency of the cell, based on the film thickness and the dye absorption coefficient.

$$\eta_{LH} = 1 - e^{-\alpha(\lambda)d}$$

2.3.2

The electron injection efficiency, η_{inj}, refers to the injection of electrons from the excited dye molecule to the TiO_2 conduction band, and it has recently been found by Koops [16] to depend on the energy difference between the LUMO of the dye, and the TiO_2 conduction band, which can be adjusted by the addition of additives to the electrolyte, such as t-BP and Li^+ ions. Furthermore, the same study suggests that the injection efficiency can change with the potential of the cell, indicating that injection from the dye into unoccupied trap states might also be possible. Based on the similarity between the various electrolytes used in this study, and those reported in the publication, the injection efficiency is expected to range from 0.78 to 0.97.

Finally the collection efficiency, or η_{col}, is the efficiency of electron collection at the contact, and is related to the electron diffusion length. Recently, a method which finds the collection efficiency to be related to the ratio of the light intensity needed to maintain the same total electron density under short and open circuit conditions, has been proposed by Jennings, and was also used by Wang and Peter[17]. In this publication, the collection efficiency for a Li-based electrolyte was 0.97. When the same approach was applied to the cells used in the microwave study, values of 0.9-0.96 were found.

Since the *IPCE* is a measure of a solar cell's photocurrent-response at a given wavelength, integrating the product of the *IPCE* and the solar spectrum can be used to predict the short circuit current. This calculation was performed on the *IPCE* spectrum shown below, and yielded a value of 7.12 $mAcm^{-2}$. This is in reasonable agreement with the short circuit current measured in the *i-V* curve shown in Figure 2.2.1. the discrepancy is probably due to there being further absorption at wavelengths below 400 nm which has not been accounted for in the *IPCE*. Also the *IPCE* was measured without bias illumination, and it has been found that the *IPCE* can be underestimated at lower light intensities. This has been observed in our laboratory, and Barnes[18] *et al.* have shown that the diffusion length measured by the *IPCE* method, described later in this chapter, also increases with light intensity.

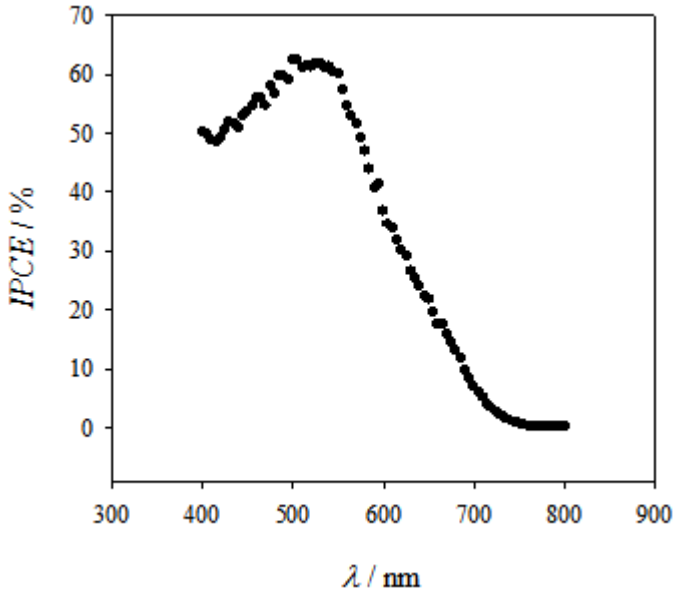

Figure 2.3.1: IPCE spectra for front side illumination for cell 21, which was part of the microwave reflectivity study in chapter 6.

2.4 *Thermodynamics, traps, and the quasi-static approximation.*

The band gap of the TiO_2 matrix appears to contain many trapping sites. The evidence for this was first seen in attempts to measure the lifetime of electrons in the conduction band. Contrary to expectations, the time scale of the response to the initiation or the cessation of illumination was found to change with the illumination intensity. This was first of all interpreted as an indication that the reaction of electrons with I_3^- was not first order in electron concentration[19]. However, this was later explained by the presence of inter-bandgap states. When an electron is injected, it will fall into a trapping state if it comes across one, and can only be released thermally. Therefore the transit time of electrons across the TiO_2 is slowed by the effect of trapping. Likewise, once in a trap, the electron must be thermally released before it can recombine with I_3^-, unless it is within tunneling distance from the interface between the TiO_2 and the electrolyte. Therefore the traps act as a buffer, slowing all processes of transport and recombination. At steady state, however, since most trapping states up to the quasi Fermi level are filled, transport and recombination are not affected by trapping. This was elegantly formulated mathematically by Bisquert and Vikhrenko[20] in the quasi-static approximation. Furthermore the charge extraction technique [21-22] allows the distribution of traps to

be measured. The cell is held at open circuit under illumination, and the total charge at open circuit is abruptly extracted as the cell is short circuited while the illumination is simultaneously ceased. The resulting current spike is integrated to give the total charge stored at a given photovoltage. By repeating this process at a range of starting photovoltages, and given that the vast majority of electrons are trapped, it is found that the trapped electron density varies exponentially with photovoltage.

The traps' exact location is not known, although it is thought that they are situated close to the surface. In a study by Kopidakis [23] *et al.*, in which a range of TiO_2 pastes were prepared with constant porosity, but varying roughness factor, the trap density was found to scale with the roughness factor. This led the authors to the conclusion that the traps are located close to the surface, since the trap density scales with surface area. If the traps were located in the bulk of the TiO_2, the density of traps would not change in the different pastes, due to the constant porosity. Recently, Bisquert [24] *et al.*, have suggested that there may in fact be two categories of traps, those in the bulk, from which electron are thermally released to the conduction band before recombining, and those on the surface, from which electrons can recombine directly with the oxidised redox species in the electrolyte. This argument has been put forward as an explanation for the variation of L_n with electron density, due to the free electron lifetime not being constant, as a result of the back reaction not occurring solely via the conduction band. This point will be revisited in section 2.7.

The behaviour of electrons in the TiO_2 matrix is described by Fermi-Dirac statistics. The probability of an electron occupying a given energy level is given by;

$$f(E) = \frac{1}{\exp\left(\frac{E - E_F}{k_B T}\right) + 1}.$$

2.4.1

When $1 << \exp\left(\frac{E - E_F}{k_B T}\right)$, which is valid when $k_B T << E - E_F$, corresponding to non-degenerate conditions, this reduces to;

$$f(E) = \exp\left(-\frac{E - E_F}{k_B T}\right).$$

2.4.2

The electron density is related to the probability of electron occupancy and the density of electron trap states function, *g(E)*, by;

$$n = \int_{E_{F,redox}}^{{}_nE_F} f(E)g(E)dE$$

2.4.3

Note that in the forthcoming discussion, the Fermi level, E_F is replaced by the *quasi*-Fermi level, ${}_nE_F$, because under illumination, the system is not in true thermodynamic equilibrium. Instead, it is said to be at constrained equilibrium or photostationary state, meaning that the quasi Fermi level is different from the equilibrium value, which in this case is the redox potential. If the constraint, which could either be an external bias or illumination, is removed, then the system will return to the equilibrium value.

Since the experimentally measured density of trapped electrons is an exponential function of the photovoltage, the density of states must also be an exponential. The density of trapping states can be fitted to a function of the form;

$$g(E) = \frac{\beta N_t}{k_B T} \exp\left(\frac{\beta(E - E_C)}{k_B T}\right)$$

2.4.4

To calculate the density of trapped electrons, the integral in equation 2.4.3 must be performed. This can either be done numerically or analytically by applying the zero Kelvin approximation, meaning that all states up to the quasi Fermi level are occupied, and all those above are empty. The analytical solution is given by;

$$n_t = N_t \exp\left(\frac{\beta({}_nE_F - E_C)}{k_B T}\right)$$

2.4.5

A comparison has been made between the two methods to calculate n_t, using, as parameters; $\beta = 0.29$, which describes the broadening of the trapping state distribution, the spatial trap density, $N_t = 10^{19} cm^{-3}$, and the temperature $T = 300K$.

The numerical integration yields values of n_t which slightly exceed the analytical solution. This is a result of the zero Kelvin approximation, since there are in fact more occupied states above the Fermi level than un-occupied stated below it, as a consequence of the exponential distribution of trapping states.

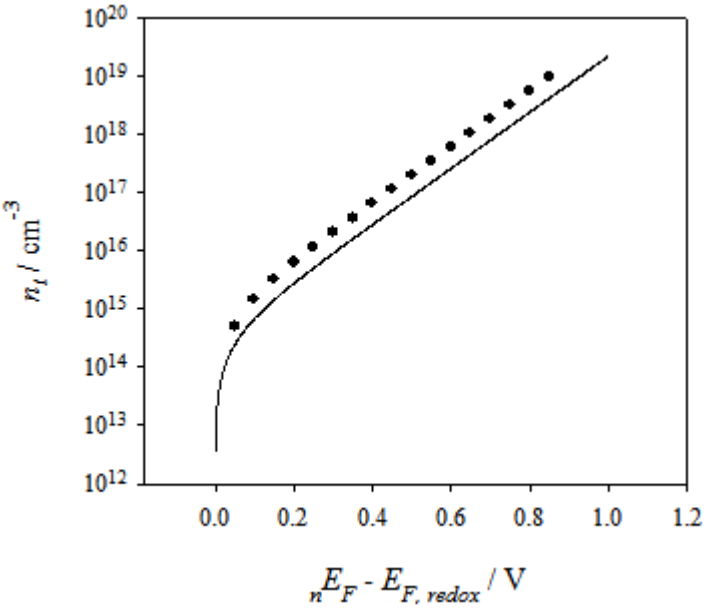

Figure 2.4.1: Trapped electron density calculated numerically for T = 300 K, filled symbols, and analytically, assuming a temperature of zero Kelvin, solid line.

Similarly, the electron density in the conduction band is found by integrating the product of the density of conduction band states and the Boltzmann distribution function, as in equation 2.4.3, between the bottom and the top of the conduction band. The conduction band electron density becomes[25];

$$n_c = N_c \exp -\left(\frac{E_c - {}_nE_F}{k_B T}\right)$$

2.4.6

where N_c is the effective conduction band density of states, which reflects the fact that the electrons do not behave as if they were in a free electron gas, which is accounted for by assigning them with an effective mass, m_n^*;

$$N_c = 2\left(\frac{2\pi m_n^* k_B T}{h^2}\right)$$

2.4.7

As was discussed above, traps have a marked effect on the electron lifetime and transport. It is therefore necessary to unravel the effects of trapping on transport and lifetime, from the "free" electron lifetime and diffusion coefficient. First of all, at steady state, the free and trapped electron densities must be at equilibrium, determined by the trapping and de-trapping rates. Furthermore, Bisquert and Vikhrenko suggested that after a small perturbation, the rate of change of trapped and free electron densities will be related as follows:

$$\frac{\partial n_t}{\partial t} = \frac{\partial n_t}{\partial n_C}\frac{\partial n_C}{\partial t}$$

2.4.8

This is known as the quasi-static approximation. Physically, it means that after a small perturbation, say an increase in light intensity, n_c will increase. As a result, $\partial n_c / \partial t$ will take some value, as will $\partial n_t / \partial t$, as extra conduction band electrons become trapped. The value of $\partial n_t / \partial n_c$ will then adjust to maintain the equality. The significance of Bisquert and Vikhrenko's work [20] is that it simplified the multiple trapping model, in which electrons go through trapping and de-trapping events, only contributing to the diffusion current when they are in the conduction band, and by applying the quasi-static approximation, reduced it to a simpler diffusion model, which accounts for trapping/de-trapping.

2.5 *Kinetic considerations and the origin of the photovoltage.*

The photovoltage in a DSC is the difference in energy levels between the quasi Fermi level in the TiO_2, and the redox potential of the electrolyte. The build up of electrons under open circuit conditions is limited by back reaction of electrons with I_3^- present in the electrolyte, or recombination with D^+, and a steady state is reached when the rate of electron injection is balanced by the rate of electron back reaction. Back reaction via D^+ tends to be considered a negligible effect, due to the high concentration of I^-, which efficiently regenerates the oxidised dye molecule.

The local electron injection rate is the product of the light profile across the film, the extinction of the dye, and the injection efficiency;

$$\upsilon_{inj}(x,\lambda) = \eta_{inj}\alpha(\lambda)I_0 \exp(-\alpha(\lambda)x)$$

2.5.1

An average injection rate across the film can be defined as the ratio of the short circuit electron number density (that the cell would have at the same light intensity) to the thickness of the film:

$$\upsilon_{inj}(\lambda) = \frac{\eta_{inj}\eta_{col}\eta_{LH}I_0}{d} = \frac{\eta_{inj}\eta_{col}I_0(1-\exp(-\alpha d))}{d}$$

2.5.2

At open circuit, since the system is in a stationary state, this rate of injection must balance the rate of back reaction via I_3^-, which, provided it is assumed to be pseudo 1st order in electron concentration, is given by;

$$\upsilon_{I_3^-} = k_{I_3^-} n_C n_{I_3^-} = \frac{n_C}{\tau_0}$$

2.5.3

This balance of injection and back reaction leads to an expression for the free electron concentration based on the incident light intensity – which is valid if back reaction is 1st order in electron concentration:

$$n_C = \frac{\eta_{inj}\eta_{col}I_0\tau_0(1-\exp(-\alpha d))}{d}$$

2.5.4

Fundamentally, the photovoltage of any solar cell is the potential difference between two external contacts of the same material. This amounts to the difference between the redox Fermi level at the anode, and the quasi Fermi level at the cathode.

$$qU_{photo} = {}_nE_F - E_{F,redox} = (E_C - E_{F,redox}) - (E_C - {}_nE_F).$$

2.5.5

Similarly to equation 2.4.6, the dark electron concentration can be written;

$$n_C^0 = N_C \exp\left(-\frac{E_C - E_{F,redox}}{k_B T}\right).$$

2.5.6

Together, equations 2.4.6, 2.5.4, 2.5.5 and 2.5.6 lead to:

$$qU_{photo} = k_B T \times \ln\frac{n_C}{n_C^0} = k_B T \times \ln\frac{\eta_{inj}\eta_{col}\tau_0 I_0(1-\exp(-\alpha d))}{n_C^0 d}$$

2.5.7

Since the only variable in the RHS of equation 2.5.7 is the light intensity, plots of the photovoltage versus light intensity should have a slope of 59 mV/decade of light intensity at 298 K. However, this is very rarely the case, with most cells exhibiting slopes of 70-120 mV/decade. This suggests that the photovoltage depends on the light intensity according to an equation of the form:

$$qU_{photo} = mk_B T \times \ln(I_0) + C$$

2.5.8

where the empirical factor, *m*, typically ranges from 1.2 to 2, and C is a constant. The origin of this non-ideality is not formally known, but it is mathematically consistent with either;

- The inclusion of m in the Boltzmann distribution function, which corresponds to non ideal electron statistics:

$$n_c = N_c \exp -\left(\frac{E_c - {}_n E_F}{mk_B T} \right)$$

2.5.9

- A shift in the conduction band position relative to the redox Fermi level of the electrolyte under operation.
- Back reaction of TiO_2 electrons with I_3^- not being 1st order in electron concentration, i.e. $n_c \propto I_0^m$.

2.6 *The continuity equation.*

Due to the high concentration of ionic species in the electrolyte interpenetrating the TiO_2 matrix, it is thought that there is no net electric field across the film. Instead, transport of electrons is believed to occur by diffusion of carriers down the concentration gradient. At steady state, provided back reaction is first order in electron concentration, the balance of fluxes in and out of any volume element in the film is given by[26];

$$\frac{\partial n_C}{\partial t} = \eta_{inj} \alpha(\lambda) e^{-\alpha(\lambda)x} I_0 + D_0 \frac{\partial^2 n_C}{\partial x^2} - \frac{n_C}{\tau_0} = 0$$

2.6.1

The first, second and third terms of the continuity equation correspond to electron generation, transport and back reaction, respectively. In order to solve this equation

for the free electron concentration, two boundary conditions are required. Firstly that electrons are not able to exit the TiO_2 via the electrolyte side of the film,

$$\left.\frac{\partial n_C}{\partial x}\right|_{x=d} = 0$$

2.6.2

and secondly that the flux of electrons extracted at the FTO contact is equal to the flux of electrons diffusing towards the contact from the film.

$$-D_0 \left.\frac{\partial n_C}{\partial x}\right|_{x=0} = k_{ext}\left(n_C - n_c^0 \exp\left(\frac{qU}{k_B T}\right)\right)$$

2.6.3

Adjusting this second boundary condition allows $n_c(0)$ to be calculated for the whole range of potentials, from open circuit, where $U=V_{OC}$ to short circuit where $U=0$. Since the current density out of the cell is simply the rate of change in the charge density with time, this can be found for all bias potentials between 0 and V_{OC}, thus predicting the *i-V* characteristics of the cell.

2.7 *The diffusion length.*

Equation 2.3.2 suggests that the light harvesting efficiency can be improved simply by increasing the film thickness. However, this will be at the detriment of the collection efficiency once the film thickness is comparable to the average distance travelled by an electron before it is lost to recombination. This parameter is known as the diffusion length, and there are various methodologies which allow its estimation.

Fundamentally, the diffusion length is determined by the electron diffusion coefficient, D_0, and – for recombination that is 1st order in electron concentration – the electron lifetime τ_0, in the TiO_2 conduction band as:

$$L_n = \sqrt{D_0 \tau_0}$$

2.7.1

However, neither the free electron lifetime or diffusion coefficient are accessible directly, due to the effects of trapping and de-trapping. By application of the quasi static approximation, an effective diffusion coefficient is defined:

$$D_n = D_0\left(1+\partial n_T/\partial n_C\right)^{-1}$$

2.7.2

Similarly, the effective electron lifetime is found to be:

$$\tau_n = \tau_0\left(1+\partial n_T/\partial n_C\right)$$

2.7.3

In order to utilise τ_n and D_n to calculate L_n, the $\partial n_T/\partial n_C$ term must be the same in both cases. This requires that both D_n and τ_n be measured at the same quasi Fermi level position[20, 26]. However, D_n is obtained from intensity modulated photocurrent spectroscopy (IMPS) at short circuit, whereas τ_n is measured at open circuit, either by photovoltage decay or intensity modulated photovoltage spectroscopy, IMVS. Thus it is necessary to relate short circuit-measured D_n to an effective quasi Fermi level in order to calculate L_n. This can be done by comparing the charge stored under open and short circuit conditions. Nevertheless, it is preferable to measure D_n and τ_n directly under the same conditions, which is made possible by measuring the rise time of a small perturbation in photovoltage, which is related to the diffusion coefficient. This method will be the focus of Chapter 4.

As well as dynamic methods, such as those noted above, several steady state methods also exist. A method which relies on the comparison of the *IPCE* spectra measured with illumination from both directions was first proposed by Sodergren *et al.* [27] and has recently been revisited by Halme *et al* [28] and Barnes *et al* [18, 29]. The method involves isolation of the contribution of the light harvesting efficiency from equation 2.3.1, defining the absorbed photon to electron conversion efficiency, *APCE*, as:

$$\frac{IPCE}{\eta_{LH}} = APCE = \eta_{inj}\eta_{col}$$

2.7.4

Although η_{LH} is simply given by the Beer-Lambert law, it requires careful measurements to account for reflections at the various interfaces, absorption by the different phases, and light scattering effects in the TiO_2. Once η_{LH} has been suitably estimated, there are two methodologies to de-convolute η_{LH} and $\eta_{col,}$ which ultimately allow an estimation of the diffusion length. Solution of the continuity

equation for front or rear side illumination yields relationships between η_{col} and L_n in each condition, which can be simplified to:

$$\eta_{col} = \frac{\tanh(d/L_n)}{d/L_n}$$

2.7.5

for uniform illumination (i.e. weak absorbtion) irrespective of illumination direction. For strong absorbtion, η_{col} is dependant on illumination direction, and for front side illumination, it is expected to be unity. For illumination from the rear side, it can be approximated by;

$$\eta_{col} = \frac{1}{\cosh(d/L_n)}$$

2.7.6

In the first method, it is assumed that η_{inj} is independent of the position within the film, and that η_{col} is unity in the limit of a infinitesimally small film thickness. Hence, in this limit, the *APCE* simply reduces to η_{inj}, so if various cells are made with a range of thicknesses, linear extrapolation to $d = 0$ allows η_{inj} to be determined, which can subsequently be used to calculate η_{col} for the thicker films. A cross check to this method is to study the effect of illumination direction, whereby if a film is thin enough that there is no change in *APCE* between illumination from the photo electrode or the counter electrode, this implies that η_{col} is unity, and the *APCE* is simply equal to η_{inj}. Once these efficiencies have been determined, the diffusion length can be calculated by either equation 2.7.5 or 2.7.6.

The second method involves measurement of the *APCE* from both illumination directions, and making use again of the assumption that η_{inj} is independent of the illumination direction. The ratio of the *APCE* measured in both directions is then equal to the ratio of η_{col} from both illumination directions, which is derived from the solution to the continuity equation for each illumination direction:

$$\frac{APCE_{FS}}{APCE_{RS}} = \frac{\eta_{col,FS}}{\eta_{col,RS}} = \frac{\sinh(d/L_n) + L_n\alpha(\lambda)\cosh(d/L_n) - L_n\alpha(\lambda)\exp(-\alpha(\lambda)d)}{\sinh(d/L_n) - L_n\alpha(\lambda)\cosh(d/L_n) + L_n\alpha(\lambda)\exp(-\alpha(\lambda)d)} \cdot \exp(-\alpha(\lambda)d)$$

2.7.7

The experimentally obtained ratio of *APCE* from each illumination direction is fitted to the RHS of equation 2.7.7, with L_n as the only free parameter. From the result of this analysis, η_{col} and η_{inj} can then be found. However, it must be noted that since this method relies on solving the continuity equation, it is implicitly assumed that back reaction is 1st order in electron concentration.

Another steady state method, proposed by Jennings and utilized by Wang and Peter[17], derives the collection efficiency from expressions for the balance of fluxes at open and short circuit. At short circuit, the flux of electrons being generated is balanced by the flux of electrons extracted, j_{SC}, and recombining, j_{rec};

$$\eta_{inj}\eta_{lh}I_{SC}T_{sub} = j_{rec} + j_{SC}$$

2.7.8

The collection efficiency can be defined as the ratio of electrons being extracted from the cell to those generated within;

$$\eta_{col} = \frac{j_{SC}}{\eta_{inj}\eta_{lh}I_{SC}T_{sub}}$$

2.7.9

Rearranging equation 2.7.8 and substitution into equation 2.7.9 leads to;

$$\eta_{col} = 1 - \frac{j_{rec}}{\eta_{inj}\eta_{lh}T_{sub}I_{SC}}$$

2.7.10

Provided j_{rec} only depends on the average electron concentration, which will only be the case if back reaction with I_3^- is 1st order in electron concentration, it will take the same value at short circuit, at light intensity I_{SC}, as it will under open circuit conditions, at a light intensity I_{OC} which maintains the same average electron concentration, hence:

$$\eta_{col} = 1 - \frac{I_{OC}}{I_{SC}}$$

2.7.11

The diffusion length can then be calculated in the same way as in the *APCE* method, based on the collection efficiency. This, rather elegant method, has the advantage of requiring very simple data analysis, and since the calculation of η_{col} is based on the ratio of experimentally measured light intensities, any systematic errors will cancel, and there is no need to measure the substrate transmission of the sample, which can

be problematic. The injection efficiency can also be found based on the measured η_{col} and an estimated η_{LH}.

In summary, several methods exist to determine the diffusion length, the agreement between which is discussed at the end of Chapter 4. However, it is important to note that both steady state methods rely on the back reaction of TiO_2 electrons with I_3^- being 1st order. The validity of this assumption is questionable, for instance, as a consequence of the experimental observation of non-ideal photovoltage dependence on light intensity. Recently, Bisquert[24] *et al.* have suggested that back reaction could occur via an exponential distribution of surface states, which would result in a non unity reaction order. However, the model relies on many parameters; for instance the distribution of surface states, and the reorganisation energy of the redox species to which the electron transfer would take place. It is therefore impossible, with the experimental evidence available, to draw any firm conclusions as to the origins of the apparent reaction order.

2.8 *Frequency resolved techniques*

A useful way to probe time constants in solar cells is with the use of frequency resolved techniques. These techniques involve applying a modulation of increasing frequency, and measuring a suitable parameter, which has an AC component as a result of the modulation. The different techniques used in this work are listed in Table 2.1.

Table 2.1: Summary of frequency resolved techniques used in the present thesis.

Technique	Modulated parameter	Measured parameter	Allows measurement of:
IMPS	Light intensity	Photocurrent	Apparent electron diffusion coeffcient
IMVS	Light intensity	Photovoltage	Apparent electron lifetime
EIS	Applied potential	Current	Chemical capacitance of TiO_2

Frequency resolved microwave reflectivity	Light intensity	ΔP_R	Apparent electron lifetime

For each frequency, the resulting response from the cell will have a magnitude, and will differ from the external stimulus by a phase difference. As the frequency increases, the phase difference tends to become more pronounced, and the magnitude of the measured parameter smaller and smaller, as the system becomes less and less capable of keeping up with the modulated stimulus. For each frequency, pairs of magnitudes and phase differences can be plotted in polar coordinates. In the case of a simple 1st order response, the frequency at which the imaginary component is minimum corresponds to the inverse of the time constant under study.

3 Experimental.

3.1 *Cell preparation.*

3.1.1 Electrode preparation

The glass used was fluorine doped tin oxide, or FTO, from Pilkington, or ASAHI in the case of the cells prepared for chapter 6, with a conductivity of 15 ohms per square. It was cut into 6 x 2.5 cm strips, which were cleaned by sonnication for 15 minutes in a sequence of solvents; decon 5%, de-ionised water, absolute ethanol, twice in iso-propanol, and ethanol. The slides were stored in ethanol until they were required, at which point they were dried using a flow of nitrogen gas.

A titanium dioxide blocking layer [30] was then applied to an area 1.5 cm wide along the edge of the long side of the slide by spray pyrolysis of a 0.2 M solution of titan(IV)bis(acetylacetonato)-diisopropylate in isopropanol (HPLC grade). The diagram below illustrates the arrangement needed to carry out the spray pyrolysis procedure. A microscope slide base is placed on a hot plate at 450^{o}C, onto which the strip of glass to be coated (conducting side up) and another strip of TEC glass are placed. Another microscope slide is positioned on top of the TEC glass, to act as a mask over the area which is not to be sprayed. This is left for 5 minutes to allow the glass to reach the temperature of the hot plate. The two spots indicate where the spray is aimed. The spray nozzle is held about 10 cm from the surface of the glass and two sprays are directed at both spots in turn. This process is repeated every 10 seconds for 2½ minutes.

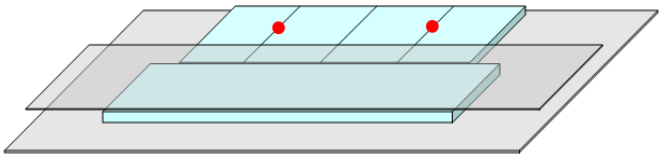

Figure 3.1.1: Set-up for deposition of titanium dioxide blocking layer by spray pyrolisis.

The slides are then moved to the edge of the hotplate and left for five minutes to ensure all the solvent has evaporated, and for the glass to cool a little. The slides are then removed and placed on a metal block to cool. Once at room temperature, the

conductivity is checked with a multimeter to ensure the masked part is still conductive but that the blocked area is not.

Magic tape is used to mark out a 1cm wide strip along the long edge of the blocked area, approximately 2 mm from one edge. A small amount of colloid is placed on one side of the tape, and wiped across the strip using a glass rod. This procedure is known as "Doctor Blading".

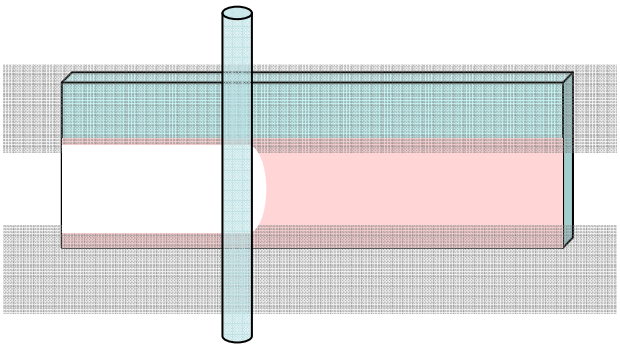

Figure 3.1.2: Doctor blading.

The tape is removed and the slide placed on a hotplate at 100^0C to dry, and then onto a hotplate at 450^0C for 10 minutes to harden. A second layer of colloid can then be applied in the same manner, after which the slides are placed in an oven at 450^0C for 30 minutes. Once cooled, the glass slides are cut to make 2.5 by 1.5 cm electrodes. Excess porous TiO_2 is scraped off using a microscope slide to leave a 1 cm^2 square film, and the electrodes are re-heated to 100^0C to ensure there is no water present. Whilst still warm, the glass is plunged into a 0.5 mM ruthenium dye bath overnight. The dye bath is made from the N 719 dye from Solaronix, the solvent used is acetonitrile and tert-butanol 1:1 in volume. The full chemical name of N 719 is cis-bis(isothiocyanato)bis(2,2'-bipyridyl-4,4'-dicarboxylato)-ruthenium(II) bis-tetrabutylammonium.

3.1.2 Counter electrode preparation.

TEC 8 glass (Pilkinton) which has a conductivity of 8 ohms per square, is cut into 1.5 x 2.5 slides. Two small holes are then drilled with a 0.2 mm carbide burr. These holes are located so that they will be directly above opposite corners of the TiO_2 film on assembly. Once drilled, the glass is cleaned and stored as described for the electrodes. Platinum was deposited by dropping approximately 15 μL of a 5 mM

solution of $H_2PtCl_6 \cdot 6H_2O$ in iso-propanol onto the conducting surface and heating to 400^0C for 20 minutes.

3.1.3 Electrolyte.

The principle constituent of the electrolyte is its redox couple, which is chosen with great care to meet the requirements of the system. The key is that the dye cation should be reduced faster than it can back react with the injected electron, and that the electrolyte should be reduced slowly by the conduction band electrons in the TiO_2, but fast at the counter electrode. So far, no redox couple has competed with iodide/tri-iodide couple in performance. Various solvents can be used, such as acetonitrile, 3-methoxy propionitryl or propylene carbonate.

Additives may also be introduced into the electrolyte to enhance the cell's performance. The addition of tert-butylpyridine, for instance, increases the open circuit voltage, while lithium ions are known to increase the short circuit current. The use of ionic liquids, such as propyl methyl imidazolium iodide (PMII), is also attractive due to their properties such as high conductivity, wide electrochemical window, thermal stability, non-volatility, non-flammability.

Various electrolytes have been used in this study, the exact composition of each one is given in the appropriate section and in appendix D.

3.1.4 Cell construction.

The electrode is removed from the dye bath and placed in acetonitrile in the dark for one hour. Meanwhile the sealant, 25 nm thick hot-melt, is prepared. Two-square centimetre pieces are cut from the sheet, and a 1 cm^2 square is cut out of the centre.

The electrode is removed from the acetonitrile and dried under N_2 swiftly, and with as little exposure to direct light as possible. The hot-melt is placed around the dyed TiO_2 and the counter electrode is placed on top, conducting side facing the electrode, with the holes over the corners of the TiO_2. This sandwich is placed on a hotplate at 120-130 ^{o}C, and pressure is applied for a few seconds using a wooden rod. The cell

is rapidly removed and placed on a metal block to dissipate the heat. The sealing is inspected, and if necessary this process can be repeated. A blunted syringe needle is introduced into one of the holes and a small amount of electrolyte is injected into the cell. The cell is finally sealed by positioning a 1 cm^2 of adhesive above the hole, and then dropping a heated microscope cover slide on top and applying pressure.

3.2 *Cell architectures for specific applications.*

3.2.1 Laser transient experiments.

Small amplitude photovoltage transients exhibit a step rise at the highest background light intensity, see chapter 4. To discover the origin of this, "blank cells" were constructed at the same time as the cells used for the laser transient study. Instead of depositing nc-TiO_2 on the blocking layer described previously, the substrate is simply dyed in the same manner as for a normal cell, and is assembled into a sandwich cell with the same electrolyte and counter electrode. This way, the step rise of pairs of blank and normal cells can be compared, allowing one to distinguish between electrons being injected into the FTO directly from dye adsorbed at the substrate surface, and those injected into the porous TiO_2, and subsequently charging the substrate capacitance. The electrolyte used in this study was 0.03M I_2, 0.6M propyl methyl imidazolium iodide, 0.5M ter-butyl pyridine 0.1M guanidinium thiocyanate in 85:15 acetonitrile:valeronitrile, and the porous TiO_2 layer was made of Solaronix T colloid.

3.2.2 Microwave reflectivity measurements.

As any electromagnetic wave, microwaves are reflected by conductors. For this reason, a normal DSSC could not be placed on the waveguide end, as the microwaves would interact with the FTO substrate before reaching the active part of the cell, i.e. the TiO_2. For this reason, cells were constructed in exactly the same way as reported in section 3.1, except the FTO was first etched away. The etch was achieved by covering the FTO with zinc granules (-30+100 mesh), and dropping on HCl, 36%. These cells are referred to as "etched cells", and were effectively always at open circuit, with a perfect blocking layer, because of the absence of FTO.

Typically pairs of nominally identical etched and normal cells were made, so that the photovoltage could be measured on the normal cells to give an estimate of that of the corresponding etched cell under given illumination conditions.

This set-up was later improved by the fabrication of "window cells". In this case, only a window with the dimensions of the waveguide opening (i.e. 3 by 7 mm) was etched out of the FTO of the electrode before deposition of the blocking layer, and out of the counter electrode after the deposition of platinum. Kapton tape was used to mask the area of FTO not to be etched, and great care was taken when constructing these cells to align the windows of each electrode. The photovoltage and the microwave reflectivity of such cells could thus be measured simultaneously, assuming an ideal blocking layer, at open circuit, the quasi Fermi level would be the same across the contacted and non-contacted areas provided the only recombination pathway is via the porous TiO_2. In order to test the validity of this assumption, the average total electron density was measured by IR spectroscopy at open circuit on pairs of etched, window and normal cells. The different cell architectures gave results which were within the spread expected for nominally identical cells. A better test would be to use a scanning IR spot to measure the trapped electron density in the two distinct regions. This work has been planned in collaboration with the National Physics Laboratories, but at the time of writing has not yet taken place.

Although the window cells are well suited to the simultaneous measurement of the photovoltage and microwave reflectivity, it is not possible to measure the photocurrent of such cells, as the non-contacted area can never be at short circuit, except perhaps a small area around the edge corresponding to the diffusion length. Since the dominant electric field mode in the waveguide was parallel to the short side of the waveguide, reflections of microwaves come from currents being set-up in this direction. For this reason, if discontinuity of FTO could be made in this direction, by etching strips in the direction parallel to the long side of the waveguide, the microwaves could pass un-reflected, and provided the strips could be made smaller than the diffusion length of the cell, microwave reflectivity could be performed at short circuit. Etching was performed in the same way as for the window cells, only strips of bare FTO, of thickness 0.5 mm, were exposed to the etch. The merits of this

cell architecture are discussed at the end of chapter 6. The colloid supplier for these cells was Dyesol (DSC-18T NR).

3.3 *Standard characterisation techniques.*

Cells could be characterised by an array of techniques to gain information on their physical structure, their photovoltaic performance, but most importantly the density, transport and trapping of electrons in the TiO_2 nanostructure. The study of electron transport and lifetime consisted in inducing small perturbations to the photovoltage and photocurrent, in the time and frequency domain, while the exploration of the electron densities, both trapped and free, mostly involved steady state spectroscopies, such as infra-red transmittance, and microwave reflectivity, as well as charge extraction methods. Section 3.4 takes an in-depth look at the various techniques available to determine the total electron concentration, whereas the assessment of the free electron concentration will be the subject of chapter 6.

3.3.1 Physical properties of the solar cells.

3.3.1.1 Film thickness.

The thickness of the TiO_2 films was measured by cross sectional SEM. Electrodes were cut so as to expose the nano crystalline TiO_2 along the edge. The samples are then mounted so that the edge supporting the exposed TiO_2 was upwards. Gold is evaporated onto the surface to improve the SEM resolution. Figure 3.3.1 is one such SEM for a cell from the laser transient experiments which form the basis of chapter 4.

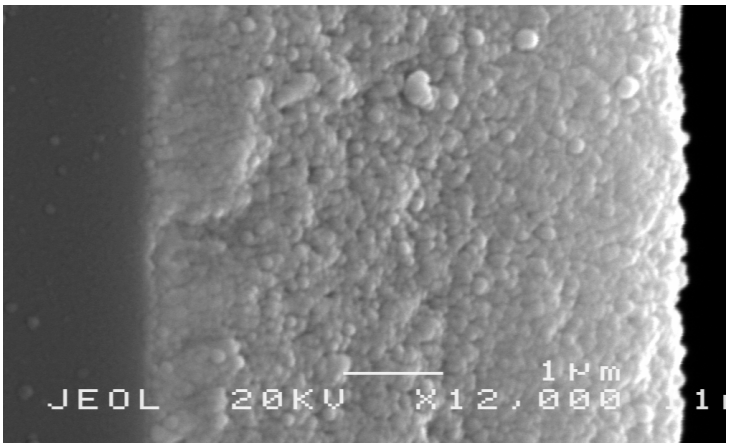

Figure 3.3.1: Cross sectional SEM of a nano crystalline TiO_2 film.

3.3.1.2 Dye coverage.

After immersion in the dye bath, some cells were placed in a 10 mM solution of KOH in order to remove the adsorbed dye. The concentration of the desorbed dye solution was measured using a Varian Carry 50 UV-Visible spectrometer, a typical absorption spectrum can be seen in Figure 3.3.2. The absorption coefficient of the cell, thus obtained, was used in the calculation of ξ as defined in chapters 2 and 4.

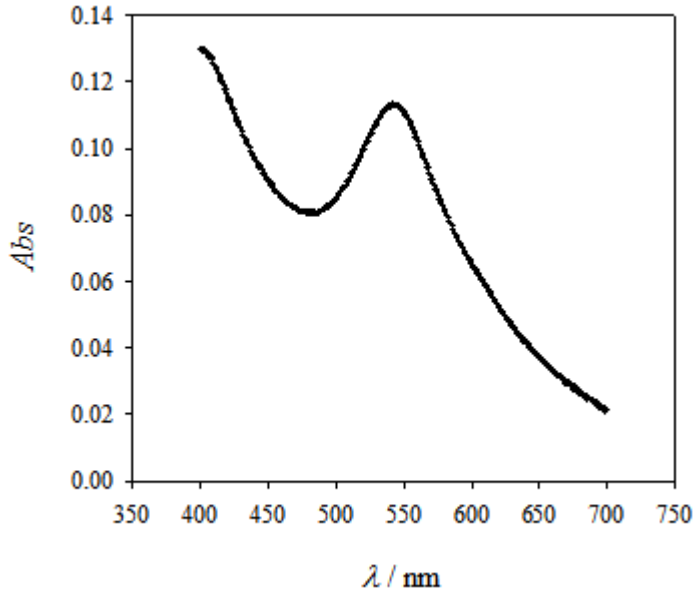

Figure 3.3.2: Absorption spectra of N719 dye desorbed from a sensitised TiO_2 film in 10 mL of 10 mM KOH in water.

3.3.2 Photovoltaic performance.

3.3.2.1 Incident photon to electron conversion efficiency, IPCE.

White light, which is provided by a xenon lamp, is passed through a PC-controlled monochromator to provide the full visible spectrum. The single wavelength light is then directed through a chopper, and is finally incident on the cell. Background illumination is sometimes used to pre-saturate the deeper traps situated in the TiO_2 band gap.

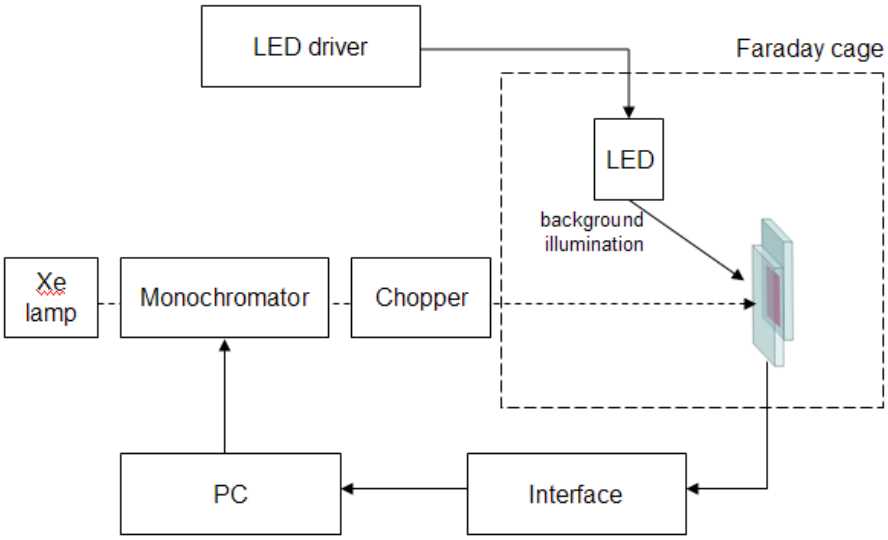

Figure 3.3.3: Experimental set-up for IPCE measurements.

3.3.2.2 Current-voltage characteristics, i-V.

The current voltage characteristics are obtained by illuminating the cell with a solar simulator which consists of a xenon lamp and an air mass 1.5 filter, which is calibrated using a GaAs solar cell. Experiments are carried out at one sun, which has a power density of 100 mW/cm^2. The cell is contacted to a purpose built Whinstonbrook potentiostat, connected to a PC equipped with cyclic voltammetry software. A potential ranging from 0 V to the open circuit potential is applied, and the current is recorded under illumination.

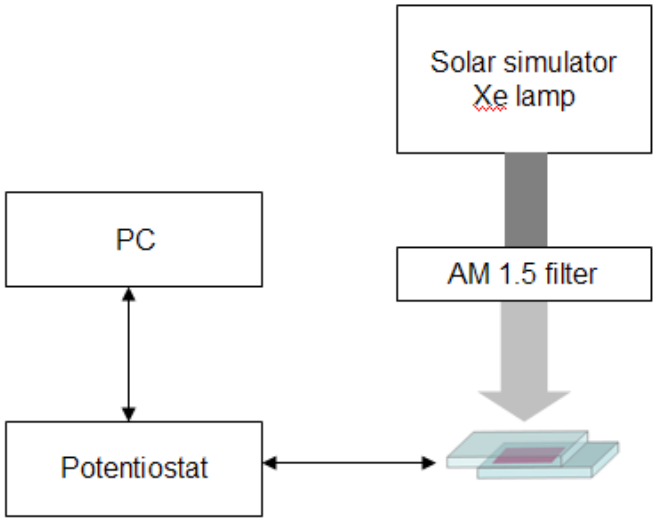

Figure 3.3.4: Experimental set-up for measurement of i-V characteristics.

3.3.3 Dynamic techniques.

3.3.3.1 IMPS/IMVS.

Electron lifetime and diffusion coefficient were determined by IMVS and IMPS, respectively. Cells were illuminated with an LED modulated by 10%. The light intensity was controlled by a series of neutral density filters, and calibrated using a silicon photodiode. The frequency of the light modulation was controlled by a solartron 1250 frequency response analyser (FRA). In IMPS, the cell photocurrent was input to a potentiostat which offset the DC component, and converted the current into a voltage, which was then fed into the FRA for analysis. In the case of IMVS, the DC component of the cell photovoltage was removed by a Stanford Research Instruments SR 560 low noise preamplifier, and the resulting signal was processed by the FRA. Z-view and Z-plot software were used to record and analyse the data.

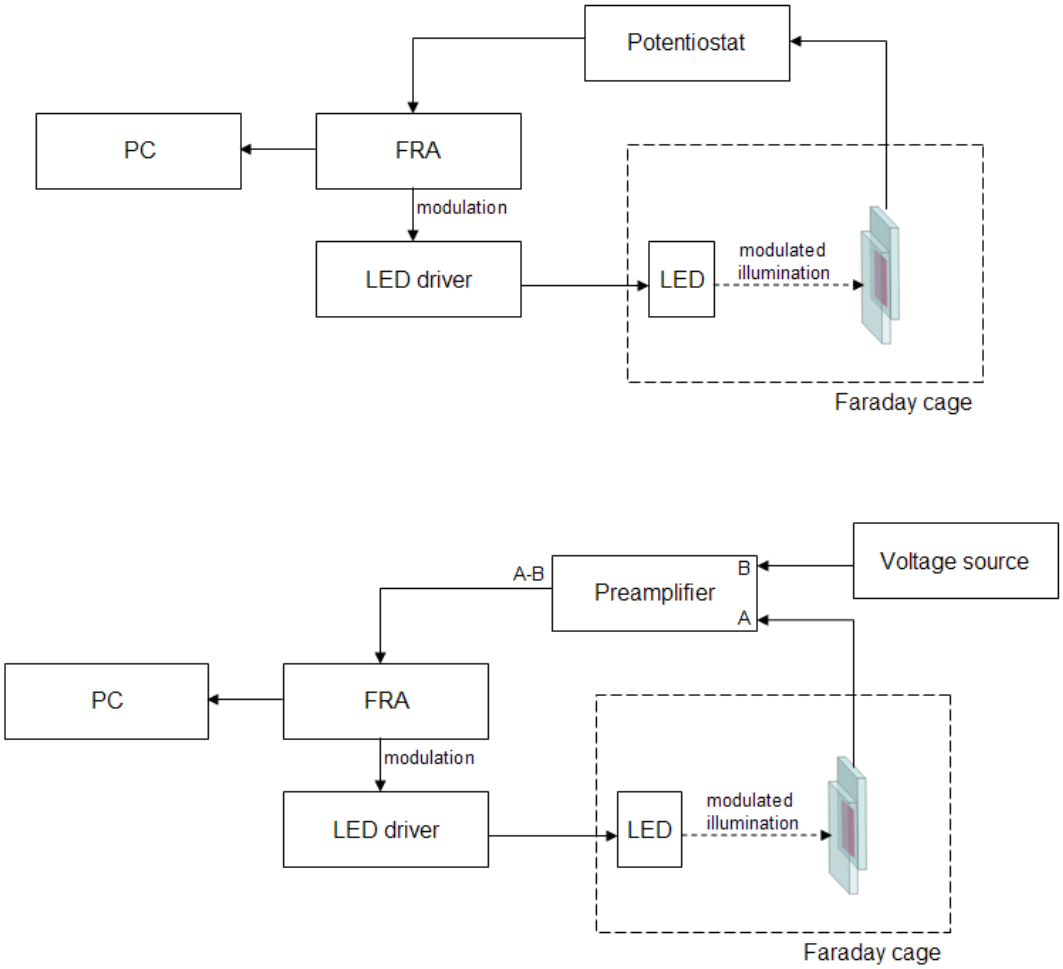

Figure 3.3.5: Experimental set-up for IMPS (top) and IMVS (bottom) measurements.

Typical IMVS and IMPS responses can be seen in Figure 3.3.6, which were taken on cell L12 in chapter 6, at a light intensity of 10^{16} $s^{-1}cm^{-2}$. Bode plots consist of plotting the magnitude or phase versus the modulation frequency, while Nyquist plots consist of the magnitude and phase shift for each frequency being plotted in polar coordinates. Nyquist plots are convenient to analyse, as the maximum imaginary component corresponds to the time constant of interest, the disadvantage being that the frequency is not expressed on such a plot. However, the data can be fitted to equivalent circuit models using the Z-plot software, yielding the maximum frequency, which in the case of IMPS corresponds to the inverse of the transport time, and in the case of IMVS, the inverse of the apparent electron lifetime.

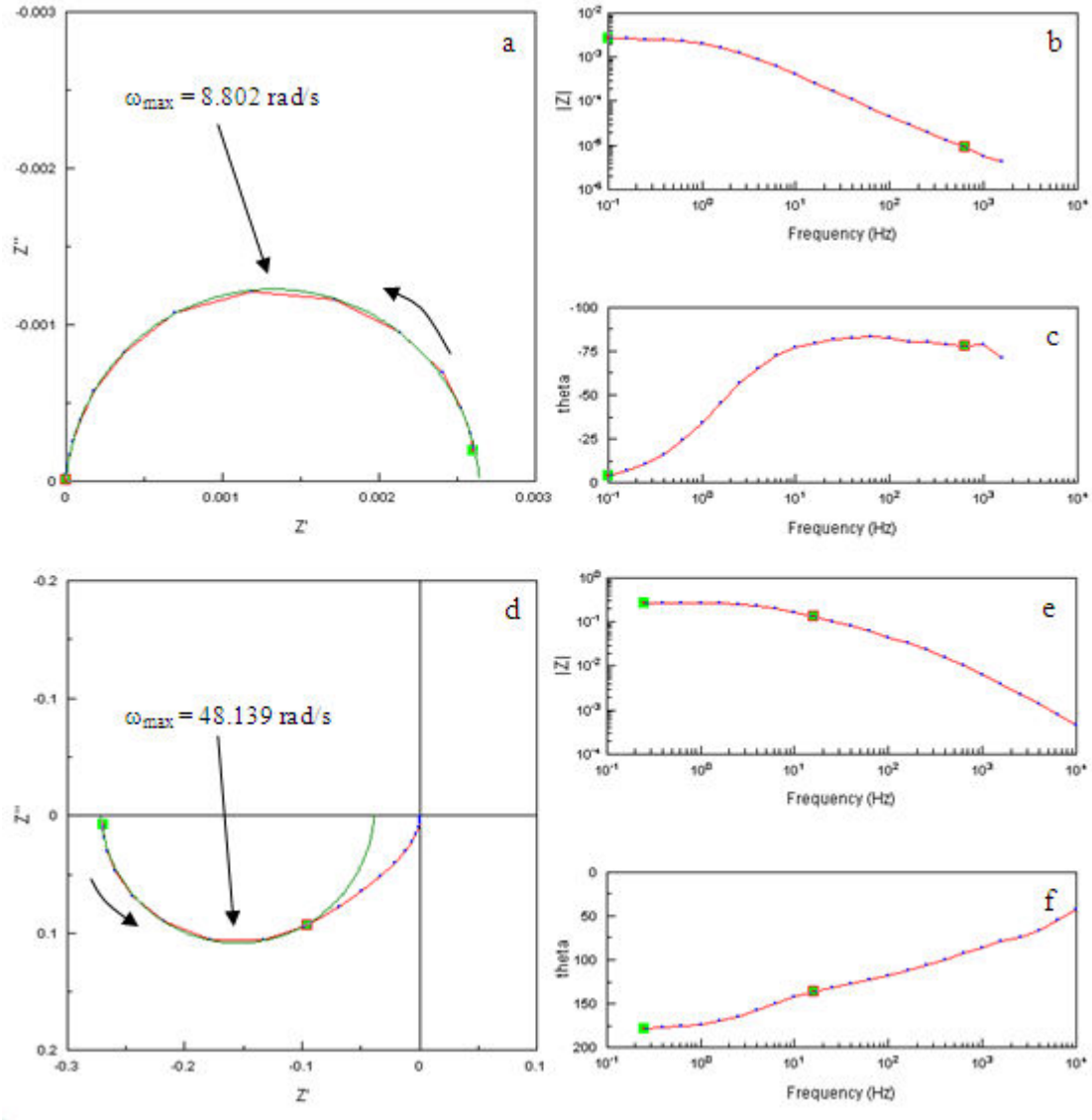

Figure 3.3.6: Example of a set of IMVS (a, b, c) and IMPS (d, e, f) data, which is represented in the complex plane by Nyquist plots (a and d) and with the magnitude (b and e) and the phase difference (c and f) in the frequency domain as bode plots.

3.3.3.2 Photovoltage decay.

The electron lifetime was also determined by open circuit photovoltage decay. The cell is held at open circuit under illumination. The illumination is then stopped, and the open circuit voltage is monitored as it decays using the potentiometry function of the Autolab (PGSTAT 12, Ecochimie). The electron lifetime can be obtained from the gradient of the decay curve.

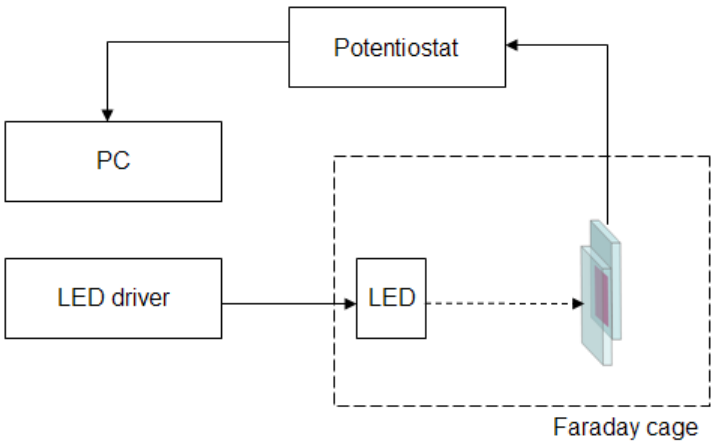

Figure 3.3.7: Experimental set-up for photovoltage or short circuit charge extraction measurements.

3.3.3.3 Electrochemical impedance spectroscopy.

The capacitance of the porous titanium dioxide layer of the cells was determined by electrochemical impedance spectroscopy, or EIS. The counter electrode of the cell was connected to the first reference and the counter electrode of the Solartron 1286 analyser, while the working electrode of the cell was connected to the second reference and the working electrode of the analyser. The cell was illuminated at various light intensities, in order to obtain the capacitance at a range of open circuit potentials. A modulated potential was produced by a Solartron 1250 FRA, which was also used to process the impedance response of the cell.

The capacitance of the blocking layer was determined in two ways, which gave good agreement. Firstly an FTO electrode with a blocking layer was immersed into an 0.1 M aqueous solution of Na_2SO_4 into which sulphuric acid was added to reach a pH of 3. A Solartron 1286 interface was used to carry out electrochemical impedance spectroscopy (EIS) on the electrode in 3 electrode mode, with a carbon counter electrode and a silver-silver chloride reference electrode. The other method was to measure the EIS of a blank cell in the same way as described above for a complete cell, except the DC component of the voltage was generated by the Solartron, rather than being caused by illumination.

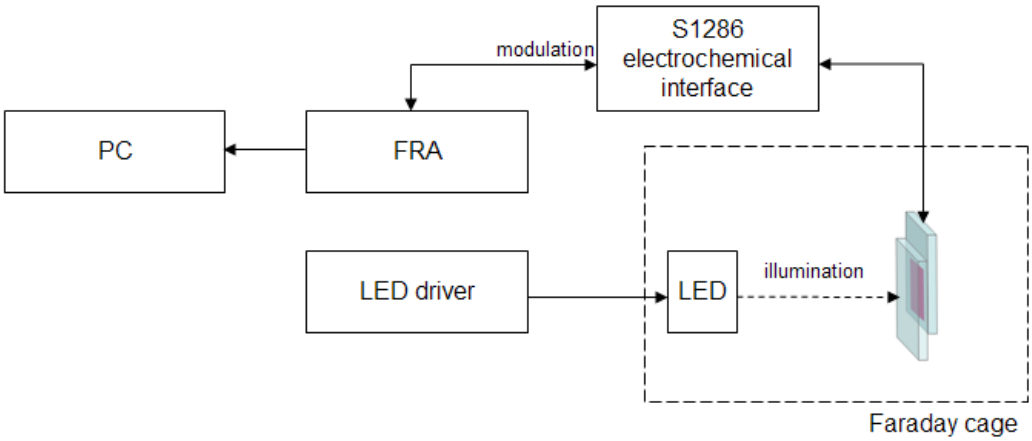

Figure 3.3.8: Experimental set-up for EIS measurements.

3.4 *Probing the trapped electron density.*

3.4.1 Infrared transmittance.

The cell is illuminated, typically with red light, and its photovoltage or photocurrent monitored on an Autolab. The illumination intensity, and therefore the photovoltage and photocurrent of the cell are adjusted by the use of neutral density filters. Meanwhile, an infrared LED (λ=950 nm) is modulated by a digital lock-in amplifier at a frequency of 10 kHz to give a nodulation depth of 100 %. An IR photodiode is placed behind the cell, so that it detects the IR transmission through the cell, a GaAs filter is placed in front of the detector to avoid contributions from the visible light. The lock-in amplifier picks out the transmitted IR signal detected by the photodiode, which is proportional to the total density of electrons within the TiO_2. The output of the lock-in amplifier is recorded by the auxiliary input of the Autolab, which allows the transmitted IR signal to be monitored in parallel with the photovoltage or photocurrent transients as the light is switched on and off.

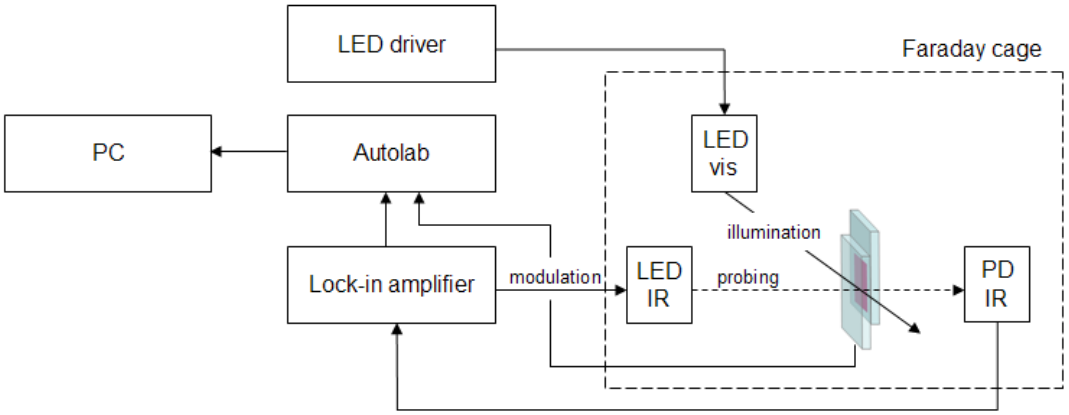

Figure 3.4.1: Experimental set-up for IR transmittance measurements.

3.4.2 "Short circuit" photovoltage.

Boshloo [31] *et al.* proposed an alternative method to estimate the quasi Fermi level position under short circuit conditions. After a period of illumination at short circuit, the cell is switched to open circuit while simultaneously switching off the illumination. The voltage measured at the contact first of all rises as the electron density profile across the film flattens out, before decaying due to back reaction with I_3^-. Provided electron transport is faster than back reaction, the peak voltage is a measure of the average quasi Fermi level at short circuit. The experimental set-up is illustrated in Figure 3.4.2, the switching is achieved by a double pole single throw mechanical switch, and the Potentiostat used is an Autolab.

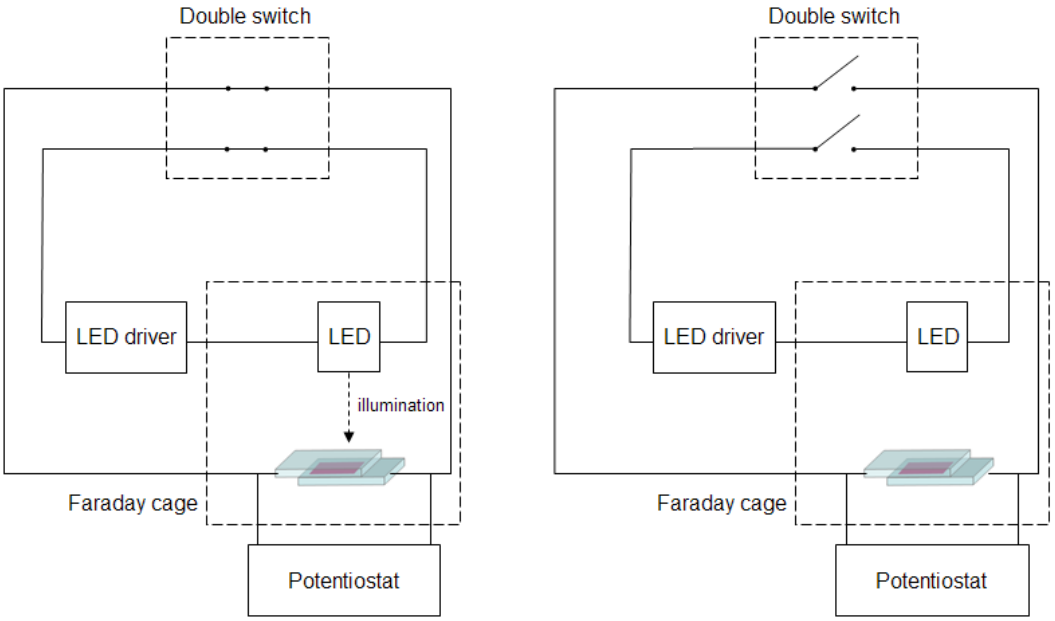

Figure 3.4.2: experimental set-up for measuring V_{SC}. On the left the cell is illuminated at short circuit, and on the right the photovoltage is measured in the dark.

Good synchronisation of the switching is crucial, as it will lead to an over estimation of the short circuit quasi Fermi level if the cell is switched to open circuit before the illumination is turned off, and an under estimation if the light is turned off while the cell is still at short circuit. A study of the lag between the two switches was carried out by James Jennings, and it was found that either switch was just as likely to switch first, and the delay was never more than 2.5 ms, and the mean value was *ca.* 20 μs. This is most likely to be problematic at the higher light intensities, when electron accumulation and back reaction are at their fastest. To account for this, measurements were repeated many times and an average value was taken for the short circuit photovoltage at any given light intensity. Furthermore, the IR transmittance and the short circuit photovoltage were monitored *in situ*.

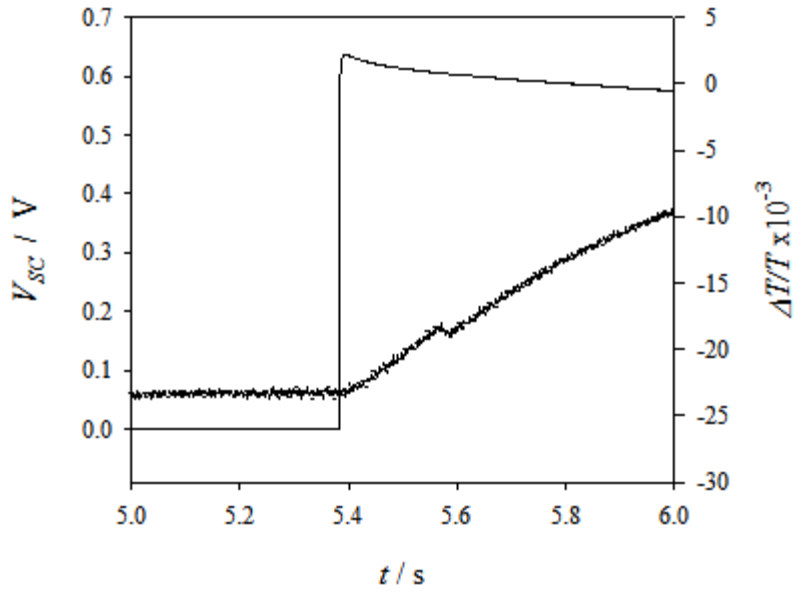

Figure 3.4.3: *in situ* IR and V_{SC} transients, showing that the peak voltage is reached before the electron density decays significantly.

3.4.3 Charge extraction.

In the charge extraction method, the cell is held at open circuit under illumination, the intensity of which is adjusted by the use of neutral density filters. Upon extinction of the illumination, the cell is simultaneously connected to an Autolab in chronocoulometry mode, which integrates the current flowing out of the cell in the dark, corresponding to the total charge stored in the cell at open circuit under illumination. This process is repeated at various light intensities, and therefore open circuit potentials, which leads to plots of stored charge versus open circuit potentials. The experiment, which is illustrated in Figure 3.4.4, consists of maintaining the cell at open circuit under illumination when the two switches are in the A position, then short circuiting the cell in the dark in position B. Since the same double pole single throw switch as in the short circuit voltage experiment is used, so the same issues related to timing need to be considered. If switch 1 switches the light off before switch 2 connects the cell to the potentiostat, the open circuit charge extraction will be underestimated, while it will be overestimated if the cell is connected to the potentiostat while the light is still on.

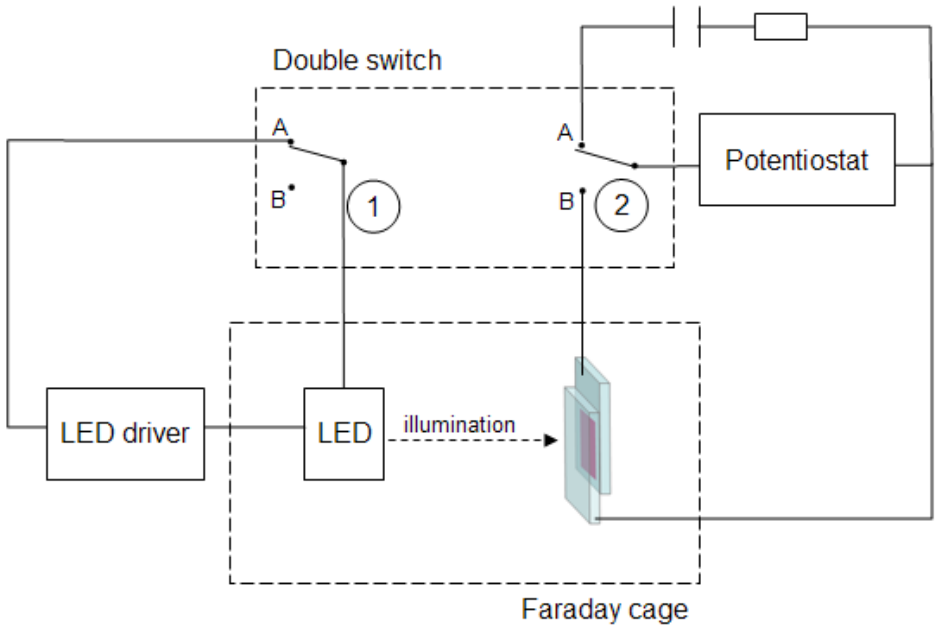

Figure 3.4.4: Experimental set-up for charge extraction switch 1 of the double switch controls the illumination, while switch 2 determines the connections to the cell.

In order to infer the shift between the quasi Fermi level at open circuit and the average value at short circuit, charge extraction was also performed under short circuit conditions. The overall experimental set-up was identical to that of photovoltage decay, illustrated in Figure 3.3.7, the only difference being in the Potentiostat setting, which was chrono-amperometry in this case. The cell is illuminated at short circuit, and the measurement is begun manually just before the light is switched off. The experiment is repeated twice, once with a high time resolution, which allows a more accurate determination of the beginning of the decay, and once at a lower time resolution, which provides more accurate current measurements due to the automatic current ranging. The two data sets are then combined, and the current spike is integrated numerically to calculate the stored charge.

3.4.4 Comparison of the different methods.

For the sake of comparison, the three techniques were applied to the same cell, the results being shown in Figure 3.4.5. There is reasonably good agreement between them, in particular the charge extraction and open circuit voltage methods. However, all three methods predict very small differences between the quasi Fermi level at

open and short circuits. This could be due to several reasons. Firstly, the absolute stored charge of the cells which happened to be used in this study was relatively low, this was due to the films being very thin, *ca.* 4 μm, and the light harvesting efficiency was also poor due to a rather old dye bath being used. This made the measurements, particularly by IR and charge extraction difficult, as the signals being measured were small and noisy. However, this study was aimed only at comparing the techniques so as to choose the most appropriate. Due to it being a steady state measurement which does not rely on switching times, and since it has been shown by Nguyen [32] to be a reliable measure of the total electron density, the infrared method was used in all measurements of total charge reported in the following chapters.

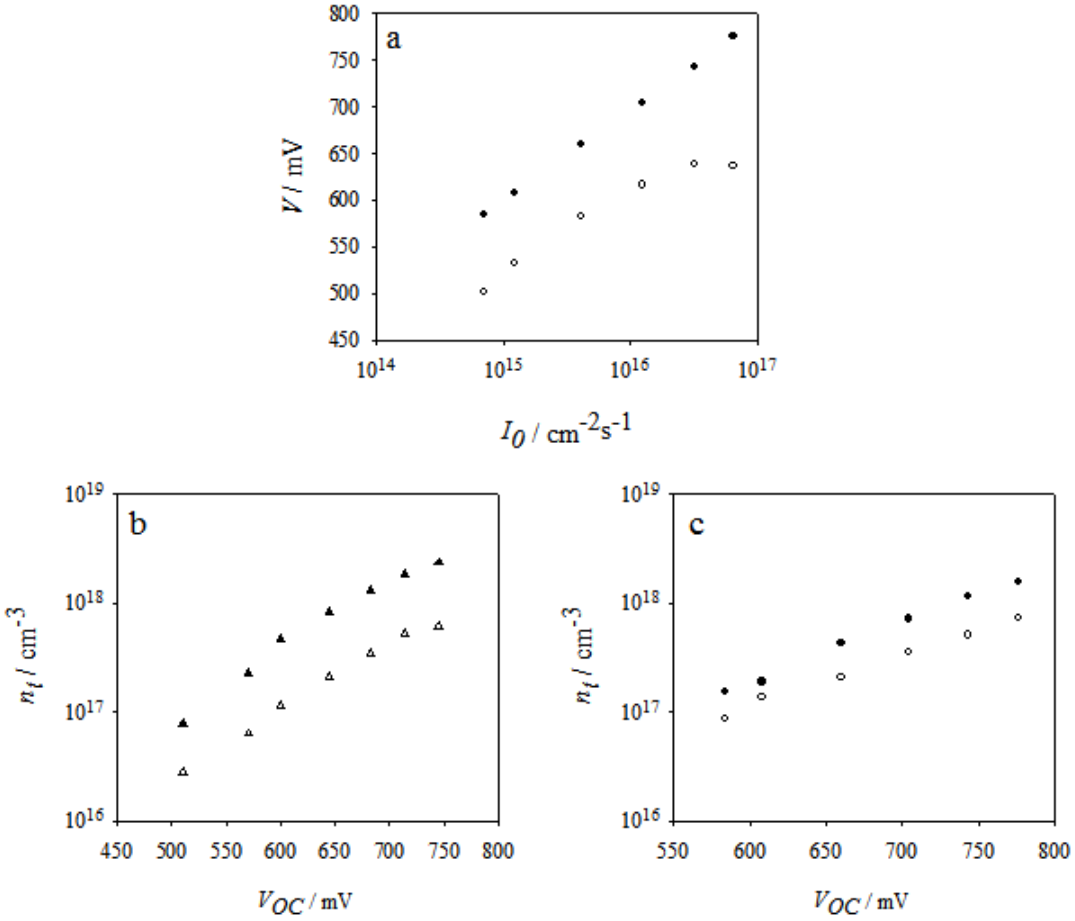

Figure 3.4.5: determination of the relative quasi Fermi level at short circuit by different methods; a) V_{OC} (filled symbols) V_{SC} (empty symbols). b) and c) are charge extraction and infrared spectroscopy, respectively, in each case the filled symbols correspond to the charge at open circuit while the empty symbols correspond to the charge at short citcuit.

4 Laser induced photovoltage rise time.

4.1 *Introduction and theory.*

As seen in the theory section, the diffusion length of electrons in TiO_2 is a key parameter in DSCs as it places an upper limit on the TiO_2 film thickness. The diffusion length can be computed from the apparent electron diffusion coefficient, D_n, and the apparent electron lifetime τ_n, provided they are determined at the same quasi Fermi level of electrons in the TiO_2 and that the back reaction of electrons from the TiO_2 with triiodide is 1st order in electron concentration:

$$L_n = \sqrt{D_n \tau_n}$$

4.1.1

A commonly used method to obtain the apparent electron lifetime and diffusion coefficient are intensity modulated photovoltage and photocurrent spectroscopies, IMVS and IMPS respectively. Since IMPS is carried out at short circuit, whereas IMVS is measured at open circuit, it is necessary to relate short circuit-measured D_n to an effective quasi Fermi level in order to calculate L_n. This can be done by comparing the charge stored under open and short circuit conditions by methods such as charge extraction[21-22], infrared transmittance[32], or the so-called short circuit voltage method[31].

Nevertheless, it is preferable to measure D_n and τ_n directly under the same conditions, for example by impedance spectroscopy[24]. O'Regan *et al.* [13] have proposed an alternative technique which allows the diffusion coefficient to be measured at open circuit. It is based on the time for excess electrons generated in the TiO_2 to charge the substrate capacitance, $\tau_{1/2}$. It can be thought of as the RC time constant of electrical current flowing through the TiO_2 resistance into the substrate capacitance;

$$\tau_{1/2} = R_{trans} \times C_{sub}$$

4.1.2

Similarly, the transport time can be likened to the RC time constant of the charge stored in the TiO_2 capacitance un-charging through the TiO_2 resistance;

$$\tau_{trans} = R_{trans} \times C_{TiO_2}$$

4.1.3

The diffusion coefficient is related to the transport time τ_{trans} by:

$$D_n = \frac{d^2}{\tau_{trans}\xi} .$$

By re-arranging, it is found that the transport time can be calculated directly from the rise time, provided the capacitances of the substrate and the TiO_2 are known.

$$D_n = \frac{C_{sub} d^2}{\xi \tau_{1/2} C_{TiO_2}}$$

IMPS spectra can be obtained by calculating the solution of the continuity equation in response to a sinusoidal perturbation of light intensity for a non-constant electron density, as is the case at short circuit. A simpler model considers the IMPS response assuming a flat quasi Fermi level. The numerical constant ξ, brings the two methods into agreement, and is related to the film thickness and the absorption coefficient of the light used to carry out the experiment. In this case, the absorption coefficient, α, was measured to be 42 000 cm^{-1} at 534 nm, which, given a film thickness of 4 μm leads to a value for ξ of 2.67.

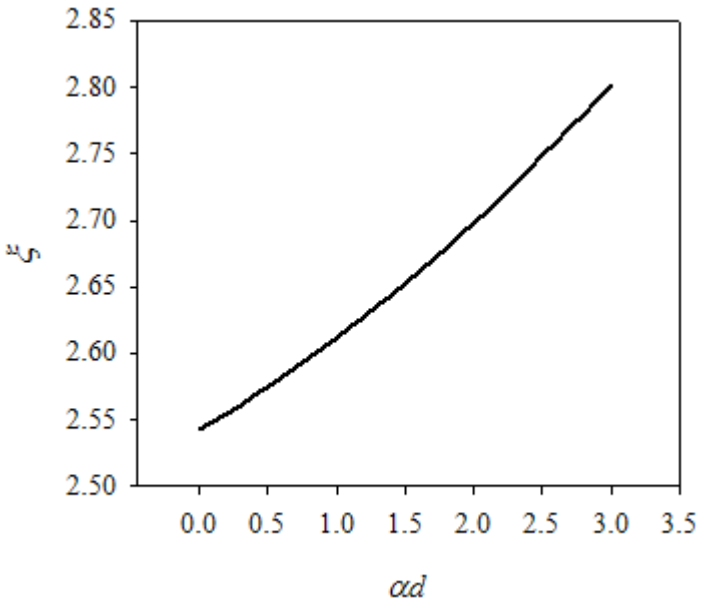

Figure 4.1.1: IMPS factor, ξ, as a function of the product of the absorption coefficient and the thickness of the TiO_2 film for illumination through the substrate. Obtained from the supporting information of reference[33].

4.2 *Photovoltage transients.*

4.2.1 Rise-time measurements.

The cell is held at open circuit and illuminated with a green LED (λ = 530 nm). A small pulse from a Nd:YAG laser (Continuum Minilite, pulse width 3-5 ns, λ = 534 nm) is then superimposed to cause a small rise in photovoltage. The intensity of the pulse is adjusted to give a rise in photovoltage of approximately 10 mV, or in some cases up to 5% of the background value. A glass beam splitter is used to deliver part of the pulsed laser light onto a silicon PIN diode which triggers the digital storage oscilloscope, or DSO (Tektronix model TDS 3012). The transients are averaged by the DSO to improve the signal to noise ratio. A schematic representation of the experimental set up is given in Figure 4.2.1, while typical photovoltage transients can be seen in Figure 4.2.2.

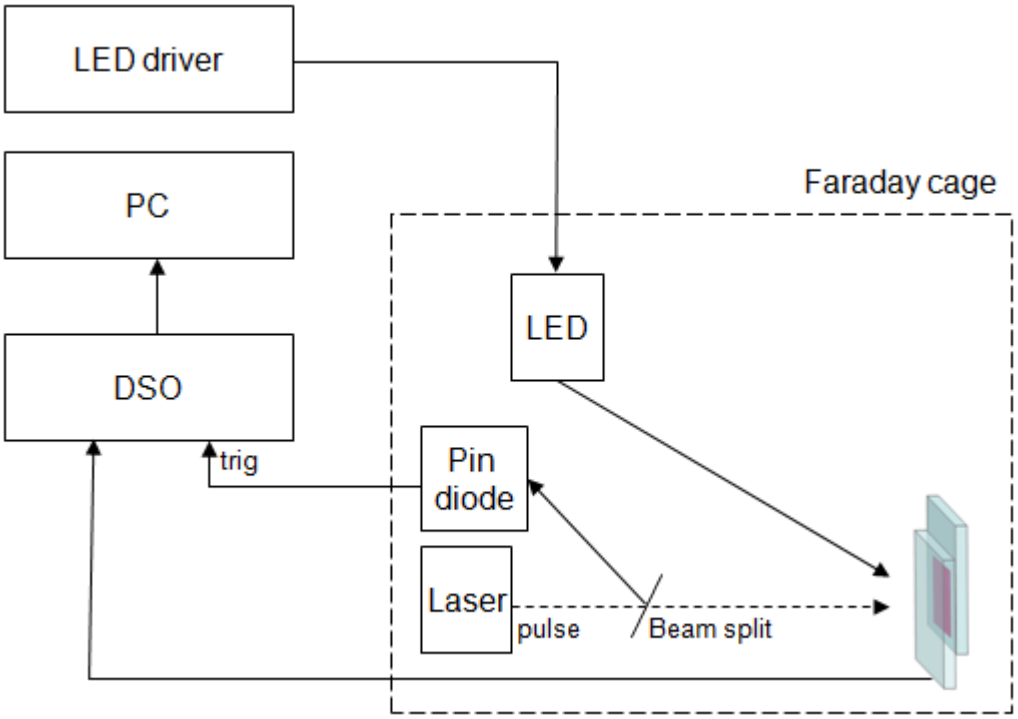

Figure 4.2.1: Set up for laser transient measurement.

Since the photovoltage rise and decay occur on such different timescales, it was possible to analyse them separately. The electron lifetimes were obtained from the transient photovoltage decays by fitting to a single exponential. The rise time was determined by inspection of highly time-resolved transients, and was taken to be the time for the photovoltage to reach a half of the peak amplitude. The reason for this was that it is a convenient manner to gauge the speed of the rise, without requiring a true exponential fit, which was not observed.

At low bias light intensity, the transient rises were smooth and easily analysed. However at high bias light intensity, a step was observed at the onset of the rise. To elucidate the origin of this step, the same experiment was performed on the blank cells. As can be seen from Figure 4.2.2, the photovoltage in the blank cell rises instantaneously, whereas in the full cell the same step rise occurs, followed by a smooth rise. It can therefore be deduced that the step rise in the full cell is due to direct injection by dye adsorbed to the compact TiO_2, whereas the slow rise is due to electrons from the porous TiO_2 charging the substrate. Since the electron trap density increases exponentially with photovoltage, the laser pulse energy must be increased progressively as the DC photovoltage is increased. As a consequence, the

instantaneous charging caused by injection from dye adsorbed on the exposed substrate becomes more pronounced. Since the two charging processes can be clearly distinguished, the step was subtracted before evaluating the voltage rise time from the transport-limited part of the response, see Figure 4.2.4.

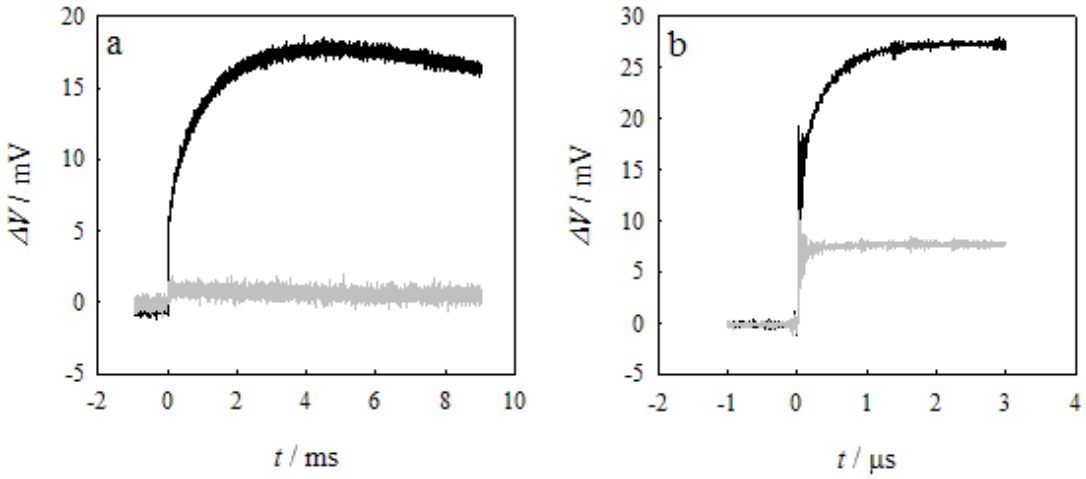

Figure 4.2.2: Typical photovoltage transients used to determine the rise time at two different steady state photovoltages; a) V_{OC} = 400 mV, b) V_{OC} = 700 mV. In each case the black trace is measured on a full cell, while the grey trace is measured on the corresponding blank cell.

The assumption that the step rise is due to direct injection from dye adsorbed to the surface of the substrate can be further justified as follows. The light intensity required to induce a 20 mV rise in the photovoltage from the background value, U_{photo}, in time Δt, can be written;

$$I_0 = \frac{C_{TiO_2} \Delta U_{photo}}{q \cdot IPCE_{TiO_2} \Delta t}$$

4.2.1

Likewise, direct injection into the substrate capacitance, assuming an $IPCE_{sub}$ for the dye adsorbed to the substrate, gives rise to a voltage of;

$$\Delta U_{sub} = \frac{IPCE_{sub} q I_0 \Delta t}{C_{sub}}$$

4.2.2

which leads to an increment of voltage in the substrate being related to that of the TiO_2 film by the ratio of the capacitances and IPCEs;

$$\Delta U_{sub} = \frac{C_{TiO_2}}{C_{sub}} \frac{IPCE_{sub}}{IPCE_{TiO_2}} \Delta U_{photo}$$

4.2.3

The result of this calculation can be seen in Figure 4.2.3, illustrating the fact that as the background photovoltage of the cell increases, direct charging will become more noticeable. Although the IPCE of the blank cell was not measured, the ratio of IPCEs in equation 4.2.3 was adjusted to a value which corresponds to a substrate IPCE of approximately 1%, which seems very reasonable, given that it consists at most of a monolayer of dye on a flat surface.

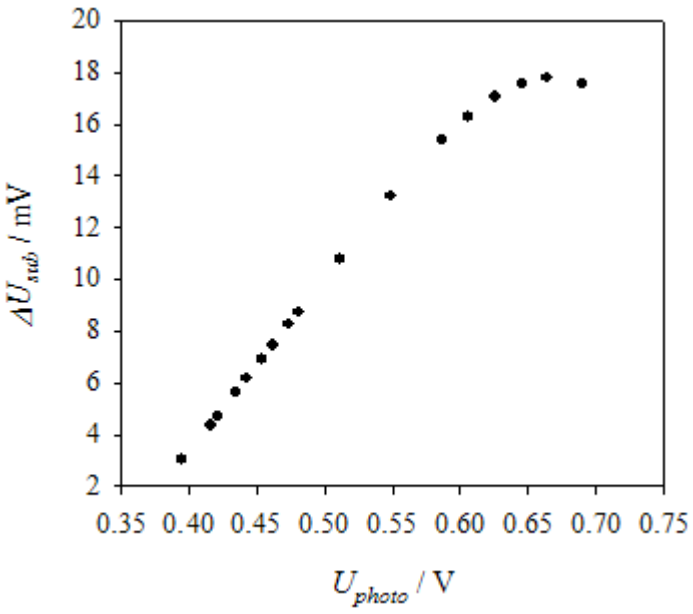

Figure 4.2.3: Expected variation in the voltage generated in the substrate by direct injection from dye adsorbed to the substrate as a function of background cell photovoltage.

The intensity of the laser pulse was adjusted to give a photovoltage rise of approximately 10 mV in the experiments behind the data in Figure 4.3.2, however, when it was understood that the initial step rise was due to direct injection from the substrate, larger pulse intensities were used, which facilitated the determination of $\tau_{1/2}$ and did not alter the measured value. This can be seen in Figure 4.2.4, in which the rise time was measured on the same cell, at the same back ground illumination with two different pulse intensities. Incidentally, this figure also illustrates how the rise time is determined based on highly time resolved transients. It should be noted

that this measurement was performed at a high light intensity, which corresponds to the noisiest measurements, and therefore those with the largest associated error.

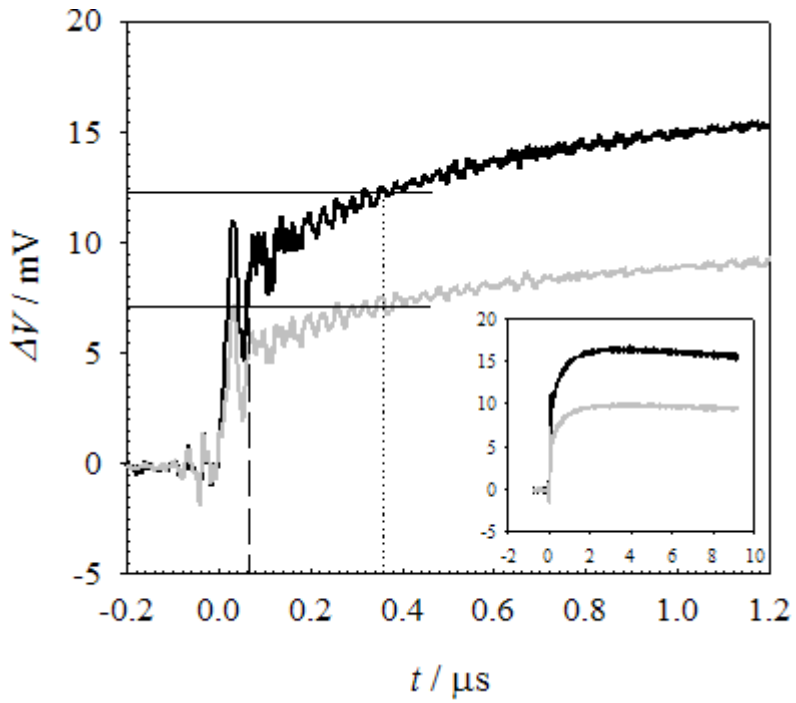

Figure 4.2.4: Highly time resolved photovoltage rise time transient used to determine $\tau_{1/2}$ for a background photovoltage of 690 mV. The two traces were taken with different pulse intensities, the two horizontal lines correspond to half the maximum voltage from the beginning of the slow rise. The dashed vertical line shows the time when the slow rise starts, and the dotted line is the time each transient reaches the half voltage. From the excellent agreement between the two traces, it is concluded that the pulse intensity can be increased to facilitate data analysis. The inset show the same transients on a longer timescale.

4.3 *Results and discussion*

4.3.1 Determination of D_n by the photovoltage transient method.

The capacitance of the porous TiO_2 was obtained by EIS at various light intensities, and thus various open circuit potentials. Figure 4.3.1 shows this, along with the capacitance of the substrate measured on the blank cell over the same range of open circuit potentials.

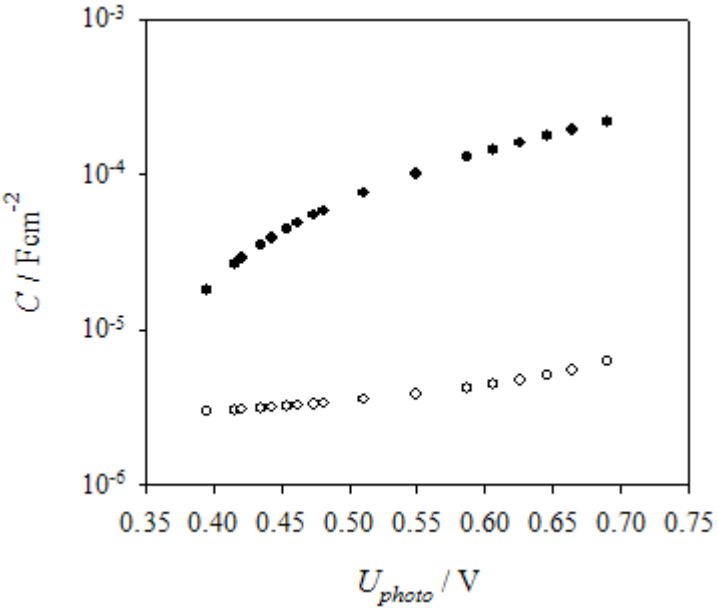

Figure 4.3.1 Nano-porous TiO_2 (filled circles) and substrate (empty circles) capacitances over a range of open circuit potentials.

The photovoltage is expected to rise at a rate which is determined by transport limited charging of the substrate capacitance by conduction band electrons within the TiO_2. The rise time was determined over a range of steady state photovoltages, and was found to decrease, as seen in Figure 4.3.2. This decrease is not only due to the increase in D_n as the quasi Fermi level moves closer to the conduction band, but also to a simultaneous increase in the ratio of the capacitances of the nanoporous TiO_2 and the substrate.

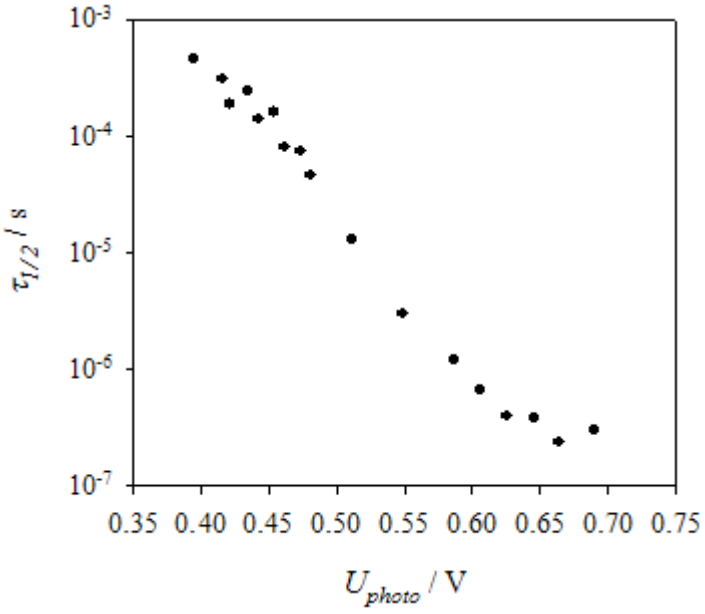

Figure 4.3.2: Photovoltage rise times determined over a range of open circuit potentials.

Using values of the porous and compact TiO_2 capacitances described above, D_n was calculated using equation 4. In this instance the numerical constant ξ was found to be 2.67. The results will be shown in Figure 4.3.5 along with the diffusion coefficient determined by IMPS. The apparent electron lifetime was obtained by fitting the small amplitude photovoltage decay of the same transients as were used to obtain the photovoltage rise time.

4.3.2 Determination of D_n by the IMPS method.

In order to test the reliability of the photovoltage transient method for measuring the electron diffusion length, it was also determined by standard frequency resolved techniques. The effective electron diffusion coefficient and lifetime were obtained from IMPS and IMVS respectively. The figure below shows these results plotted against incident light intensity.

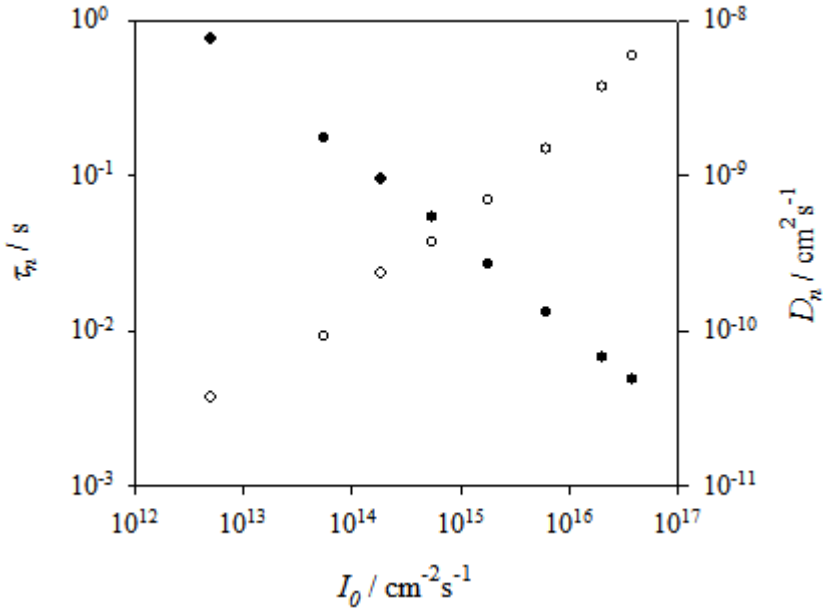

Figure 4.3.3: Electron diffusion coefficient and lifetime at various light intensities.

However, D_n was determined at short circuit, whereas τ_n was measured at open circuit. Therefore, at any given light intensity, D_n and τ_n were determined at different quasi Fermi level positions. In order to find a meaningful value of L_n, it was necessary to find an "equivalent quasi Fermi level" at short circuit. To this end,

the total charge would have been extracted from the cell at open and short circuit, and plotted versus the open circuit potential of the cell at the light intensity at which the extraction was performed. However, due to experimental limitations at the time, charge extraction measurements at open circuit were not possible. Nonetheless, the determination of the shift between open and short circuit quasi Fermi level has been performed several times in our laboratory, by a range of different methods, and typical values of 200 mV tend to be found. For instance, Lobato [34] measured the short circuit quasi Fermi level by a passivated titanium electrode in contact with the TiO_2 film at the interface with the electrolyte, and reported a difference of 300 mV at one sun illumination. For DSCs based on titania nanotubes[33], the difference in quasi Fermi level at open and short circuit was evaluated to be 200 mV by the short circuit voltage method, described in the experimental section. Work published by Wang [17] has found a typical value of 150 mV, while we have measured differences ranging from 75 to 120 mV, measured by IR transmission at open and short circuit. Boschloo [31] *et al.* also assessed the difference in quasi Fermi level by the short circuit voltage method, and found it to be 200 mV.

4.3.3 Comparison of the two methods, and determination of L_n.

Figure 4.3.4 compares the apparent electron lifetime measured by small amplitude decay and IMVS. As expected, there was very good agreement between the lifetime obtained by these two small amplitude dynamic methods. However, due to the relative ease with which IMVS time constants are obtained, these values were used in the calculation of L_n.

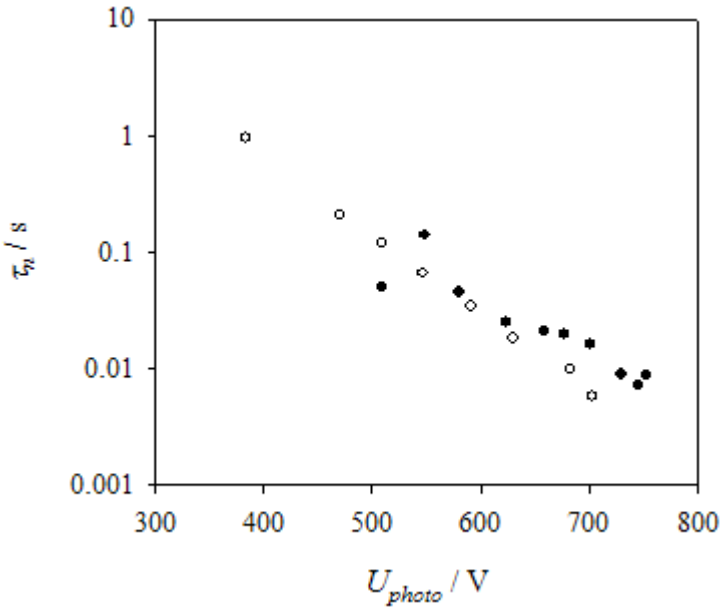

Figure 4.3.4: Comparison of apparent electron lifetime determined by IMVS (empty symbols) and inspection of small amplitude photovoltage decays (filled symbols).

In Figure 4.3.5, D_n obtained from the photovoltage rise time and IMPS are plotted against photovoltage. In the case of IMPS this signifies the open circuit photovoltage of the cell at the light intensity at which the IMPS measurement was carried out. Shifting the IMPS data by 245 mV brings the two data sets into coincidence, which is due to the fact that the short circuit measurement was in fact carried out at a lower equivalent quasi Fermi level. It can be noted that once the shift has been taken into account, the datasets of D_n and τ_n will only overlap over a small quasi Fermi level range, and it is necessary to extrapolate D_n at higher open circuit potentials. This highlights the advantage of measuring D_n at open circuit directly. The D_n derived from photovoltage rise time shows a plateau at highest photovoltages. This is predicted by the quasi static approximation[20], and Bisquert [35] has also shown it to occur if a hopping theory is adopted, whereby trapped electrons are able to hop directly between traps by tunnelling. However, in view of the difficulty in determining $\tau_{1/2}$ accurately at the highest photovoltages, due to the complication of the step rise attributed to direct injection into the substrate, no firm conclusions can be drawn as to whether this saturation is a real effect, or simply an experimental limitation being reached.

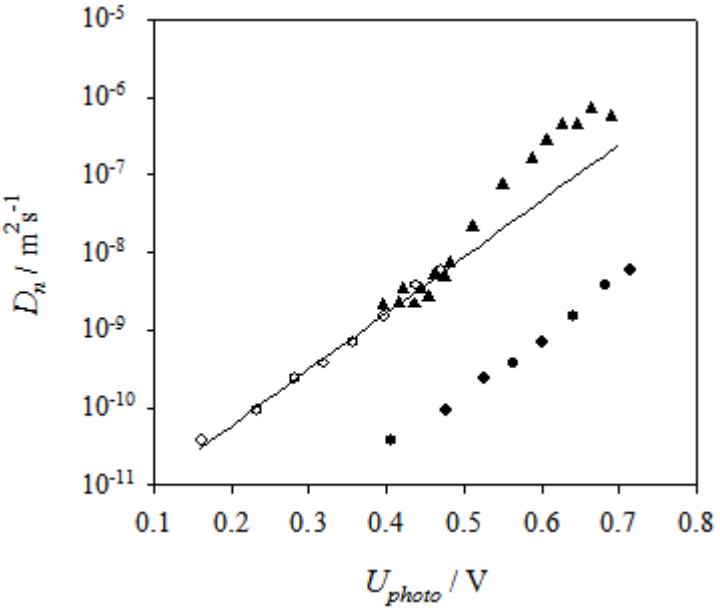

Figure 4.3.5: Electron diffusion coefficient plotted against the open circuit potential of the cell at a given light intensity. Determined by the rise time technique (triangles), by IMPS (filled circles) and IMPS corrected for the quasi Fermi level position (open circles).

The diffusion length was calculated from the electron lifetime measured by IMVS and the diffusion coefficient determined from the rise time, both of which were measured at the same background photovoltage. It can be seen in Figure 4.3.6 that the diffusion length increases slightly with photovoltage from 40 to 70 μm. This is inconsistent with equation 2.7.1, which suggests that the diffusion length is only dependent on the conduction band diffusion coefficient and electron lifetime, however, it is very common to observe diffusion lengths varying with quasi Fermi level, measured by various techniques[24, 29, 33]. The same figure shows the diffusion length calculated from the regression lines in the IMPS/IMVS study, and shifting the IMPS data by 245 mV, as described previously. This estimate indicates the diffusion length is decreasing slightly, although it is in good agreement with the rise time-determined L_n in the region of overlap. In both cases it is found to exceed the film thickness by an order of magnitude, so the electron collection efficiency is expected to be close to 100% in these cells. The main source of error in the rise time-determined diffusion length originates from the visual determination of the time at which the photovoltage reaches half the amplitude. This is due to the transients being noisy, in particular at higher open circuit voltages, corresponding to faster rises.

It should be noted that although values of the difference between the quasi Fermi level at open circuit and the spatially averaged quasi Fermi level at short circuit have been found in the range of 70 to 300 mV, the value of 245 mV is rather high, and since it was not measured directly for this cell, is worthy of some discussion. First of all, it should be pointed out that since the electron profile drops at the contact, the averaged quasi Fermi level will be lower for thinner films, thus giving a larger shift in thinner films, as is the case for this film which was 4 μm thick. This large shift is consistent with the high collection efficiencies expected for thin films. However if it is underestimated, so too will the diffusion length determined by IMPS/IMVS be.

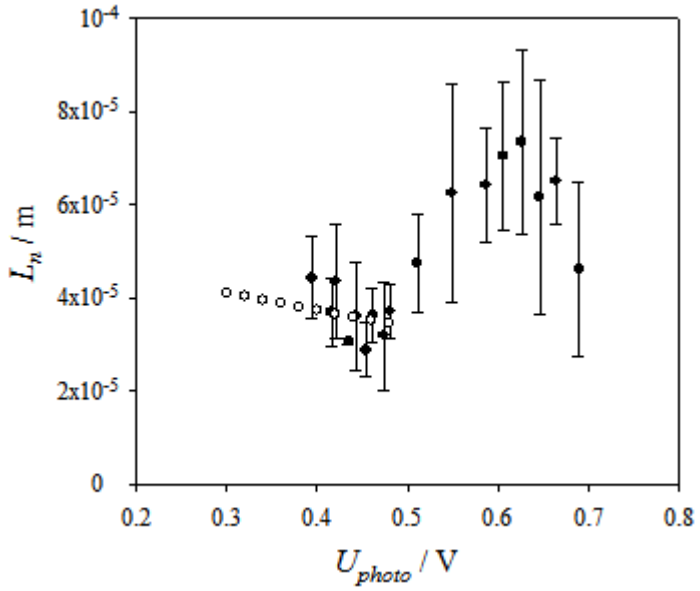

Figure 4.3.6: Diffusion length determined by direct measurement at open circuit (filled symbols), and from the fit of shifted IMPS and IMVS time constants.

4.4 *Conclusions and outlook.*

Small amplitude photovoltage rise times were determined over a wide range of steady state photovoltages, and were used to compute the electron transport time through the nano-porous TiO_2 based on the respective capacitances of the nano-porous TiO_2 and that of the compact TiO_2 blocking layer. Values of the diffusion coefficient calculated with this technique were in good agreement with the diffusion coefficient measured by IMPS once they had been corrected for the difference in quasi Fermi level between open and short circuit. The diffusion length was

calculated from values of the lifetime and diffusion coefficient directly measured under identical conditions, and was found to vary from 40 to 70 μm.

A lively debate currently surrounds the issue of determining the diffusion length in nano-porous TiO_2. There are essentially two approaches; dynamic, which includes frequency and time-resolved small amplitude perturbation techniques, and steady state, which involves comparison of IPCE measurements from front and rear side illumination. The dynamic approach is based upon the assumption that diffusion is governed by single-valued electron lifetime and diffusion coefficient, and the quasi static approximation in order to utilize the experimentally accessible D_n and τ_n, which vary with total electron density and reflect the effects of trapping and de-trapping. This method tends to result in diffusion lengths which far exceed most film thicknesses. Despite this, optimisation of DSSCs rarely considers improvements by extending film thicknesses to the maxima predicted by the diffusion length calculated by dynamic techniques.

Barnes [29] *et al.* have made this observation, and suggest that this is because practically, no improvements are made by increasing the film thickness, which could be due to the diffusion length being over-estimated by the dynamic techniques. An alternative steady state technique to determine the diffusion length, proposed by Sodergren[27] *et al.*, and continued by Halme *et al.* [28] and Barnes *et al.*[18, 29], is to compare the values of the *IPCE* from front and rear side illumination, as described in Chapter 2. It has been found that for cells with deliberately low η_{col}, the diffusion length measured by the dynamic method exceed that measured by the steady state method by a factor of two. On the face of it, the foundations of the steady state technique do rely on very simple measurements, and it has the advantage that no assumptions are made as to the mechanism of electron transport in the nano-porous TiO_2. However the practicalities of performing the computation of L_n requires various accurate optical corrections, which are by no means trivial. Particularly in that there is no way in which it can account for non-uniform dying of the film. Indeed, since dye has to percolate through the rear of the film, from the bulk solution in the dye bath, it is not unreasonable to assume that dye aggregation would occur at the rear of the film, which would act as a filter for rear side illumination. This limitation would also affect dynamic techniques when measured with rear-side

illumination, but it should not interfere with the calculated time constants, as they are found for a given photovoltage or photocurrent, which is an internal measure of the absorbed fraction of the incident light intensity, thus taking the extra loss into account. Evidence for non-uniform dye uptake was found by Jennings *et al.*[33], in that the concentration of dye in the films decreases with film thickness. More importantly, it should be noted that in both studies [28-29] cells had to be purposely made to have large d/L_n, which underlines a fundamental limitation; the technique is only valid in the case where the film thickness exceeds the diffusion length, which is not the case for high efficiency cells. Nonetheless, the dynamic method is not without its critics, Halme [36] has recently shown that D_n is sometimes over-estimated by IMPS, an issue which can be minimised by using light modulation from the rear side, and working with weakly absorbed wavelength, so that the generation profile is as flat as possible throughout the film. However, Jennings and Peter have obtained very good fits taking into account both the non-uniform generation profile and the non-uniform quasi Fermi level across the film. The rise time method, on the other hand, is immune to this particular criticism, since the electron profile at open circuit is uniform.

One example of good agreement between dynamic and steady state estimation of the diffusion length was found in a study by Jennings *et al.*[33], in which for a 20 μm DSC based on titania nanotubes, the short circuit current of a film illuminated from the rear side corresponded to the short circuit current calculated based on the η_{LH} obtained from dye desorption experiments. This was in agreement with the dynamic method, which estimated L_n to be *ca.* 100 μm, based on IMVS and IMPS performed for rear side illumination. So the steady state method can be used on high efficiency cells, perhaps not in a quantitative way, but certainly in a qualitative way, answering the question "is the diffusion length greater than the film thickness?", and as an invaluable means to cross check the dynamic methods, which do need to be used carefully, and should be considered to give an upper-limit, rather than an absolute, irrefutable determination of L_n. Given the limitations of each methodology, the two-fold discrepancy found by Barnes *et al.*[29] seems to show that the two methods are in fact in reasonable agreement. However, much of the preceding discussion relies on the assumption that back reaction is 1st order in electron concentration. If this is not

the case, then all the steady state techniques listed above may be invalid. In order to explain the experimentally observed variation of the diffusion length with electron density, Bisquert [24] *et al.* have recently put forward a model for back reaction which not only occurs via the conduction band, but also via an exponential distribution of surface states. This model therefore predicts a reaction order which is not necessarily unity. Due to the large number of free parameters used in this model, including the distribution of surface states and the reorganisation energy of the redox species in the electrolyte, it is not clear at present what the reaction order is, but it should be kept in mind as a possibility, which would have important consequences in the field of DSC modelling and characterisation.

One novel method in determining L_n could arise as a by-product of the "slit cells" described in chapters 3 and 6. In these cells, strips of FTO were etched away from the substrate beneath the photo-electrode. When illuminated under short circuit conditions, the areas over the etched FTO would be at open circuit (provided the width of the etched area exceeds half the diffusion length), while the areas over the un-etched area would be at short circuit. By performing scanning IR transmittance with a suitably small laser spot, an estimate of the diffusion length could be obtained that would not depend on any assumptions, and by studying the lateral diffusion of electrons, would not be affected by dye aggregation or non-uniform dye uptake throughout the film. This work is planned as a collaboration with NPL, but has yet to be carried out.

5 Development of the microwave reflectivity technique.

5.1 *Introduction.*

As discussed in Chapter 3, electrons injected by the dye into the TiO_2 are divided into two categories; free and trapped. Although the total electron density, which can be approximated to the trapped electron density, is measured by various techniques, the free electron density has not yet been measured. The conductivity in a material where electrons are the majority carriers is defined as;

$$\sigma = nq\mu$$

5.1.1

so that, provided the electron mobility can be assumed to be constant, the free electron density is accessible from the conductivity.

Microwaves are positioned between radio waves and infrared in the electromagnetic spectrum. Their wavelengths range from 1 m to 1 mm, which is equivalent to frequencies between 0.3 GHz and 300 GHz. The frequency of the waves used in this study is about 33 GHz, corresponding to a wavelength in air of about 7 mm. Microwaves are subdivided into bands, according to frequency. For instance, the microwaves in this study belong to the Ka-band, which corresponds to frequencies in the range of 26.5 to 40 GHz. X-band microwaves are also mentioned in this chapter, and correspond to a lower frequency range, 8 to 12 GHz.

When any electromagnetic wave is incident on a conductor, electrons in the conductor are made to move, thus setting up eddy currents. The conductivity of the material dictates what proportion of radiation will be transmitted, reflected, or absorbed. Whereas near infrared radiation – 900 nm i.e. 1.3 eV – is suitable for the study of electrons trapped between the quasi Fermi level and the TiO_2 conduction band – the energetic separation between which is thought to be of the order of 1 eV – microwaves are suited to the study of conduction band electrons because of their low energy, which is of the order of 0.2 meV for the source used here.

The magnitude of the microwave induced current gradually decreases as it progresses into the conductor. The skin depth, δ, is the distance over which the current drops to 1/e of the surface value. For a good conductor, the skin depth is given by;

$$\delta = \sqrt{\frac{2}{\mu\sigma\omega}}$$

5.1.2

As can be seen, the lower the conductivity of the sample, and the lower the frequency of the incident wave, the larger the skin depth. If the skin depth exceeds the sample thickness, the currents on the other surface will induce an electromagnetic wave there, so the incident wave appears to have traversed the material. It will, however, have lost some of its amplitude, and there will be a phase difference between the two waves. With their low frequencies, microwaves are able to penetrate samples with low conductivity. Abayev *et al.*[37] have measured the conductivity of porous TiO_2 across a gap between two electrodes, and have found it to range from 10^{-8} to 10^{-1} S/m over a range of potentials corresponding to operation of a DSC. This corresponds to a skin depth of approximately 20mm to 70m, which is much larger than the TiO_2 thickness, indicating that microwaves are well suited to the study of conductivity in this material. By contrast, the skin depth of FTO, whose conductivity was measured to be $4x10^5$ S/m by four point probe, is of the order of 5 nm, which is significantly smaller than the FTO thickness (about 200nm). This is consistent with measurements of microwave reflectivity on plain FTO, which indicate that 90% of the incident power is reflected.

5.2 *Microwave reflectivity*

5.2.1 Principles.

The reflectance is defined as the fraction of an incident electromagnetic wave which is reflected by a surface. Hence if the properties of the material were to change, for instance as a result of a change in conductivity, the reflectance would also change, according to;

$$\frac{\Delta P}{P_{in}} = \frac{P(\sigma + \Delta\sigma) - P(\sigma)}{P_{in}} = R(\sigma + \Delta\sigma) - R(\sigma)$$

5.2.1

Provided that the reflectivity is a continuous function of conductivity, the linear term of a Taylor expansion performed on the penultimate term in equation 5.2.1 yields;

$$\frac{\Delta P}{P(\sigma)} = S\Delta\sigma$$

5.2.2

Here, an extra step has been taken to replace the incident power by the steady state reflected value, since this is a more accessible experimental parameter. The sensitivity factor *S* is hence given by;

$$S = \frac{dR(\sigma + \Delta\sigma)}{d\sigma}\frac{1}{R(\sigma)}$$

5.2.3

As the conductivity is related to the electron density, microwave reflectivity can be used as a technique to measure the density of free electrons:

$$\frac{\Delta P}{P(\sigma)} = Sq\mu\Delta n_c$$

5.2.4

Two parameters are needed when calculating n_c using equation 5.2.4. The sensitivity factor, *S*, which we have estimated through modelling in this chapter, and experimentally in the following chapter, was taken to be of the order of 0.3 – 0.5 Ωcm. A value for single crystalline anatase of 20 $cm^2V^{-1}s^{-1}$ was used for the mobility[38], although the values reported in the literature span eight orders of magnitude, as summarised in Table 5.1, for clarity. Unsurprisingly, the mobilities reported for single crystalline materials (sc-) generally exceed those for nanoporous (np-) materials. Aside from the possible effect of grain boundaries between particles in reducing interparticle mobility, Hendry *et al.*[39] also suggest that in an inhomogeneous medium made up of TiO_2 and air, the electric field density will be screened by the polar TiO_2, resulting in a weaker field inside the particles, and hence lower mobility. Another trend regards the technique used, with time-of-flight methods consistently yielding much smaller values than other techniques. These differences can be understood in terms of the time scales on which the various techniques probe the electron mobility. Terahertz spectroscopy – which will be discussed in the next section – probes the electron mobility on a timescale between thermalisation of carriers with the lattice, and trapping or recombination. Time of flight measurements, on the other hand, measure an apparent mobility, which is

influenced by the effects of trapping. Microwave and DC conductivity measurements also comprise the effects of trapping, since the mobility is obtained from the conductivity and the total density of photogenerated electrons. Since we are attempting to estimate the free electron density, we choose a value of the mobility which applies to the free electron behaviour – i.e. either prior to trapping, or in a material in which trapping does not occur. The single crystalline value measured by Forro *et al.*[38] is in good agreement with the highly time resolved terahertz measurement by Turner *et al.*[40], although it differs from that of Hendry *et al.*[39], for an almost identical experiment. The difference, it seems, lies with the model used to obtain the conductivity from the terahertz signal. Both studies agree that the Drude model of conductivity, which is based upon scattering of electrons with ions in the lattice with no "memory" of the momentum of the previous collision, is not appropriate in the description of porous TiO_2, although Hendry *et al.* did find it suitable for single crystal rutile. However, the studies differ in the alternative model chosen to fit their data. Turner *et al.*[40], use the Smith-modified Drude model, which accounts for the momentum from previous collisions. Hendry *et al.*,[39] on the other hand, use an effective medium theory, which is an average of air and TiO_2, assuming a porosity of 0.5. It is difficult at this stage to ascertain which of these approaches provides the most reliable result. Despite the lack of a definitive value for the mobility, Turner *et al.* found that the mobility was unchanged over a wide range of electron densities (from 2 – 88 electrons per 25 nm particle on average). This constancy of the mobility signifies that although the absolute value of the electron density from photoconductivity measurements may be scaled by some unknown factor, the way in which it changes with photovoltage and light intensity – which is discussed in detail in the next chapter – should be unaffected by the mobility.

Table 5.1: Summary of literature values of electron mobility in TiO_2.

Author	Mobility /$cm^2V^{-1}s^{-1}$	Technique	Material
Kroeze *et al.*[41]	$3x10^{-2}$	Microwave	np-anatase
Turner *et al.*[40]	15	THz	np-anatase / rutile
Hendry *et al.*[39, 42]	10^{-2} 1	THz	np-anatase / rutile sc-rutile
Forro *et al.*[38]	20	Hall	sc-anatase

Ditterich *et al* [43]	10^{-5}	TOF	np-anatase
Aduda *et al.*[44]	$10^{-7} – 10^{-6}$	TOF	np-anatase
Petrozza *et al.*[45]	$2x10^{-4} – 10^{-3}$	DC conductivity	np-TiO_2

5.2.2 Applications.

A major concern in the emerging semiconductor industry of the early 60's was the measurement of two fundamental properties of a semiconducting sample; the minority carrier lifetime, and the resistivity. These were typically measured by point probe methods – monitoring the decay of the conductivity in the case of the lifetime – although this was difficult in certain materials due to the poor ohmic contact between the semiconductor and the probes. Microwave reflectivity offers a convenient method to measure the bulk conductivity of semiconductors, without the added complication of contacts. As early as 1958, Ramsa *et al.*[46] placed a Ge rod inside K and X-band waveguides, and simultaneously measured the conductivity by point probe and microwave absorption techniques, finding very good agreement. Germanium is well suited to both measurement techniques, due to the quality of the ohmic contact it is able to make with the nickel contacts used in this study, but for materials such as silicon or gallium arsenide, contacting can be problematic, so the microwave method is invaluable in measuring the conductivity of these samples.

It is sometimes impractical to position the sample within a waveguide, and various different experimental configurations have been developed to circumnavigate this issue. Deb and Nag[47] overcame the difficulty of providing light to a single crystal Ge rod by measuring the change in reflected microwave power outside the waveguide. They directed microwaves towards the sample from an open ended waveguide, and used a horn connected to a detector to capture the reflected waves. The open nature of this method makes it particularly suited to studying large, or awkwardly shaped samples, and those requiring irradiation by light. However, by its open nature, the technique is very sensitive to stray reflections.

The next step was taken in the early seventies, by researchers at the University of California, including Tributsch[48], who enclosed ZnO single crystals in a microwave resonance cavity, which not only provided a more spacious location for the samples

while being isolated from outside interference, but also allowed the sample positioning to be adjusted to the maximum electric field position. They turned their attention to the study of charge carriers and dipoles in the space charge layer and the Helmholtz layer of a semiconductor electrolyte interface, and compared the method to standard electrochemical procedures.

The mid eighties saw the combined efforts of Kunst, Beck and Tributsch, who made great advances not only experimentally, but also in their application of optical modelling, in order to predict the change in reflectivity as a function of sample conductivity, and so to estimate the sensitivity factor. They demonstrated the applicability of microwave reflectivity to the study of semiconductor|electrolyte interfaces[49], by introducing a small electrochemical cell into a short circuited waveguide. Separately Kunst and Beck applied the Fresnel equations for reflection of electromagnetic waves across a series of interfaces to predict the conductivity dependence of the reflected microwave signal, which then allowed a detailed and quantitative comparison between theory and experiments based on single crystalline silicon.[50-51] Tributsch later studied solid state devices, such as p-n junctions, and metal oxide semiconductor junctions with Wünsch.[52]

Peter and Schichthörl[53-54], whose interest was also in investigating semiconductor-electrolyte interfaces, were able to draw quantitative conclusions from microwave reflectivity, as they were able to find the sensitivity factor, *S*, in equation 5.2.2 by comparing the capacitance inferred from the conductivity measurements, and that measured electrochemically by impedance spectroscopy. These studies allowed them to measure the flat band potential of n-Si samples in various electrolytes, as well as separate the effects of charging the space charge layer and surface states, as the microwave method is not sensitive to the latter, owing to their low mobility. Experimentally, their approach was bolder than in previous studies, since they simply placed the Si wafer on the un-terminated waveguide end, and constructed a three electrode cell on the other side. Semiconductors were contacted in such a way that potential steps could be applied to them, and impedance spectroscopy could be performed *in situ*. Schichthörl and Lewerentz[55] then went on to make simultaneous measurements of microwave reflectivity and photocurrent density, and used these values to perform mathematical modelling of various parameters within the

semiconductor electrolyte junction, such as the charge transfer velocity, and the surface recombination velocity at the n-Si|NH_4F junction.

Peter and co-workers[56-57] also continued to study semiconductor electrolyte junctions by a combined approach of microwave reflectivity and more common electrochemical methods. Not only did they obtain the sensitivity factor experimentally as with Schlichthörl, but they also calculated a theoretical value, similarly to Kunst[50], by solving the continuity equations to find the electron and hole distribution in the semiconductor, and combining the results with the Fresnel reflection coefficients for the various phases in the microwave path; air, bulk semiconductor, space charge layer, electrolyte. While studying the evolution of hydrogen at the surface of p-Si in ammonium fluoride solution, they found there to be a disagreement between the sensitivity factor determined in each way of a factor of two.[58-59] They attributed this discrepancy to simplifications in the Fresnel calculations. Nonetheless, they went on to use microwave reflectivity to measure the electron transfer rate by a steady state measurement, which involved measuring the conductivity of the space charge layer, which was a direct measurement of "queuing" electrons, so that a higher conductivity corresponds to a lower transfer rate. They were also able to perform frequency resolved measurements very similar to IMPS, from which they could extract both the transfer rate and the recombination rate.

For the past thirty five years, Warman and co-workers[60-63] have been using the time resolved microwave reflectivity technique to study the conductivity of a plethora of different materials, many of which have photovoltaic applications. Their work distinguishes itself from that of others in that the main focus is on "soft" materials such as polymers, or nanocrystalline materials such as TiO_2. Their experimental setup consists of an X-band waveguide terminated with a metal grid. This allows light to enter the waveguide while maintaining a closed ending to the microwaves. The sample (for example nc-TiO_2 on a quartz substrate) is placed inside the evacuated waveguide, at a position of maximum electric field, i.e. an odd number of quarter wavelengths from the end of the waveguide.

In an attempt to probe the injection efficiency and kinetics, and the identity of the electron traps which are known to exist beneath the TiO_2 conduction band, the time

resolved microwave conductivity method was applied to samples of bare and sensitised TiO_2 in the absence of electrolyte.[41] First of all, a comparison was made between the wavelength dependence of the microwave reflectivity and absorption spectrum of the sensitizer. The microwave signal was found to trace the action spectrum, indicating that the sample was indeed increasing in conductivity in the expected manner, although the relative height of the peaks suggested a higher injection efficiency towards shorter wavelengths. The decay transients yielded a power law decrease of the characteristic decay time with light intensity, which is indicative of an exponential trap distribution. The authors also observed that upon excitation with ultraviolet light, which is absorbed purely by the TiO_2 itself, both samples with and without sensitizer displayed the same recombination transient, which they took as evidence that traps were not located at the surface, conjecturing that the presence of the antenna layer would be likely to modify them in that case. At steady state, the product of the mobility and the injection efficiency, $\eta_{inj}\sum\mu$, is expected to be constant over a range of light intensities, in particular under UV illumination, where the efficiency of formation of electron hole pairs should be close to unity. This was not found to be the case, with the product increasing, and then decreasing. However, with bias illumination, the product $\eta_{inj}\sum\mu$ was found to be almost constant over the lower light intensity range, only dropping off at a high light intensity. The increase at lower light intensities was thus attributed to trapping effects. They suggested two possible explanations for $\eta_{inj}\sum\mu$ falling off at higher light intensities, either that the injection efficiency was lowered due to rapid recombination, or that the electron mobility falls off at this point, owing to the effect of electron-electron repulsion. On closer inspection, they found that for all excitation wavelengths, the point at which the product stopped being constant corresponded to an average of one electron per particle – corresponding to 10^{18} cm^{-3} for 9nm particles – pointing towards electron-electron repulsion. This conclusion was strengthened by the fact that the dye-coated sample exhibited the same behaviour, implying that there was no change in recombination between the two cases, which could have been expected for the sensitised cell. This possibility of a changing electron mobility is very significant, since it seems to contradict the assumption that transport is only possible via the conduction band. However, as discussed in section 5.2.1, Turner *et al.* [40]state that for a range of 2 to 88 electrons per particle – which for a particle diameter of 25 nm, corresponds to approximately 10^{17} to $5x10^{18}$ electrons per cubic

centimetre – the mobility is unchanged. This disagreement could come from the difference in particle size, if, as suggested by Kroeze[41] *et al.*, the reduction in mobility is due to electron-electron repulsion. In which case, given that our TiO_2 particles have a diameter of 20 nm, our mobility is expected to be closer to that of Turner *et al.*. Also, due to the absence of electrolyte, which screens any electric fields at the surface of the particles, there could be electron-electron interactions which would not occur in a working cell. Furthermore, in the microwave study, a constant sensitivity factor was assumed, which we have not found to be the case in our experiments. This point will be discussed in more detail in chapter 6.

Terahertz spectroscopy is an alternative non-contact method for measuring the conductivity of a sample. The technique, which was first applied to TiO_2 by Schmuttenmaer and co-workers[40, 64] is similar to microwave reflectivity, in that the absorbance of the sample is related to its conductivity. It differs in that it is a pump-probe technique, in which a fs laser pulse is used to excite the sample, followed by a terahertz pulse after a certain delay time. By monitoring the transmitted terahertz signal as a function of delay time, the conductivity can be measured over different timescales; allowing the different physical processes contributing to the change in conductivity to be isolated. This method can also be used to determine the complex permittivity of the material under study, since both the magnitude and the phase of the transmitted signal are detected.

5.3 *Modelling.*

5.3.1 Theory.

In order to quantitatively relate $\Delta P_r / P_r$ to changes in $\Delta\sigma$ according to equation 5.2.2, the sensitivity factor, *S*, is required. As described in section 5.2.2, the reflection can be predicted based on the Fresnel equations. These deal with reflection and refraction of electromagnetic waves at an interface. Instead of considering only the angles involved, such as in Snell's law, the amplitude is also taken into account. At normal incidence, the reflectance and transmittance of an electromagnetic wave through an interface is given by;

$$R = \left(\frac{n_t - n_i}{n_t + n_i} \right)^2$$

$$T = \frac{4 n_t n_i}{\left(n_t + n_i \right)^2}$$

5.3.1

This set of equations is a simplified form of the Fresnel equations for normal incidence, a full derivation of which can be found in Hecht[65]. The complex refractive index is related to the permittivity and the conductivity according to[66];

$$n^2 = \mu_r \left(\varepsilon_r - \frac{i\sigma}{\omega \varepsilon_0} \right) = \mu_r \varepsilon_r(\omega)$$

5.3.2

where the complex permittivity is given by;

$$\varepsilon = \varepsilon' - i\varepsilon'' = \varepsilon_r(\omega) - i\frac{\sigma}{\omega \varepsilon_0}.$$

5.3.3

The samples in the present study can be likened to a stack of materials with different refractive indices.

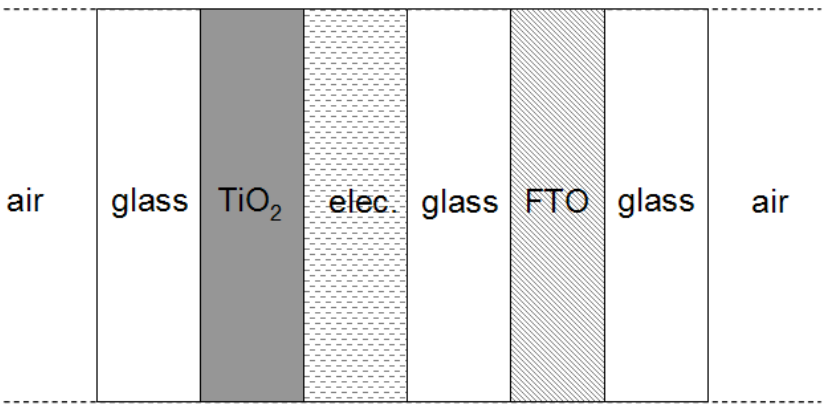

Figure 5.3.1: Stack-model of the DSC used to calculate the expected reflected power using the Fresnel equations.

By varying the conductivity of the active layer, i.e. the TiO_2, and calculating the expected microwave reflectance, the proportionality between the reflected power and the conductivity can be found, which is the sensitivity factor, *S*. The derivation of equation 5.2.4 by Taylor expansion relies on the change in conductivity, $\Delta\sigma$, to be

small. Since the experiments, presented in chapter 6, are "light on, light off" experiments, this assumption also needs to be verified.

5.3.2 Literature survey of the complex dielectric constant for the materials of interest.

A study of the dispersive properties of TiO_2 at 2.45 GHz found the real part of the dielectric constant, ε', to be 77 for Degussa P25 nanoparticles[67]. they also report a complex permittivity of 10, although this value was not necessary in the context of our work, since the conductivity is the variable used to predict the change in reflectance. The range of values used will be discussed in section 5.3.4, and later in Chapter 6.

The electrolyte used in our cells was based on 3-methoxypropionitrile. The closest dispersion study found in the literature was on acetonitrile over a range of frequencies including 33 GHz. The real and imaginary parts were found to be, respectively, 25 and 15.

Due to its various applications as an optically transparent conductor, the dispersive properties of FTO are well studied in the visible and near infrared part of the spectrum[68-69], but no data was found for wavelengths above 2500 nm. The only data found for the real and imaginary components of the complex permitivity are therefore 4 and 2, respectively, at 2500 nm[70].

Air was considered as a vacuum, while the glass was taken to have a dielectric constant of 4, and a conductivity of 10^{-4} S/cm[71-72].

5.3.3 Experiments performed to refine parameters.

In order to facilitate the modelling, simpler stacks were constructed with constituent parts of the cell, as detailed in Table 5.2. The idea being to first of all test the model was working correctly, and secondly to adjust some of the parameters for the various refractive indices. Each measurement was averaged 20 times, and the standard deviation was calculated. This was particularly important for the window cells, as

small changes in alignment of the FTO window and the waveguide aperture meant the absolute reflectance was not perfectly reproducible. In combinations 5-7, the effect of the different constituents of the electrolyte were studied. In this case no averaging was performed, however, the removal and insertion of the electrolyte were performed *in situ*, without disturbing the cell alignment, and for this reason the data are considered reliable for the investigation of the reflectance of the solvent and electrolyte molecules. Combination 9 was in fact measured with the four different electrolytes used in this study. However, since the difference in average reflectance between the different electrolytes was less than the standard deviation of any electrolyte, it was concluded that the electrolyte composition had no sizable impact on the reflectivity, and an average value was taken.

Table 5.2: Measured reflectance for simple stacks of constituents of a DSC.

combination	stacks	Reflectance, %
1	Air/FTO/glass/air	91.6 ± 0.3
2	Air/glass/FTO/air	59.3 ± 0.3
3	Air/glass/air	60 ± 2.3
4	Air/glass/air - window	51.7 ± 2.3
5	Empty cell - window Air/glass/BL/air/glass/air	31.2
6	Introduce solvent - window Air/glass/BL/3-MPN/glass/air	32.3
7	Replace solvent with electrolyte - window Air/glass/BL/elec./glass/air	33.7
8	Empty cell - window Air/glass/BL/air/glass/air	35.4 ± 1.3
9	Seal with FTO - window Air/glass/BL/elec./glass/FTO/glass/air	48.5 ± 1.8
10	Full cell - window Air/glass/BL/nc-TiO_2/elec./glass/FTO/glass/air	42.9 ± 3

5.3.4 One dimensional model.

Kunst and Beck [50-51] have modelled the sensitivity factor, S, for microwave reflectivity in silicon, over a large range of conductivities, and have found it to change for conductivities larger than approximately 10 S/m. One must first consider the range of conductivities expected in a DSC as a function of photovoltage. This can be calculated based on the voltage dependence of the free electron density, as discussed in the theory chapter;

$$\sigma = n_C \mu q$$

5.3.4

The result of this calculation can be seen in Figure 5.3.2 (b) for conduction band positions above the redox Fermi level ranging from 0.9 to 1.2 eV. The relative conduction band position was taken to be 0.9 eV for cell E23 (electrolyte H1), and for the other cells, it was inferred from the trapped electron densities as a function of photovoltage, see Figure 5.3.2 (a). From this data it can be seen that the conductivities of the solar cells studied in the microwave reflectivity measurements should not lie outside the range 10^{-6} to 10 S/m.

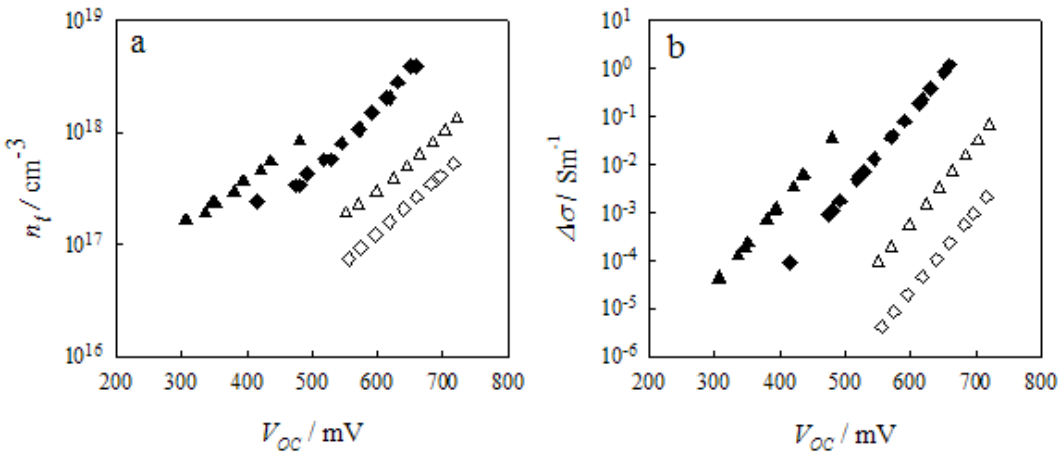

Figure 5.3.2: a) Trapped electron density, n_t measured as a function of photovoltage for cells made with electrolyte H1(filled triangles), H2 (empty triangles), H3 (filled diamonds) and H4 (empty diamonds). b) Calculated conductivity as a function of photovoltage for different energy differences between the redox potential of the electrolyte, and the conduction band of the oxide.

If the system were to behave exactly the same as in the study by Kunst and Beck, the photo-conductivities in this study would be expected to lie within the range where the sensitivity factor is constant. However, since the above mentioned study was

based on silicon, it is possible that the TiO_2 system would behave differently. Another major difference between the system under study here and that of Kunst and Beck is that their sample was enclosed in a waveguide, whereas in our case, the sample was placed on the waveguide end, with a highly conducting FTO plate positioned 1 mm behind the FTO layer. Figure 5.3.3 illustrates the possible interaction of the electromagnetic field and the waveguide end terminated in different arrangements, with the dashed lines representing the wave fronts. In (a), a conducting plate is in contact with the waveguide end. As a result, the waveguide is fully terminated, and all power is reflected back into the waveguide. In (c), the waveguide is open, and power will be radiated out, while some is reflected due to the change in impedance between the waveguide and the air. The arrangement used in the experiments reported in the next chapter is illustrated in b), whereby the sample is placed between the waveguide end and a conducting FTO sheet. This has the effect of channelling part of the power between the plate and the waveguide, acting as an antenna.

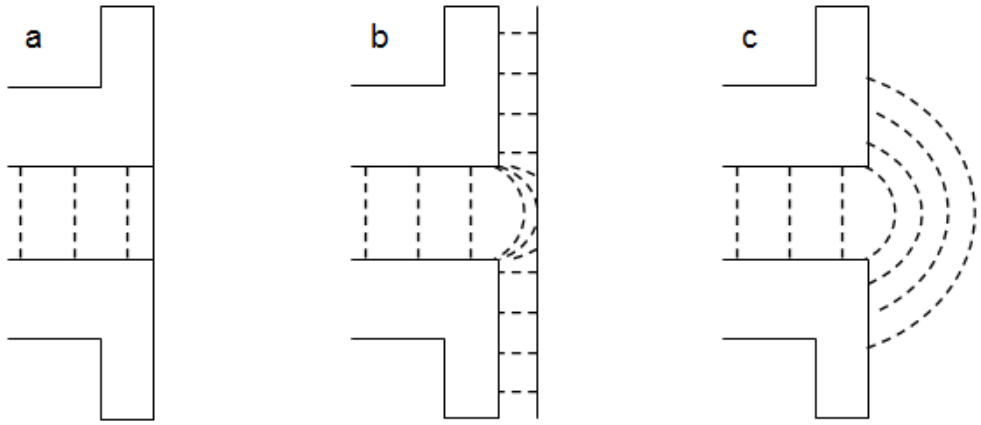

Figure 5.3.3: Electromagnetic wave fronts at the waveguide end with a) a metallic termination, b) a metallic termination a short distance from the waveguide end, and c) an open ended waveguide.

This "leakage" of electromagnetic field makes quantitative modelling of the stacks impossible, unless a 3-dimensional model, taking into account leakage perpendicular to the waveguide propagation can be constructed. This work is underway by Eric Maluta, Dr Stephen Bingham and Prof. Alison Walker (Department of Physics, University of Bath) using Comsol software. A preliminary result can be seen in Figure 5.3.4, which considers the reflections at a T-junction in a microwave

waveguide. Once it is extended to the geometry of the experiment, it should allow quantitative determination of the sensitivity factor. Note that the relative size of the wavelength in comparison to the dimensions of the waveguide is expected to alter the reflectance. This is expected to give rise to interference effects.

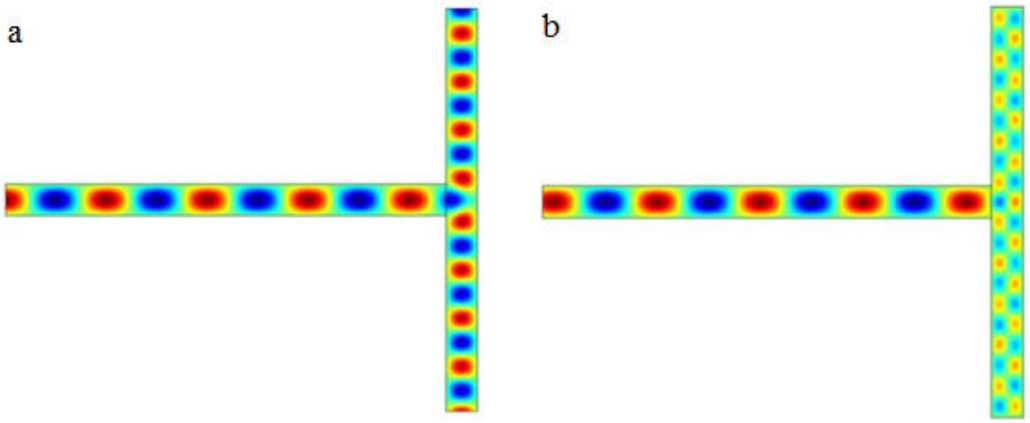

Figure 5.3.4: Modelled electric field in a T-junction of a microwave waveguide. a) corresponds to a dielectric constant of 2, whereas b) corresponds to a dielectric constant of 5.

To a first approximation, the effects of leaking are expected to be constant throughout each measurement, provided that the sample is not moved, and any change in reflected power originates from the photo-induced conductivity. A model based on equations 5.3.1 and similar to that of Kunst and Beck[50], which was implemented by Dr Stephen Bingham (Department of Physics, University of Bath), considered stacks enclosed in a waveguide which could be terminated or not. First of all, the model was tested by reproducing plots of the reflectance as a function of conductivity for silicon (figure 2 of Kunst and Beck[50]) see Figure 5.3.5 (a). Then, by varying the conductivity of the TiO_2 layer over the range expected for operation of the DSC, i.e. from 10^{-6} to 10 S/m, the modelled change in conductivity with respect to a dark value, taken to be 10^{-8} S/m, was calculated, and found to be linear over this range. In Figure 5.3.5 (b), the absolute values have been plotted due to the change in reflectivity decreasing with increasing conductivity. Since in our experimental set up the waveguide was neither truly terminated nor open ended, the model was used to predict the change in reflectivity as a function of conductivity for both cases, and no difference was observed over the range of interest.

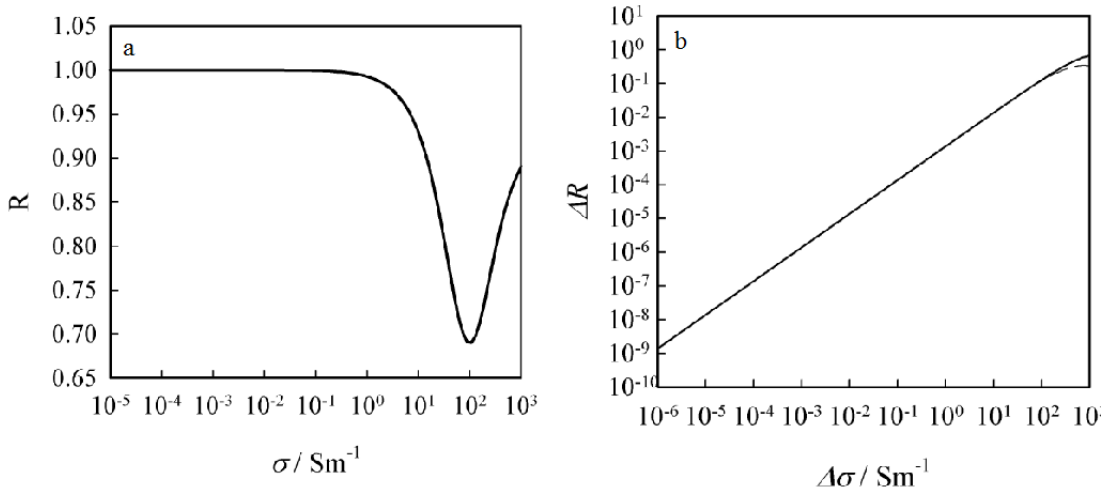

Figure 5.3.5: a) Calculated reflectance as a function of Si conductivity, b) calculated change in reflectance of a 13 μm TiO_2 film as a result in a change in conductivity brought on by illumination when the waveguide is terminated with a short (solid line) and open (dashed line). Parameters used for a) ε_r=12 and the sample thickness *d*=300 μm[50]. Parameters used for b) can be found in appendix B.

Since the relationship between the change in conductivity and the change in reflected power is linear over the range of interest, the sensitivity factor is expected to be constant, and equation 5.2.2 should be valid. The sensitivity factor was calculated with equation 5.2.3, and was found to be approximately 0.48 Ωcm. However, this value does not take into account the leakage of power due to the imperfect termination. It should, however, place an upper estimate on the real sensitivity factor for our system, since the same change in conductivity will lead to a smaller reflected power.

5.4 *First steps in microwave reflectivity on TiO_2*

5.4.1 Microwave components.

This section describes those components of the microwave set up which do not relate to aspects of the set up optimisation discussed in section 5.5.3.

The microwave source used in this study was a 33 GHz Gunn diode connected to a rectangular waveguide of inner dimensions of approximately 7 by 3.5 mm. The Gunn effect, discovered in 1963, is the generation of oscillations when a potential

difference of several thousand V/cm is applied across a GaAs or InP n-type semiconductor. It corresponds to a range of applied voltages of negative differential resistance, caused by the transfer of conduction band electrons from one satellite valley to another[25]. Figure 5.4.1., which shows the current-voltage characteristics for the Gunn diode used throughout this study, indicates that microwaves are only generated in the region of negative resistance, after an applied potential of approximately 3 V.

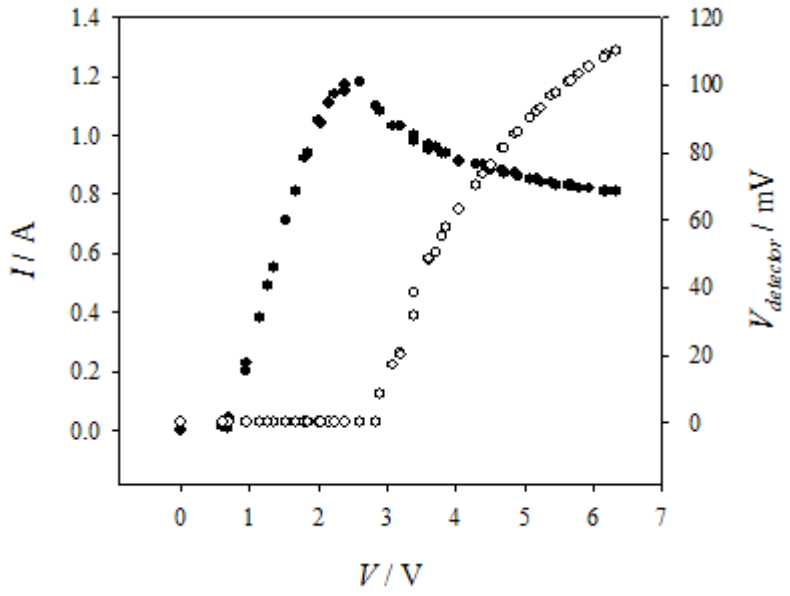

Figure 5.4.1: Current-voltage characteristics of the Gunn diode, showing the area of negative resistance after ~2 V applied(filled symbols). Power emanating from the Gunn diode as a function of applied potential, which only occurs in the region of negative resistance (empty symbols).

An isolator is a device which blocks microwaves in one direction, while allowing them to pass in the other. It is used to protect delicate elements, such as the Gunn diode, from reflections.

A directional coupler, illustrated in Figure 5.4.2, is a four-port device, consisting of two parallel channels, separated by openings which allow a certain proportion (in this case 7.5%) of the power in the lower channel to pass into the upper channel. The source and the sample are at either ends of the lower channel, meaning that the small amount of power from the source which enters the upper channel is directed to a microwave absorbing material. Of the power reflected by the sample, 7.5% will

reach the detector which is connected to the opposite termination of the upper channel. The rest will travel down the wave guide in the opposite direction, and will be absorbed by the isolator.

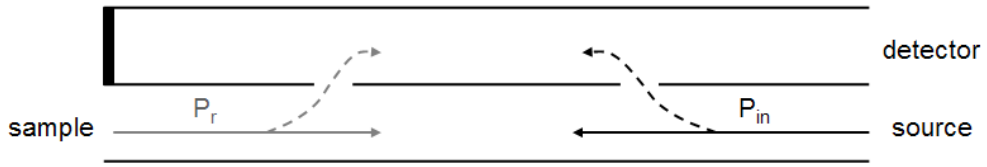

Figure 5.4.2: Schematic representation of a directional coupler, see text for details.

5.4.2 Preliminary measurements.

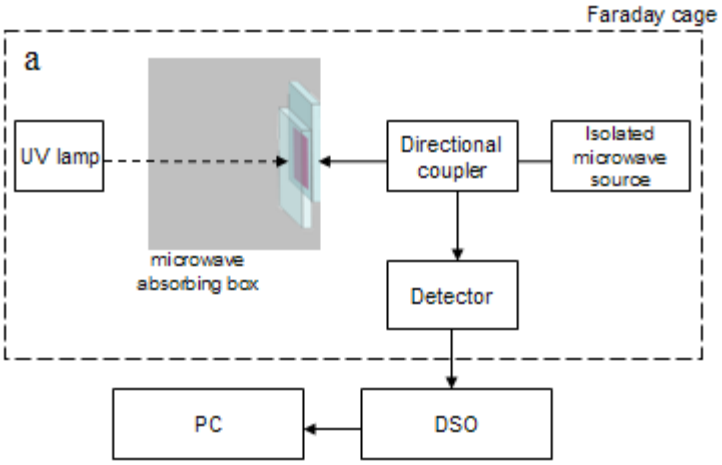

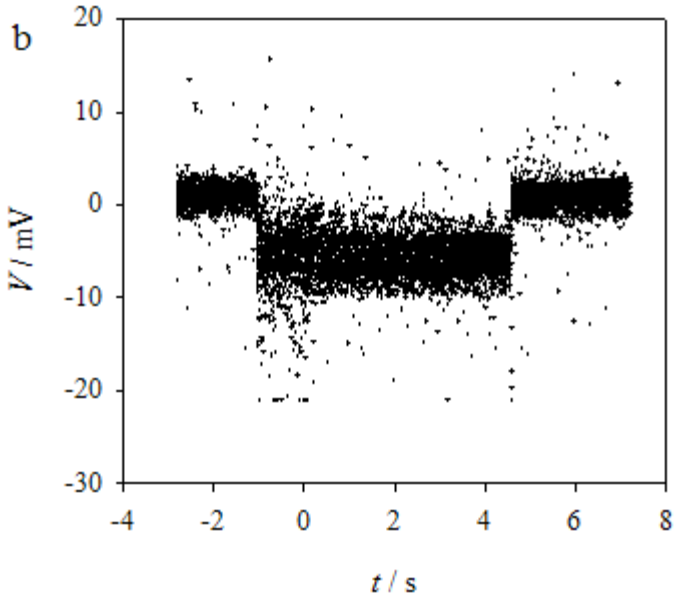

Figure 5.4.3: Set up for the measurement of the conductivity of bare TiO_2 as a result of UV illumination, and corresponding transient.

The first measurement of an illumination-induced change in microwave reflectance was obtained on a sample of porous TiO_2 on plain glass under UV illumination. This sample was chosen because it did not require the TiO_2 to be dye-sensitised, thus eliminating issues of dye degradation when exposed to the atmosphere. Figure 5.4.3 illustrates the simple set up used to obtain the first microwave reflectance transient. The microwave source is a 33 GHz Gunn diode which is protected by an isolator, to prevent reflected waves from damaging it. The cell is mounted directly on the end of the waveguide, and a directional coupler channels the reflected microwaves to the R422C crystal detector (Agilent technologies). The directivity of the directional coupler was measured to be 7.5%, meaning that of the power reflected by the sample, 7.5% of it will reach the detector. The UV lamp was turned on and off manually, and the resulting transients were recorded on a Tektronix TDS 3012 digital storage oscilloscope (DSO). The sample is housed in a box made of microwave absorbent material to minimise stray reflections from metallic materials in the surroundings. However, the box was not closed, so as to allow illumination.

Similar experiments were then attempted with dyed TiO_2 on plain glass under green light, but no change in conductivity was detected. It was thought that in the absence of electrolyte, the electron concentration was too low. Hence electrolyte was introduced; "etched" cells, as described in chapter 3, were made, and to begin with, no change in conductivity was measured in the set up described in Figure 5.4.3 as a result of illumination with green light. However, by modulating the illumination intensity it was possible to measure very small changes in reflected power using a Stanford Research Instruments SR 83 DSP lock in amplifier. The frequency was swept from 0.1 Hz to 1 kHz. The experimental set up and the Nyquist plot obtained, showing a very plausible electron lifetime of 200 ms, are displayed in Figure 5.4.4.

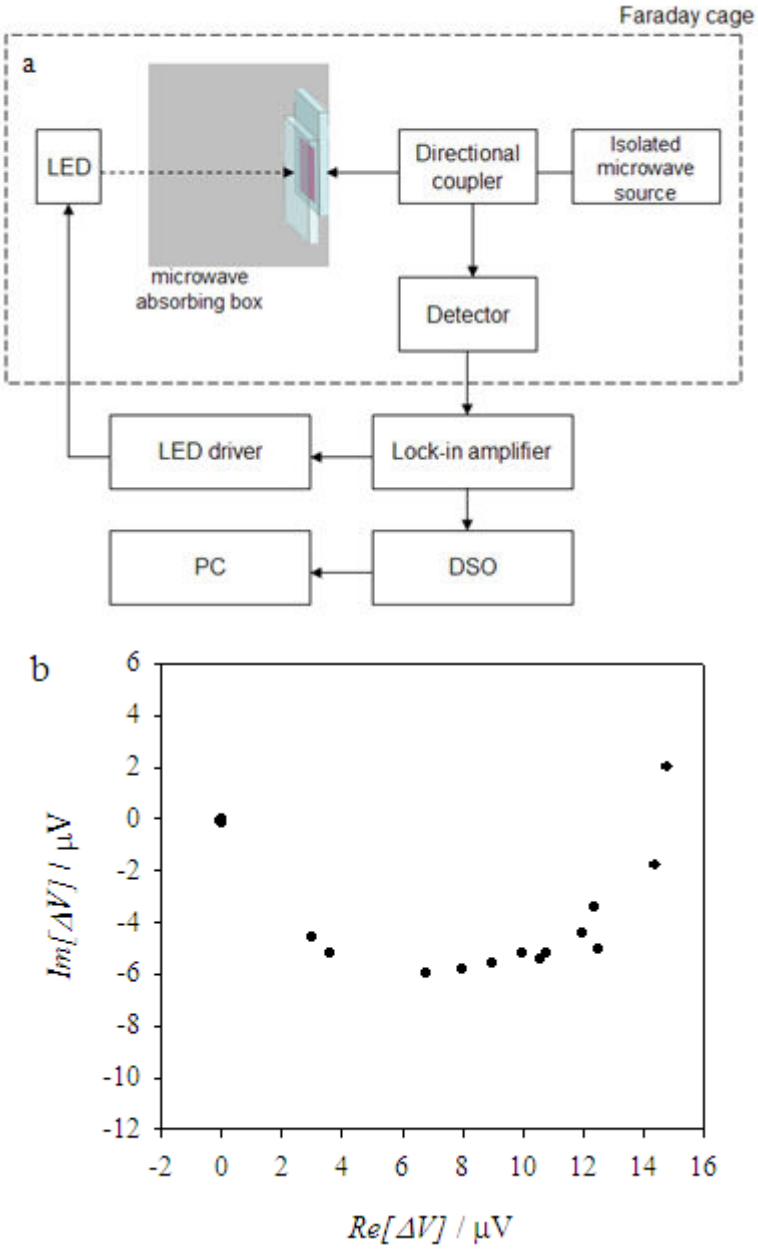

Figure 5.4.4: a) Experimental set up used to obtain the first evidence of visible light-induced change in conductivity of sensitised TiO_2, and associated Nyquist plot b).

Having ascertained that changes leading to signals of the order of a few microvolts were taking place under visible illumination, a new set up to attempt to measure time resolved transients was built, and is described in Figure 5.4.5, along with an example of a transient obtained. Amplification of the detector output prior to subtraction the background reflectivity, using a Stanford Research Instruments SR 560 low noise preamplifier, allowed the latter to be more accurately compensated for. It was then possible to amplify the remaining light-induced signal using a second preamplifier, and average the result on the DSO. In this case, the signal was averaged 150 times,

and the light intensity was of the order of 10^{16} $cm^{-2}s^{-1}$. A PPR1 pulse generator was used to turn the LED on and off.

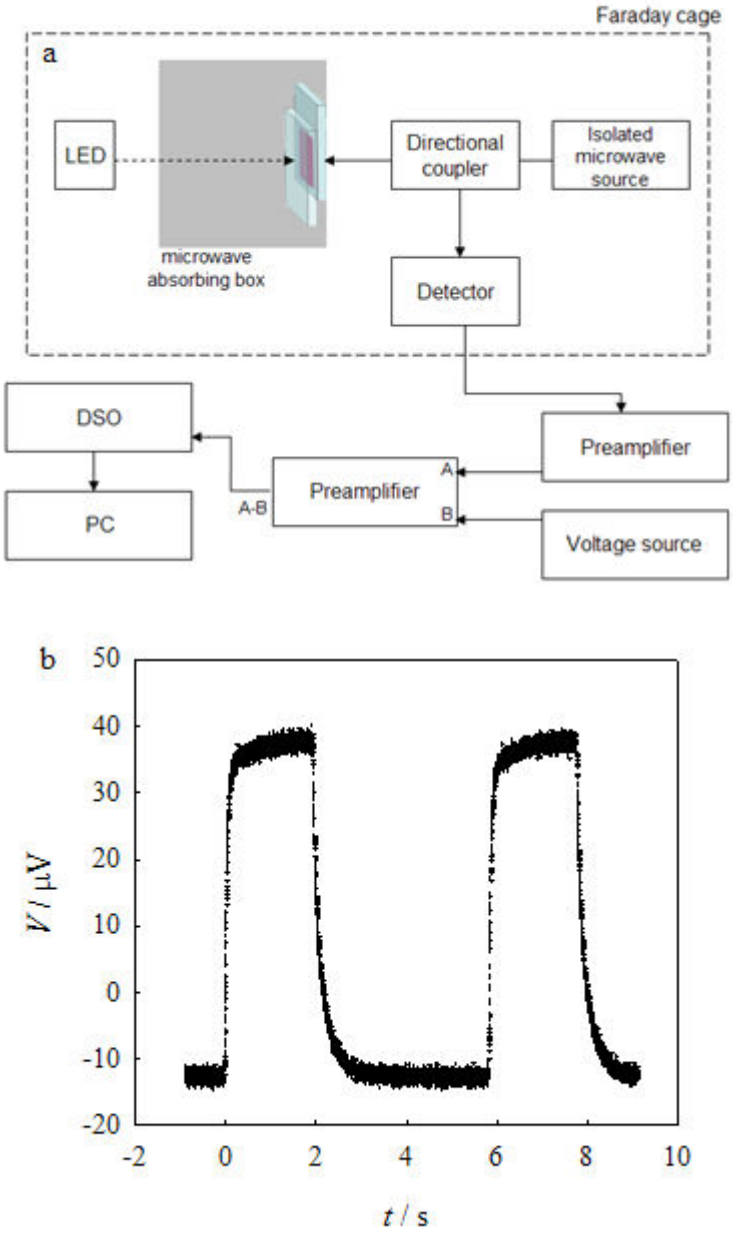

Figure 5.4.5: a) Experimental set up and b) microwave reflectivity transient recorded in a light on light off experiment.

5.5 *Optimisation*

5.5.1 Cell design.

For the purpose of these measurements, the DSCs described in chapter 3 had to be modified to fit certain requirements. The main limitation is that since the microwaves would interact with any conductor, there could be no FTO between the microwave source and the active part of the cell, namely the TiO_2. Indeed the first measurements were made on cells which were constructed exactly as those described in chapter 3, except they were made using plain glass instead of FTO. This would mimic a cell at open circuit, with an ideal blocking layer. To get an idea of the photovoltage which would be expected in these cells, identical cells were made on FTO and their photovoltage was measured under the same illumination intensity. This was further improved by making cells on FTO with a window etched in the FTO which could be aligned with the waveguide end. This allowed the free electron density and photovoltage to be measured simultaneously. It should be noted that the quasi Fermi level in the cell over the etched and non etched areas of the substrate is expected to be the same provided that back reaction via the FTO is negligible, which is why a blocking layer was used.

To verify that the quasi Fermi level remains unchanged by etching off the FTO, IR transmittance was used to measure the total electron density in two identical cells, one of which had an etched window, and the other was normal. It can be seen in Figure 5.5.1 that there is a good agreement between the two cells, indicating that at open circuit, the quasi Fermi level is unchanged by the removal of FTO. However the IR spot used covered an area which did not fit solely on the etched patch, so it is not exactly indicative of the quasi Fermi level precisely in one area or the other. For this reason, an experiment using a scanning IR laser is planned at the National Physics Laboratory, NPL, which will measure the total electron density across the boundary between the etched and un-etched areas, which will give detailed insight into the effect of removing the FTO on the quasi Fermi level. In conjunction with measurements of the total electron concentration, the harmlessness of the etched patch can be demonstrated by comparing the photovoltage of identical cells with and without the etched patches. It was found that they were in good agreement, within the variation expected of nominally identical cells.

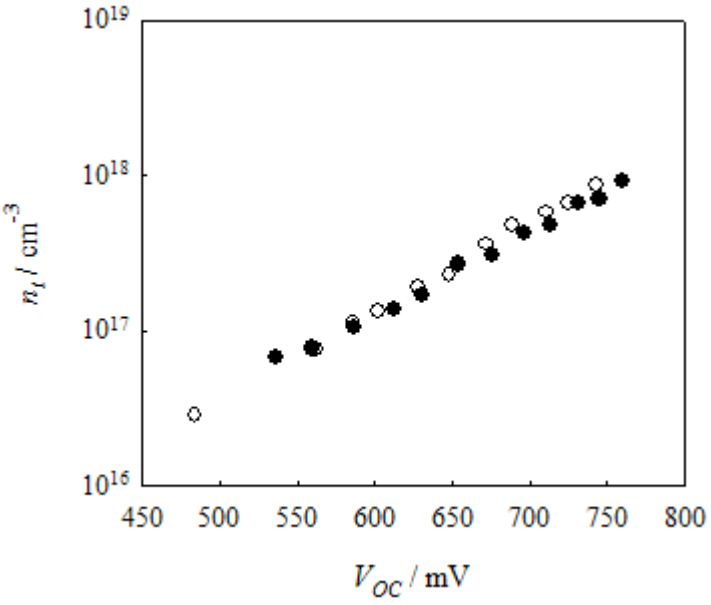

Figure 5.5.1: Voltage dependence of the total electron density determined by IR transmittance spectroscopy of a normal cell (open symbols) and a window cell (filled symbols).

5.5.2 Active area positioning and back reflection.

It was noted that the amplitude, and sign, of the reflected microwave signal changed when cells were constructed with glass of different thicknesses. Although this observation was initially puzzling, it was realised that this could be due to the active area of the cell (i.e. the porous TiO_2) being at a different point of the wave, and so the distance between the active area and the waveguide end was systematically changed by adding pieces of glass. the results from this study can be seen in Figure 5.5.2. Since the distance was only changeable by adding glass with a discrete thickness, it was impossible to finely tune the distance to get the strongest achievable signal. The periodic guide to the eye which has been added is only put forward as an illustration of what the trend may be. It is possible that interference between the incident and reflected microwave are causing these changes in detected signal, depending on the position of the active area within the wave. The wavelength of the microwaves in air should be approximately 1cm. The wavelength of the guide to the eye in Figure 5.5.2 is approximately 3 mm, consistent with the microwaves passing through a medium of refractive index 3.

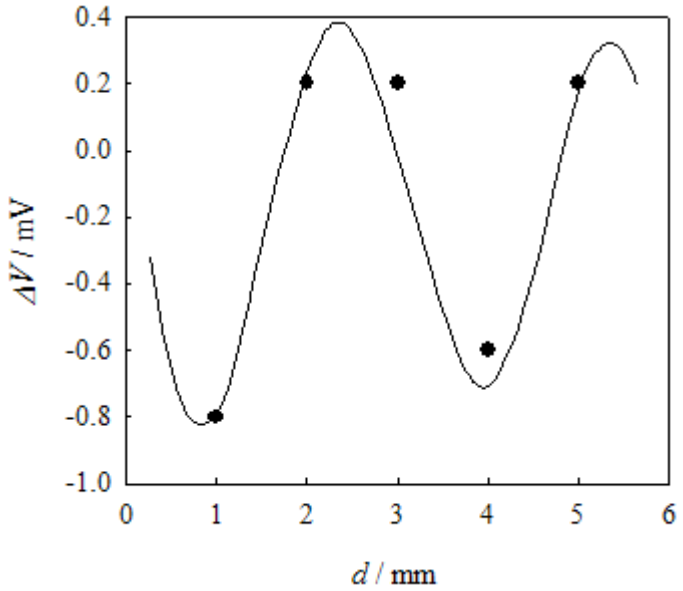

Figure 5.5.2: Change of the magnitude and the sign of the change in reflected signal due to an illumination of *ca.* 10^{-17} $cm^{-2}s^{-2}$ for different distances between the TiO_2 and the waveguide end. A periodic guide to the eye with a wavelength close to that expected for the microwaves in glass has been added to illustrate the possibility that this effect is due to interference effects due to the TiO_2 being located at different points along the wave.

Furthermore, an FTO-coated glass slide was positioned after the active area, which further improved the signal. This could either be due to the extra power passing through the sample, or perhaps the FTO acts as a short, creating a node, and therefore a maximum may occur near the active area, thus increasing the signal.

Figure 5.5.3 summarises the effect of altering the position of the active area, and of the metallic short. It can be seen that there is very little difference in the variation of the reflected signal with light intensity, only the absolute magnitude changes. Given the difficulty in detecting such small signals, the design giving the highest magnitude was adopted. This consisted of a single glass slide acting as the spacer between the active area and the waveguide end, and an FTO-coated slide being used to seal the cell, resulting with 1mm distances between the waveguide end, the active area, and the short.

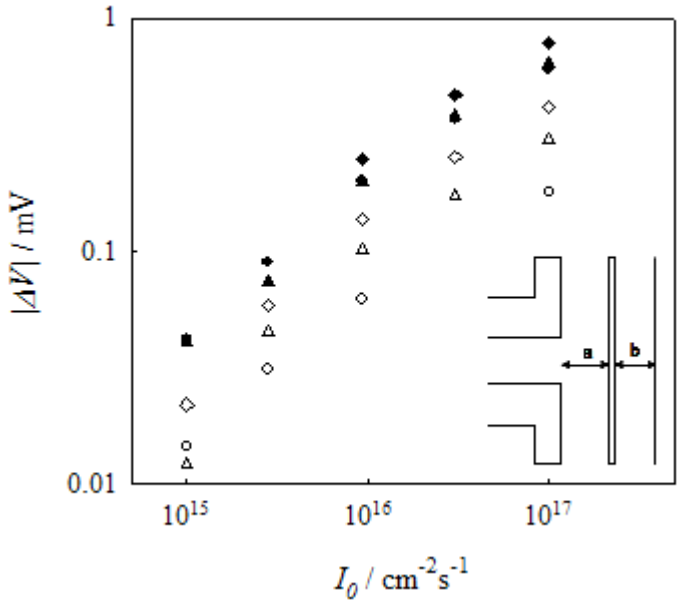

Figure 5.5.3: Effect of altering the distance between the waveguide end and the active area, a, and the distance between the active area and the metallic short, b. The filled symbols represent a = 1 mm, while the empty symbols represent a = 2 mm. In each case the diamonds correspond to b = 1 mm, the triangles, b = 2 mm, and the circles, no metallic short.

5.5.3 Improvements to the waveguide

To further improve the detected signal, a high speed pin diode switch (Atlantic Microwaves) was used to modulate the incident microwave power. The TTL output of the lock-in amplifier was used to drive the switch at a frequency of 32.63 kHz, and the same lock in was connected to the detector output. The resulting microwave signal was a square wave, with a modulation depth of 100%, as can be seen in Figure 5.5.4 (b).

The detector does not maintain a linear relation between input power and output voltage over its whole operating range. An attenuator was added to the waveguide to maintain the measured background reflected power within a reasonably linear region. Figure 5.5.4 (a) illustrates the almost linear relationship between input power and output voltage in the region the experiments were performed, while the inset in shows the non-linear behaviour observed at high powers. It should be noted that no significant error is expected to be introduced by the slight non-linearity of the detector response, since the quantity of interest is the ratio between the reflected

power under illumination and that in the dark, and the difference between them is at most tens of microvolts.

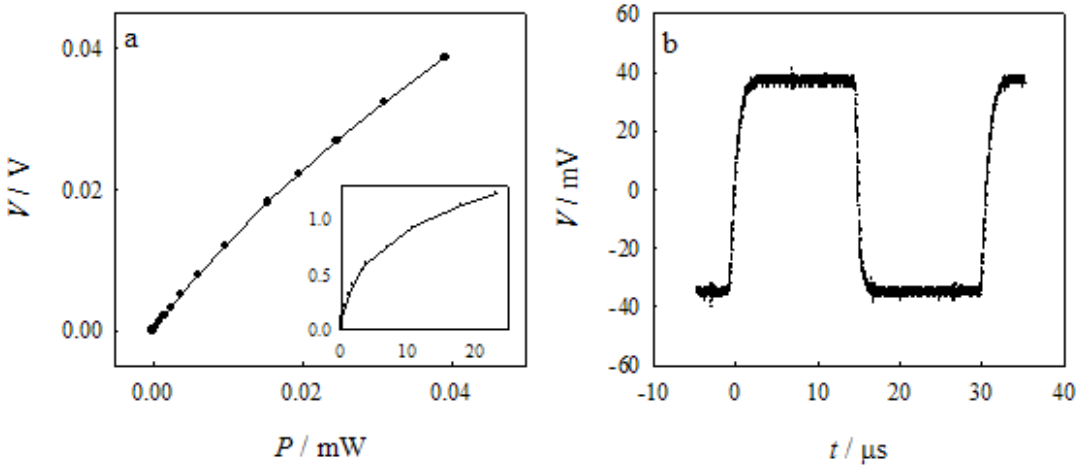

Figure 5.5.4: a) Voltage response of detector to power over the range of dark reflected powers measured in the experiments, inset shows the saturation of the detector at higher powers, axis labels are the same. b) Chopped incident power in the microwave waveguide.

5.5.4 Optimised experimental set up

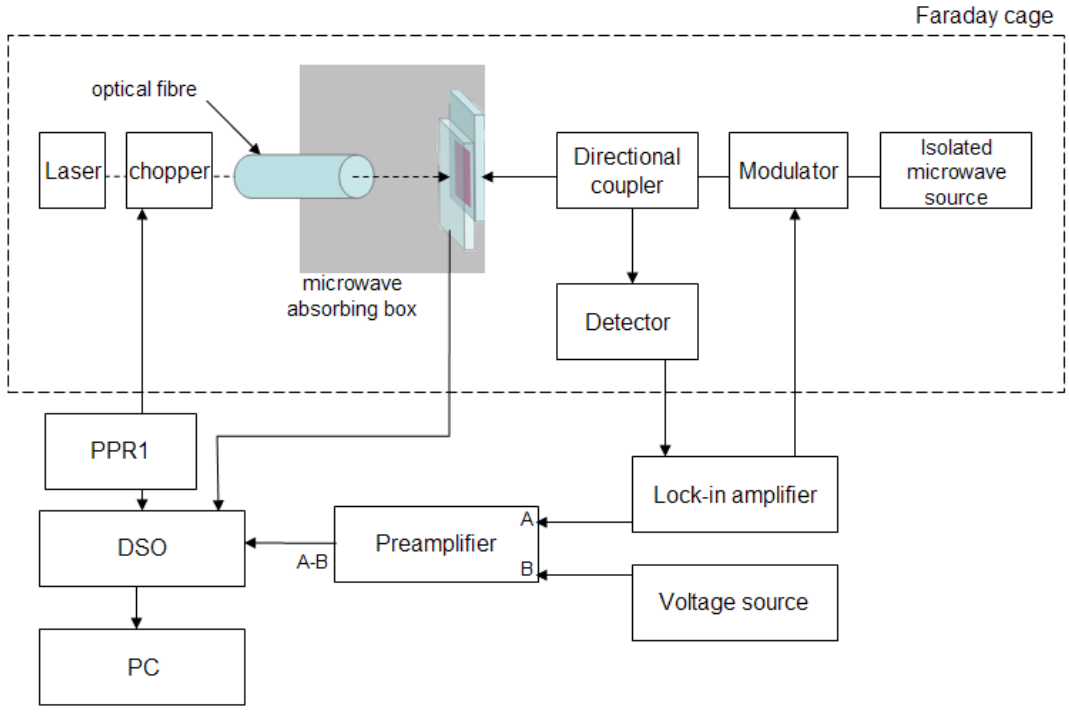

Figure 5.5.5: Optimised experimental set up for measurements of light-induced change in conductivity of TiO_2 by microwave reflectivity.

Figure 5.5.5 shows the optimised experimental set up for time resolved microwave reflectivity on DSSCs. A fast switching modulator is incorporated in the waveguide to allow lock-in detection of the reflected signal, which is at most a few milivolts. The waveguide also comprises of an added attenuator, whose purpose is to keep the reflected signal within the linear operating range of the detector.

The crystal detector's output is fed into a Stanford Research Instruments SR 83 DSP lock in amplifier, whose reference signal (32.63 kHz) is used to modulate the microwave signal. A Stanford Research Instruments SR 560 low noise preamplifier was used to offset the dark reflectance of the cell from the lock-in output. The light-induced change in reflectance is then recorded on a Tektronix TDS 3012 digital storage oscilloscope (DSO), capable of averaging up to 512 frames. A PPR1 square wave generator is used to chop the green laser light which is incident on the DSC. The same TTL signal is used to trigger the DSO. The DSC is housed in an improved box made of microwave absorbent material to minimise stray reflections from metallic materials in the surroundings. For this reason, fibre optic of diameter 1 mm is used to introduce light from the green laser onto the cell. Before entering the fibre optic, the light is chopped and the intensity is adjusted by the use of neutral density filters.

Depending on the signal strength, 5-30 frames would be averaged for each measurement, which consists of the change in reflected microwave power, and the photovoltage of the cell, measured simultaneously for a given light intensity.

A typical dataset can be seen in Figure 5.5.6, where the raw data (a) measured at various light intensities is used to construct the plots in (b), (c) and (d). The expected trends for plots (b), (c) and (d) are summarised below, along with the assumptions made.

Semi logarithmic plots of $\Delta P_r / P_r$ versus V_{OC} are essentially a representation of the Boltzmann equation, and as such are expected to be linear, with a slope of $1/k_BT$ provided that:

- The change in conductivity is linearly proportional to the change in reflected microwave power, i.e. the sensitivity factor, *S*, and the electron mobility are constants.
- The conduction band position relative to the redox Fermi level of the electrolyte does not change.

Double logarithmic plots of $\Delta P_r / P_r$ versus I_0 are an expression of;

$$n_C = \frac{\eta_{inj}\eta_{col} I_0 \tau_0 \left(1 - \exp(-\alpha d)\right)}{d},$$

5.5.1

which is derived from the balance between the rate of injection and back reaction. These plots should be linear with a slope of one provided that:

- The change in conductivity is linearly proportional to the change in reflected microwave power, i.e. the sensitivity factor, *S*, and the electron mobility are constants.
- Back reaction of photo-injected electrons is first order in electron concentration, and occurs only via the conduction band.
- The light harvesting, injection and collection efficiencies are independent of light intensity.

Semi logarithmic plots of V_{OC} versus I_0 are expected to be linear with a slope of $1/k_BT$ provided that:

- Back reaction of photo-injected electrons is first order in electron concentration, and occurs only via the conduction band.
- The light harvesting, injection and collection efficiencies are independent of light intensity.
- The conduction band position relative to the redox Fermi level of the electrolyte does not change.

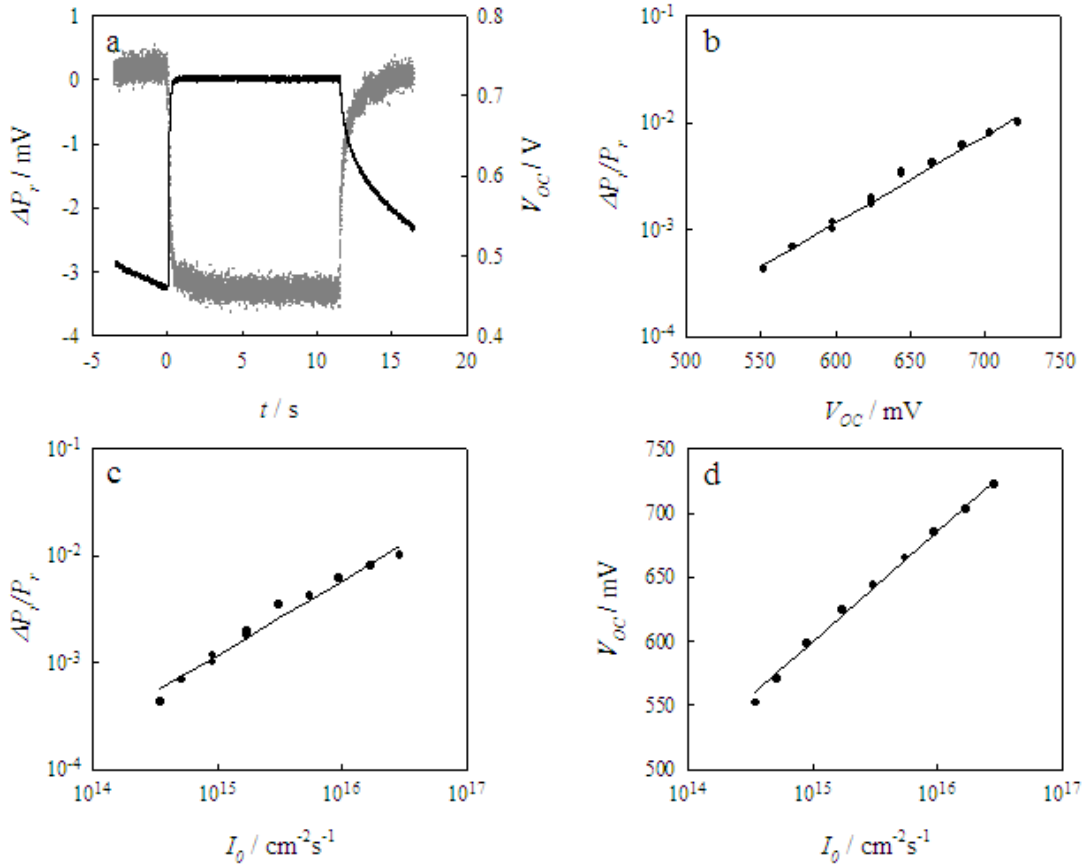

Figure 5.5.6: a) Conductivity (grey) and photovoltage (black) transients measured simultaneously on a window cell (cell E32). The light intensity was 10^{17} cm^{-2}s^{-1}, and the electrolyte comprised of 0.5M LiI, 0.05M I_2 and 0.5M TBP in 3-methoxy propionitrile. b) Variation of photoconductivity with open circuit photovoltage. c) Variation of photoconductivity with light intensity. d) Variation of photovoltage with light intensity.

The first unexpected observation made on these data sets is that none of the trends are perfectly linear. Plots such as that in Figure 5.5.6 (c) are distinctly curved for all cells in this study. The curvature of plots such as (b) and (d) is less pronounced, and in a few cases they have been found to be linear. The second observation is that none of the slopes of the trends, ignoring the slight curvature, correspond to the expectations listed above. This should not come as too much of a surprise, since plots of V_{OC} versus I_0 are a routinely found to have slopes greater than expected, which is often dealt with by including an empirical non ideality factor, m, in the Boltzmann equation.

In the following chapter, we will attempt to elucidate the cause of the non-ideality and explore possible origins for the curvature seen in plots (b), (c) and (d).

6 Microwave reflectivity as a tool to provide further insight into the inner workings of DSCs.

6.1 *Introduction.*

Microwaves are electromagnetic waves with very low energy, and are therefore suitable to probe electrons located in the conduction band or in very shallow traps. When microwaves are incident on a conducting sample, the reflected power is related to its conductivity, and assuming a constant mobility, to the free electron concentration, n_c. Microwave reflectance has been used to measure conductivities in isolated nano-porous TiO_2 with and without adsorbed dyes, but never in a working DSC.[41, 62]

In the previous chapter, we demonstrated that microwave reflectivity could be applied to a working DSC under open circuit conditions. This is an important step forward in the characterisation of DSCs, since n_c is a key parameter in DSC theory, although it has remained un-measurable until now. Figure 5.5.6 summarises the data sets which are obtained with this technique, and has been reproduced to facilitate referencing.

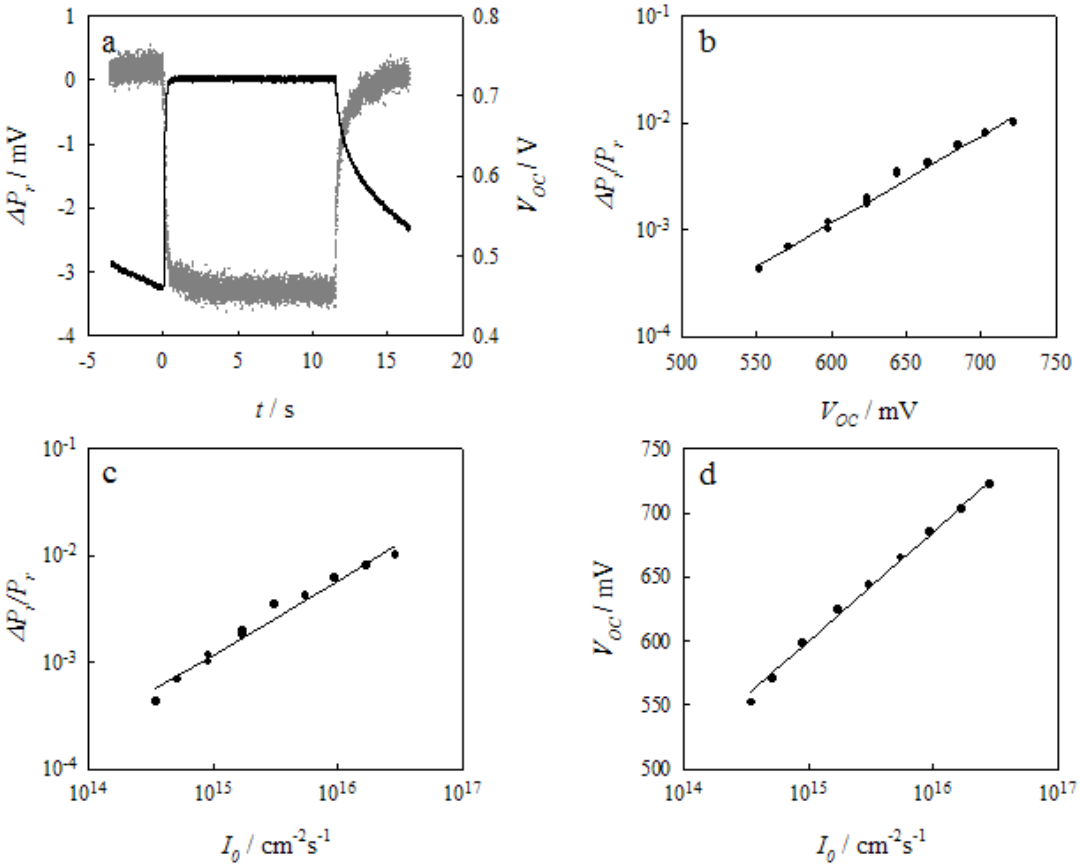

Figure 6.1.1: a) Reflected microwave signal (grey) and photovoltage (black) transients measured simultaneously on a window cell (cell E32). The light intensity was 10^{17} cm^{-2}s^{-1}, and the electrolyte comprised of 0.5M LiI, 0.05M I_2 and 0.5M TBP in 3-methoxy propionitrile. b) Variation of microwave reflectivity with open circuit photovoltage. c) Variation of microwave reflectivity with light intensity. d) Variation of photovoltage with light intensity.

Several interesting observations on these data were noted in the previous chapter, namely that similarly to the well-documented non-ideal behaviour of the photovoltage with light intensity, variations of the microwave reflectivity – which is thought to be proportional to the free electron concentration – with light intensity and photovoltage are also non-ideal. Furthermore curvature is observed in the trends of Figure 5.5.6 (b), (c), and (d), for which there is no obvious *a priori* explanation.

The objectives of the present chapter are four-fold. Firstly attempts are made to explain the surprising findings presented in the previous chapter, and summarised above. Secondly, the effect of the electrolyte composition on the free electron concentration is investigated as an indirect means to probe the electron lifetime. Thirdly a light-modulated microwave reflectivity setup operating in the frequency

domain is presented, which allows measurement of the apparent electron lifetime. This is found to be in good agreement with that obtained by IMVS, which provides reassurance that the microwave reflectivity technique is indeed a measure of the free electron concentration. Finally, preliminary work on measuring the free electron concentration at short circuit is introduced, and although it was not possible to measure the free electron concentration at short circuit due to time limitations, there was very encouraging evidence that this could in principle be achieved.

6.2 *Exploring the unexpected.*

As was mentioned previously, several unexpected observations were made. The first to be investigated is the origin of the curvature in the plots of the free electron lifetime as a function of the photovoltage and light intensity, shown in Figure 5.5.6 b) and c), respectively. An independent measurement of the TiO_2 conductivity across a gap between two electrodes allows this curvature to be explained by a non-constant sensitivity factor between the reflected microwave signal and the conductivity. Then, we will show that the non-ideal behaviour obtained in the plots of the free electron density as a function of the photovoltage and light intensity, shown in Figure 5.5.6 b) and c), respectively, combine to make the well-documented non-ideality in the variation of the photovoltage with the light intensity, as in Figure 5.5.6 d). Finally, we will explore some possible physical explanations for these non-idealities in the way the free electron concentration scales with the light intensity and the photovoltage.

6.2.1 Investigating the origin of the curvature.

As discussed in chapter 2, the free electron concentration should scale linearly with light intensity, provided the back reaction of photogenerated electrons with I_3^- is pseudo first order in electron concentration and occurs only via the conduction band.

$$n_C = \frac{\eta_{inj}\eta_{col}I_0\tau_0\left(1-\exp\left(-\alpha d\right)\right)}{d}$$

6.2.1

From Chapter 5, the free electron concentration should depend on the change in microwave reflectivity according to;

$$\frac{\Delta P}{P(\sigma)} = Sq\mu\Delta n_c .$$

6.2.2

Provided equation 6.2.2 holds, and S is constant, the change in microwave reflectivity should scale linearly with light intensity. However, the double logarithmic plot of $\Delta P_r / P_r$ versus I_0 seen in Figure 5.5.6 is curved, indicating that the measured change in reflectance does not scale linearly with light intensity. De-convoluting the origin of this non-linear behaviour requires consideration of the equalities which link the change in reflectance to the light intensity.

Firstly, the expression linking the free electron concentration to the light intensity, equation 6.2.1, was scrutinised. Although the parameters in this equation are usually considered constant, it is not inconceivable that they could be changing. Indeed, Koops *et al.*[16] have reported electron injection efficiencies changing as the bias voltage becomes high, arguing that the driving force for injection becomes smaller. The same effect could be present in this case, as the light intensity increases, and the quasi Fermi level becomes closer to the conduction band. Furthermore it has been shown recently by Bisquert *et al.*[24] that the free electron lifetime is dependent on the electron concentration. Another possibility could be that back reaction is not only occurring via I_3^-, but also via the oxidised dye cation, which would be more pronounced at higher light intensities, as the local concentration of iodide would become depleted. However if the origin of the curvature were to lie in the relationship between the free electron concentration and the light intensity, plots of $\log(\Delta P_r / P_r)$ versus V_{OC} would be linear, which is not the case. Therefore it seems more likely that the curvature originates in the relationship between the free electron concentration and the microwave reflectivity.

On inspection of equation 6.2.2, two parameters could be non-constant; the sensitivity factor or the electron mobility. The electron mobility, which is usually assumed to be constant, is related to the conduction band diffusion coefficient by the Stokes-Einstein relation;

$$\mu = \frac{q}{k_B T} D_0$$

6.2.3

However, Kroeze and co workers[41] have made observations of microwave conductivity consistent with a decrease in the effective inter-particle electron mobility, which they have attributed to electron-electron interactions because the change occurred at an electron density of one electron per particle. Since this study also used a microwave reflectivity technique in which a constant sensitivity factor was assumed, this evidence does not seem compelling enough to justify variations in mobility as the origin of the curvature in these plots.

Although the conductivity of the TiO_2 (calculated in the previous chapter) was found to lie within a range where the modelled sensitivity factor is constant, given the unexpected curvature in the plots it was deemed preferable to obtain an independent measurement of the conductivity. The conductivity of porous TiO_2 has been measured by forming a bridge of porous TiO_2 between two electrodes separated by a gap of width ranging from 5 to 200 μm by several research groups.[45, 73 37] The study which covers the experimental conditions closest to our work is that of Abayev *et al.*.[37] They report values of conductivity ranging from 10^{-8} to 10^{-1} Sm^{-1} over a range of applied potentials corresponding to normal operating conditions of a DSC. Interestingly, they report a saturation of the conductivity above -0.5V vs Ag/AgCl – corresponding to V_{OC} ~800 mV – whereas Agrell *et al.*[73], who investigated the conductivity at potentials higher than ordinary operating conditions of a DSC device, did not observe such a saturation. This is likely to be due to the different electrolyte compositions used in these studies. Unlike the aforementioned studies, Petrozza *et al.*[45] measured the photoconductivity in dry TiO_2 electrodes, and found values within the range reported by Abayev *et al.*. Since measurements of the TiO_2 conductivity when immersed in electrolytes similar to those used in our study were not found in the literature, DSCs with a gap in the working electrode were prepared – see Figure 6.2.1. In all other respects, the cells were prepared exactly the same as the "normal cells" described in Chapter 3, the electrolyte used was H2.

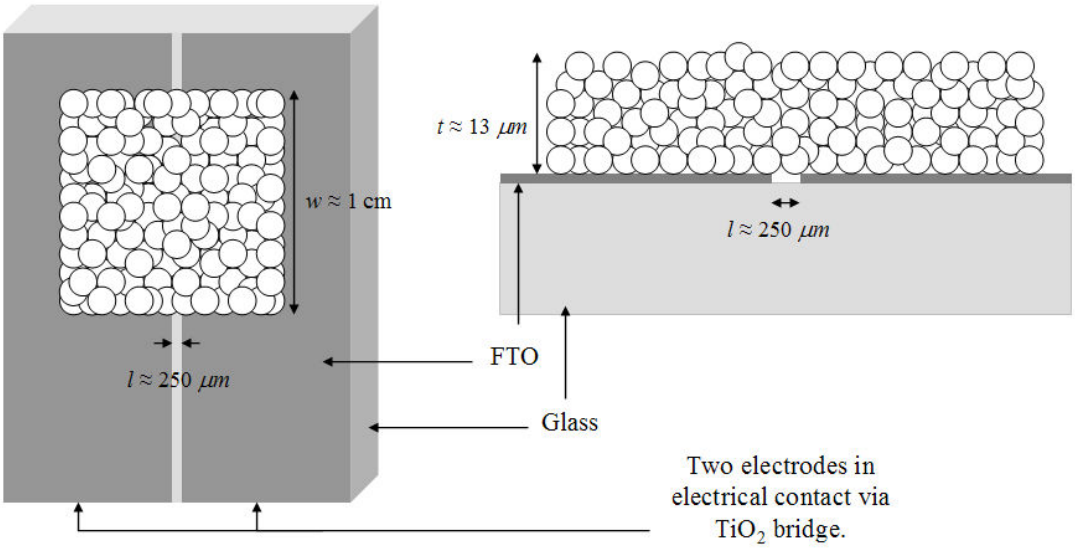

Figure 6.2.1: Top and side view of the samples prepared with a gap in the FTO in order to measure the conductivity of porous TiO_2.

The cell was held under illumination, and the photovoltage was recorded between the counter electrode and one of the two working electrodes. The cell's two working electrodes are then contacted to an Autolab potentiostat in two electrode mode. A potential is applied between the electrodes, and the resulting current is measured. By sweeping the applied potential, it was observed that the *i-V* curve, shown in Figure 6.2.2 a), displays ohmic behaviour for potentials between +/-0.075 V. The conductance was obtained from the slope of the i-v curve in the ohmic region, and was used to calculate the conductivity based on the geometry of the device illustrated in Figure 6.2.1:

$$\sigma = \frac{l\Delta I}{wt\Delta V} \qquad \textbf{6.2.4}$$

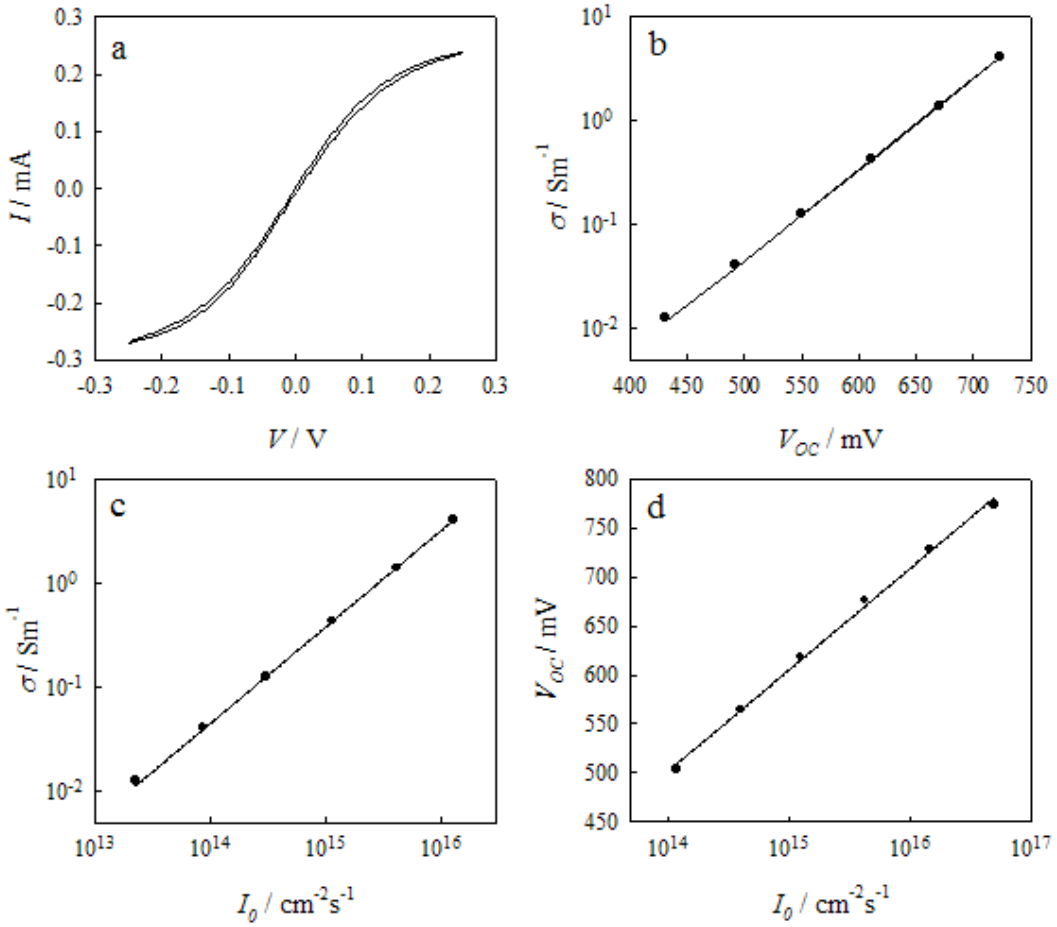

Figure 6.2.2: a) Cyclic voltammogram across the gap electrode (cell 5) measured under illumination, leading to a photovoltage of 720 mV. The slope of the straight part of the curve around 0 V gives the conductance of the TiO_2. The measurement is repeated at different light intensities and the open circuit voltage at each light intensity is recorded, so that the conductivity can be plotted against; b) the photovoltage, or c) the light intensity. d) Also shown is a plot of the photovoltage as a function of light intensity.

The most striking observation that can be made from Figure 6.2.2 is that there is no curvature in the plots of the conductivity versus the light intensity and the photovoltage. This demonstrates that the curvature in the plots of the change in microwave reflectivity versus these same parameters – see Figure 5.5.6 – is not due to an intrinsic property of the DSC. Instead, it is most likely due to the sensitivity factor, *S*, not being a constant, which is consistent with the fact that the conductivities measured across the FTO gap are much larger than those calculated in Chapter 5, because a non constant sensitivity factor is predicted at higher conductivities. It should be noted that the precise geometry of the gap is not formally known, particularly the thickness of the gap, which was determined purely

by visual inspection. Hence the absolute values of conductivity could differ by some factor. However the change in conductivity with the quasi Fermi level position is unaffected by this uncertainty.

Since the plots of $\log(\Delta\sigma)$ versus V_{OC} and $\log(\Delta\sigma)$ versus $\log(I_0)$ are both linear, plots of V_{OC} versus $\log(I_0)$, such as Figure 6.2.2 d), should also be linear. However this is not the case, and most plots measured as part of the microwave study also show a slight curvature. The origin of this is not clear, but it is thought that this could be due to slight inaccuracies in the measurement of the light intensity. Indeed the response of the photodiodes used to calibrate the light intensity start to saturate at high light intensities – above 10^{16} $cm^{-2}s^{-1}$ for the particular photodiode used throughout this work. To overcome this, the highest light intensities are calculated based on the transmission of the filters used to achieve them. However, there may be some variation in the transmission of individual filters, which could lead to inaccuracies in this method of determining the higher light intensities. Naturally, this should also impact on plots of $\log(\Delta\sigma)$ versus $\log(I_0)$, which are found to be linear when measured across a gap. This can be explained by noting that when the photoconductivity is plotted against the light intensity, as in Figure 6.2.2 b), the light intensity was calibrated separately, and was thus obtained from fits of photovoltage versus light intensity, as in Figure 6.2.2 d).

Having clarified the origin of the curvature in plots of $\log(\Delta P_r / P_r)$ versus V_{OC} and $\log(I_0)$, it is noted that the overall non ideality remains in the data measured with the gap technique, indicating that there are some forms of non-ideal mechanisms in DSCs. In this particular example, the non ideality factor *a*, from the plot of $\log(\Delta\sigma)$ versus $\log(I_0)$, shown in Figure 6.2.2 c), is 0.89, and the non ideality factor *m*, from the plot of $\log(\Delta\sigma)$ versus V_{OC}, see Figure 6.2.2 b), is 1.95. The product of these non-ideality factors is 1.73, which is identical to that determined from the plot of V_{OC} versus $\log(I_0)$, as in Figure 6.2.2 d). The relevance of this will become clear in section 6.2.3.

6.2.2 Estimation of the sensitivity factor.

In chapter 5, the sensitivity factor, *S*, was calculated by considering the reflections from the various layers making up a DSC depending on the conductivity in an active layer. But is can also be estimated experimentally by taking the ratio;

$$S = \frac{\Delta P_r / P_r}{\Delta \sigma}$$

6.2.5

Where $\Delta P_r / P_r$ is measured by microwave reflectivity, and $\Delta\sigma$ is measured across the gap cell described in the previous section. The sensitivity factor thus obtained is compared to the modelled value in Figure 6.2.3. The agreement is reasonable, in particular since the absolute values of the conductivity are not known due to the uncertainty in the gap thickness, and the modelling assumed an open-ended waveguide, which was not strictly the case. In fact, this experiment helps to illustrate just how un-terminated the waveguide actually is. If the modelling is performed with the same parameters, and assuming a terminated waveguide, the value of the sensitivity factor is smaller by several orders of magnitude.

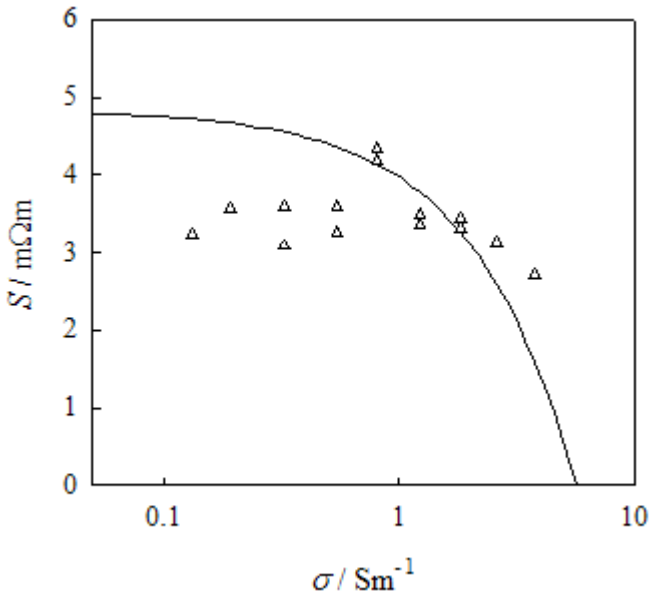

Figure 6.2.3: Sensitivity factor modelled based on the Fresnel reflection coefficients for a layer of thickness 13 μm and relative refractive index 30 in an open ended waveguide (solid line) and sensitivity factor estimated as the ratio of $\Delta P_r / P_r$ and σ (open triangles).

This model is sensitive to factors such as the value of the refractive index of the TiO_2, and the presence of other layers. However in all cases, it was found to be relatively constant for lower conductivities, decreasing as the conductivity reaches ~ $1Sm^{-1}$, which is confirmed by the estimation based on the microwave and gap electrode measurements. This qualitative agreement was considered sufficient, and due to the many unknown parameters and the simplicity of the model which does not truly represent the geometry of the measurement, it was not deemed useful to adjust the parameters to obtain the best possible fit.

6.2.3 How do the various non-idealities relate?

Dye sensitised solar cells are a widely modelled and characterised system. It was shown in Chapter 2 that provided the position of the conduction band is fixed, and that back reaction is pseudo 1st order in electron concentration and occurs solely via the conduction band, the photovoltage should depend on the light intensity according to;

$$qU_{photo} = k_B T \times \ln \frac{\eta_{inj}\eta_{col}\tau_0 (1 - \exp(-\alpha d))I_0}{n_C^0 d}.$$

6.2.6

Although measurements of the photovoltage and light intensity are trivial, it is widely recognised that DSCs are seldom found to behave according to equation 6.2.6, which predicts plots of photovoltage versus the natural logarithm of the light intensity having a slope of k_BT, which corresponds to an increase of 59 mV per decade of light intensity at 300 K. Instead the slopes tend to have higher values, which is *mathematically* consistent with the inclusion of an empirical ideality factor, m, in the Boltzmann distribution function, although this is not necessarily physical:

$$n_c = N_c \exp - \left(\frac{E_c - {}_n E_F}{m k_B T} \right).$$

6.2.7

Equation 6.2.6 essentially derives from the Boltzmann distribution function under the assumption that the free electron concentration is linearly related to the light intensity by equation 6.2.1.

From the derivation of equation 6.2.6, it is clear that a better understanding of the relationship between the free electron concentration and the light intensity, and the quasi Fermi level position, would help to elucidate the origin of the non-ideality observed between the photovoltage and the light intensity. Although the *total* electron concentration in the TiO_2 of DSCs can be measured by means of charge extraction or infrared transmittance, the free electron concentration has remained an unmeasured parameter.

Conductivity offers a means to estimate n_c. It can either be measured as the conductance across TiO_2 forming a bridge between two electrodes, or by microwave reflectivity. As noted in the preceding sections, neither method found the conductivity to be linearly proportional to I_0. Furthermore, in both approaches, the dependence of the conductivity on V_{OC} also deviates from ideality (see Figure 5.5.6 and Figure 6.2.2). The focus thus turns to finding the link between these non-ideal behaviours and the well-documented non-ideality in V_{OC} versus I_0. First of all, equation 6.2.6 will be re-derived with two proposed non-ideality factors, and later, this new derivation will be put to the test thanks to the estimations of n_c which have been made possible by this work.

Fundamentally, the photovoltage of any solar cell is the potential difference between the two contacts. Provided there is no over-potential at the counter electrode, and no potential drop across the TiO_2|FTO interface, this amounts to the difference between the redox Fermi level at the anode and the quasi Fermi level at the cathode:

$$qU_{photo} = {}_nE_F - E_{F,redox} = \left(E_C - E_{F,redox}\right) - \left(E_C - {}_nE_F\right).$$

6.2.8

Similarly to equation 6.2.7, the dark electron concentration can be written;

$$n_C^0 = N_C \exp - \left(\frac{E_C - E_{F,redox}}{mk_BT}\right).$$

6.2.9

Together, equations 6.2.7, 2.5.5 and 2.5.6 lead to:

$$qU_{photo} = mk_BT \times \ln\frac{n_C}{n_C^0}.$$

6.2.10

Since a non-linear behaviour was also observed in n_c versus I_0, a further non-ideality factor, a, was included in equation 6.2.1, such that;

$$n_c = \frac{\eta_{inj}\eta_{col} {I_0}^a \tau_0 \left(1 - \exp(-\alpha d)\right)}{d}.$$

6.2.11

Although experimentally one finds a power dependence of n_c on I_0, it is clear that this is not physical in itself. Instead there must be another parameter in the equation, for instance the electron lifetime or the injection efficiency, which is also dependant on the light intensity. It should be noted that the concept of lifetime is only applicable for the case of 1st order reactions. If the lifetime is found to change, this signifies that the reaction order is not one, and therefore the lifetime is undefined. Combining equations 2.5.7 and 6.2.11, one gets;

$$qU_{photo} = mak_B T \times \ln\left(I_0\right) + C,$$

6.2.12

where C is a constant.

These proposed non-ideality factors can be tested by comparing "m" from plots of n_c versus V_{OC}, "a" from plots of n_c versus I_0, and the value "ma" from plots of V_{OC} versus I_0 for a variety of cells with different non-ideality factors. It is clear from section 6.2.1 that the most appropriate way to estimate n_c would be by measuring the conductivity across a gap rather than by microwave reflectivity, due to the complication of the sensitivity factor in the latter method. However, the former method was only developed and carried out in retrospect, and time limitations did not allow it to be applied to all the different cells made for this study. Slopes were therefore obtained by fitting the curved data such as that in Figure 5.5.6, and since the curvature in plots b) and c) have the same physical origin, and the ideality in one is larger as a consequence, while the other is smaller, the effects cancel when taking the product. Furthermore the exact agreement between the product "m" times "a" and "ma" from Figure 6.2.2 – in which there is no curvature - which is noted at the end of section 6.2.1, lends weight to this argument.

Figure 6.2.4 displays the results of the study presented above on cells made with six different electrolyte compositions. The change in reflected microwave power, which is related to the free electron concentration, and the photovoltage were measured as a

function of light intensity according to the optimised set up described in the previous chapter. From the slopes of fits such as those seen in Figure 5.5.6 (b) and (c), factors "*a*" and "*m*" were determined. Finally the product of these was compared to that measured from plots of photovoltage versus light intensity, such as Figure 5.5.6 (d). A line of $y = x$ has been added to the plot to indicate what would be a perfect match between the non-ideality factor from V_{OC} versus I_0 and the product of *a* and *m*.

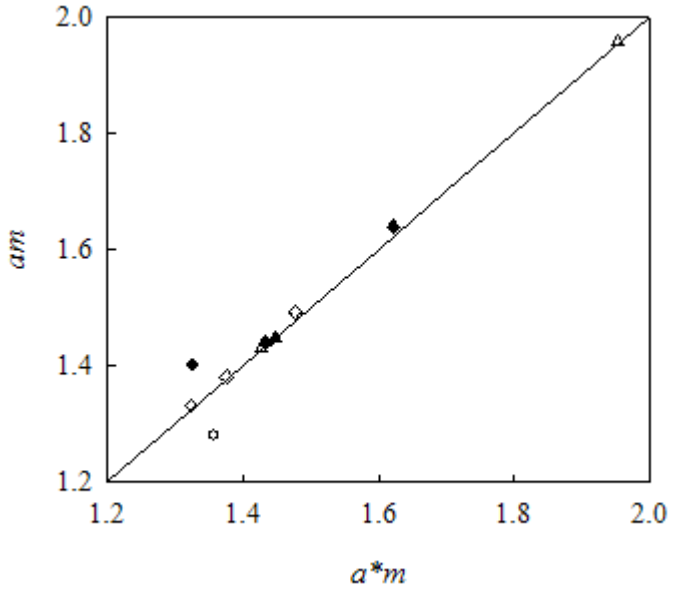

Figure 6.2.4: Non-ideality factor obtained from plots of V_{OC} versus I_0 plotted against the product of the non-ideality factors from plots of $\Delta P_r / P_r$ versus I_0, *a*, and $\Delta P_r / P_r$ versus V_{OC}, *m*. The various symbols correspond to different electrolyte compositions.

These results suggest that there are indeed two sources of non-ideality in DSCs, although their physical origins remain unconfirmed. In order to attempt to elucidate this, consideration must be given to the assumptions listed at the end of the previous chapter. By comparing the assumptions on which the expectations of plots such as those in Figure 5.5.6 (b), (c) and (d), it can be postulated that:

- The non ideality in the relationship between n_c and, *m*, is either related to a movement of the relative position of the conduction band, or to non-ideal Boltzmann statistics.
- The non ideal relationship between the free electron concentration and the light intensity, *a*, is due to the back reaction of electrons not occurring solely by 1st order kinetics via the conduction band, or that the rate of electron injection is light intensity dependant.

- It is also possible that the link between n_c and σ is affected by a non-constant mobility, whose effect would be to increase one non-ideality factor, while decreasing the other – since a is the slope of σ versus I_0, while m is inversely proportional to the slope of σ versus V_{OC} – this non-ideality would therefore not appear in plots of V_{OC} versus I_0. To truly investigate this possibility would involve an independent measurement of the free electron mobility, which is outside the scope of this work.

An intriguing secondary observation from Figure 6.2.4 is that the value of the ideality factor "*ma*" does not appear to correlate strongly with the electrolyte composition. Indeed there is, in many cases, more variation between cells of the same electrolyte composition than between the different electrolytes. However, it was observed that when grouped on the basis of the day on which the cells were prepared, as in Figure 6.2.5, there is a stronger correlation. This suggests that the origin of the non-ideality is more likely to be due to accidental effects, perhaps in the make up of the electrolyte. Un-controlled parameters, such as the relative humidity or the duration of a particular step in the cell fabrication, could introduce accidental additives into the electrolyte, which may alter the surface chemistry in the device.

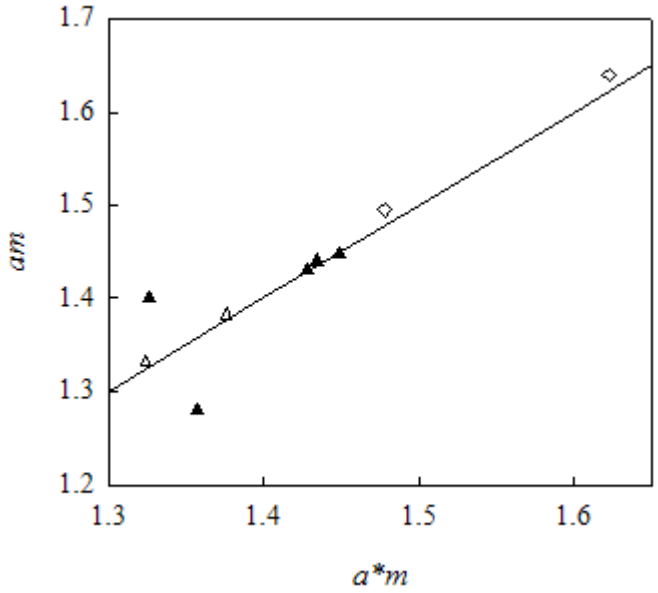

Figure 6.2.5: Non-ideality factor obtained from plots of V_{OC} versus I_0 plotted against the product of the non-ideality factors from plots of $\Delta P_r / P_r$ versus I_0, a, and $\Delta P_r / P_r$ versus V_{OC}, m. The various symbols correspond to cells made on the same day. Note there are fewer data points than in Figure 6.2.4 because only data for cells when at least two cells were prepared on the same day is presented.

6.2.4 Non-ideality between the photovoltage and the free electron concentration.

Assuming that Boltzmann statistics are fundamental to electrons, the most likely explanation for the non-ideality observed in plots of $\Delta P_r / P_r$ versus V_{OC} is that the position of the conduction band relative to the redox Fermi level of the electrolyte changes as the light intensity, and hence the photovoltage of the cell, increases. This hypothesis was quantified by assuming the movement of the conduction band is of the form;

$$E_C - E_{F,redox} = bV_{OC} + c \,,$$

6.2.13

Then, by fitting plots of $ln(n_c)$ versus V_{OC}, the values of b and c can easily be found from the slope and intercept;

$$b = 1 - slope \times k_B T$$
$$c = \left(\ln\left(N_c\right) - \text{int}\, ercept\right) k_B T \,.$$

6.2.14

Figure 6.2.6 summarises the relative conduction band shifts calculated in this way for the same cells which feature in Figure 5.3.2. An encouraging observation is that the relative overall conduction band position of each cell, and therefore electrolyte type, agrees well with the data shown in Figure 5.3.2, namely that the conduction band position, from lowest to highest, is determined by the electrolyte composition:

- Electrolyte H1: 0.5M LiI 0.05M I_2
- Electrolyte H3: 0.1M LiI 0.01M I_2
- Electrolyte H2: 0.5M LiI 0.05M I_2 0.5M TBP
- Electrolyte H4: 0.1M LiI 0.01M I_2 0.5M TBP

However, the absolute magnitude of the conduction band position relative to the redox Fermi level depends on assumptions of the density of conduction band states, N_c, and the sensitivity factor and electron mobility used to calculate n_c from $\Delta P_r / P_r$. Nonetheless, the way in which the conduction band moves, b, does not depend on numerical assumptions, and as such, can be taken as a serious estimate of the extent of band edge unpinning in DSCs under operation. It should also be noted that the band edge shift calculated from microwave reflectivity data and conductivity measured across a gap for cells prepared with the same electrolyte (see Figure 6.2.6 solid line and empty triangles) are in good agreement. This suggests that the slight curvature in the microwave data, which arises from the non-constant sensitivity factor, S, does not significantly alter the slope which is used to estimate the conduction band shift.

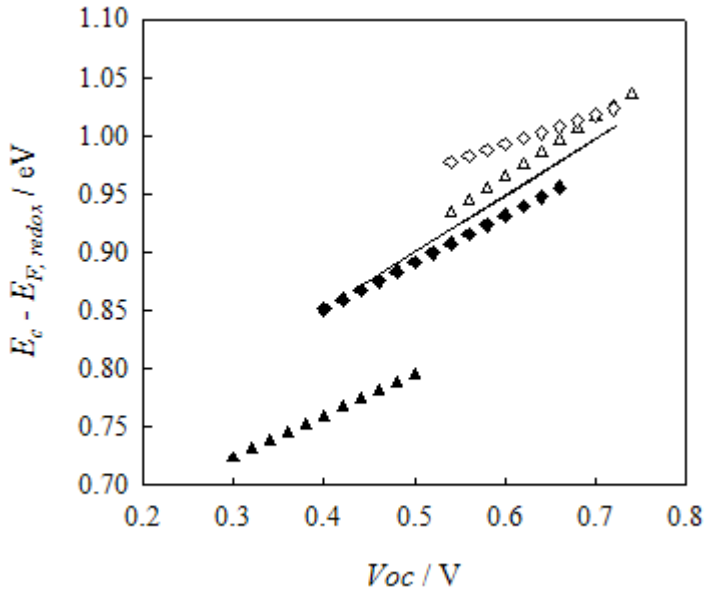

Figure 6.2.6: calculated conduction band shift based on plots such as Figure 6.2.2 for a cell made with electrolyte H2 (solid line) and from Figure 5.5.6 for cells made with electrolyte H1 (filled triangles), H2 (empty triangles), H3 (filled diamonds) and H4 (empty diamonds).

Having ascertained that the non-ideality in the relationship between the free electron concentration and the photovoltage – and consequentially that in the relationship between the photovoltage and the light intensity – is consistent with an upward shift of the conduction band relative to the redox level, our attention turns to possible explanations for this.

These findings are in good agreement with a recent publication by O'Regan and Durrant in which the activation energy for electron transport or recombination – which is thought to be dependent principally on the activation energy for de-trapping – was measured as a function of V_{OC}.[74] For an almost ideal cell, the slope of activation energy versus photovoltage was close to -1, as expected. However for non-ideal cells, the slope deviated from -1 as the cells became less ideal. This indicates that as the photovoltage increases, the activation energy does not decrease as much as it should if the conduction band were not moving up simultaneously. However, when using this technique, care must be taken in whether the calculation of the Arrhenius activation energy is carried out at constant V_{OC}, or at constant $E_C - {}_nE_F$, as was the case previously[75], since this would be, in effect, a circular argument.

As noted above, the difference in conduction band position between different cells scales qualitatively with electrolyte composition, confirming that the concentrations of ions such as Li^+ and TBP play a role in determining the overall conduction band position. There is, however, some variation in the conduction band shift, estimated as above, for nominally identical cells (data not shown). This suggests that other ions, whose concentration is accidental, and therefore not controlled, influences the variation in conduction band position under operation. This is in agreement with the finding presented in the previous section, that the ideality factor – which is assumed to be related to the relative movement of the conduction band – does not correlate strongly with the cation concentration or the presence of TBP. However, when the ideality factors are grouped based on the day they were prepared, there is some correlation. As mentioned by O'Regan and Durrant[74], ions such as Li^+ or H^+ are expected to bind to the TiO_2 surface, and cause a shift in conduction band, possibly as a function of potential and/or light intensity. It can be postulated that the un-controlled differences between the conditions when cells were prepared on different days may include factors which could alter the accidental amount of water present in the cell, such as the relative humidity, the temperature at which the cells are introduced in the dye bath, or even the exact duration of each fabrication step.

It is interesting to note that Abayev *et al.*[37] found the conductivity within a range of potentials corresponding to the normal operating conditions of a DSC to vary with a slope close to 59 mV/decade. Since this measurement was carried out in the dark, it may be consistent with the findings by O'Regan and Durrant[74], that in some respects, cells behave more ideally in the dark than under illumination for a given electron density. They found, for example, that the electron back reaction is accelerated by illumination, although they weren't able to distinguish between the light intensity and the position of the Fermi level as the cause for the band edge shift under operation.

6.2.5 Non-ideality between the free electron concentration and the light intensity.

Plots of $\log(\Delta P_r / P_r)$ versus $\log(I_0)$, such as that presented in Figure 5.5.6 c) have non-ideality factors, *a*, of approximately 0.6. Upon inspection the plot of $\log(\Delta\sigma)$ versus $\log(I_0)$, Figure 6.2.2 c), however, it can be seen that the conductivity varies with the light intensity to the power of 0.9, which is much closer to the linear relationship predicted by equation 6.2.1. This is due to the fact that when measured with the microwave reflectivity technique, the curvature brought on by the non-constant sensitivity factor decreases the slope further. Albeit a small deviation from the model, the photo-conductivity does indeed appear to increase non-linearly with the light intensity. Equation 6.2.1, which is derived in Chapter 2, arises from the balance of fluxes in the cell under open circuit conditions. Namely that the rate of electron injection into the TiO_2 conduction band by the dye must equal the rate of back reaction of conduction band electrons with the I_3^- in the electrolyte. Hence consideration must be given to determining which process, of electron injection or back reaction, is the more likely to be changing as the light intensity, or the photovoltage, increases.

Koops *et al.*[16] have recently shown that the injection efficiency decreases strongly as the conduction band of the TiO_2 increases, as a result of electrolyte composition, in agreement with our infrared and microwave experiments – see Figure 5.3.2 and Figure 6.2.6, respectively. They also found there to be a slight decrease of η_{inj} under applied potential, particularly as the potential reaches the open circuit voltage under one sun illumination. This suggests that if the conduction band shifts to more negative potentials under operation, a gradual decrease in the injection efficiency is conceivable, perhaps as injection occurs into the exponential distribution of inter-bandgap states – which are possibly surface states.[23] By comparing the trends in the published[16] data for decay half life, injection efficiency and conduction band shift, it was calculated that a 100 mV negative shift in the conduction band leads to a decrease in injection efficiency of approximately 0.073. Given that we estimate the conduction band shift to be of the order of 100 mV across the region of operation in this study, this corresponds to a decrease in injection efficiency of approximately

10%. Taking the example of the cell whose conductivity was measured across a gap electrode, since it does not suffer the extra complication of the non-constant sensitivity factor, over the range under study, the maximum conductivity was a factor of two smaller than would be expected if the relationship were linear. This "back of the envelope" calculation does not allow a changing injection efficiency due to band edge shifting to be firmly ruled in or out, since the measurements were carried out in different laboratories. However it implies that it is at least a plausible explanation, and a joint study of injection efficiency and conductivity over the operating range of a DSC could lead to much more definitive conclusions.

In a recent publication, Bisquert *et al.*,[24] credit back reaction of electrons via surface states for the non-constant free electron lifetime. The model uses Marcus theory to account for electron transfer occurring from the exponential distribution of occupied surface energy levels into a distribution of oxidised states in the electrolyte, with reorganisation energy λ. This leads the recombination resistance to decrease for two reasons as the quasi Fermi level moves upwards; an increase in the density of available electrons occupying surface states, and an increase in the charge transfer probability, provided $_nE_F - E_{F,redox}$ does not surpass the reorganisation energy. In this publication, the free electron lifetime was measured by impedance spectroscopy in the dark. If we are trying to draw conclusions about the dependence of the free electron concentration upon the light intensity, it would be interesting to have access to a similar experiment in which the bias was applied by illumination rather than potential. O'Regan and Durrant[74] have found that the recombination flux at a given electron density in the dark is a factor of two lower than under illumination. This effect may well combine with Biquert's observations, so that the recombination resistance decreases faster still with the quasi Fermi level under illumination.

Hence both effects which could account for the non-ideal dependence of free electron concentration on light intensity can be explained if electron transfer is allowed to take place not only via the conduction band of the TiO_2 but also via an exponential distribution of intra-bandgap states. Figure 6.2.7 illustrates these two processes, distinction between which would require detailed modelling and independent determination of parameters such as the reorganisation energy of the

oxidised species. The one qualitative means which may allow to separate these two effects could be that the first – a changing lifetime due to back reaction via surface states – could happen whether or not the conduction band shifts, whereas the second – a variable injection efficiency due to direct injection into empty intra-bandgap states – will only occur in the case of conduction band edge unpinning. It would be interesting to study cells prepared with ionic liquid-based electrolytes, since yet-unpublished work in our laboratory has found that they tend to behave more ideally, and may therefore allow a distinction to be made between these processes. If, for instance, the non-ideality factor, m, was lower than for an equivalent solvent-based cell, whereas a remained unchanged, one could conclude that back reaction via surface states was the more probable. If, on the other hand, both non-idealities were similarly reduced, it would imply that they both shared the same physical origin, namely a conduction band shift, indicating that η_{inj} would be the more likely cause for the non-ideal relationship between the free electron concentration and the light intensity.

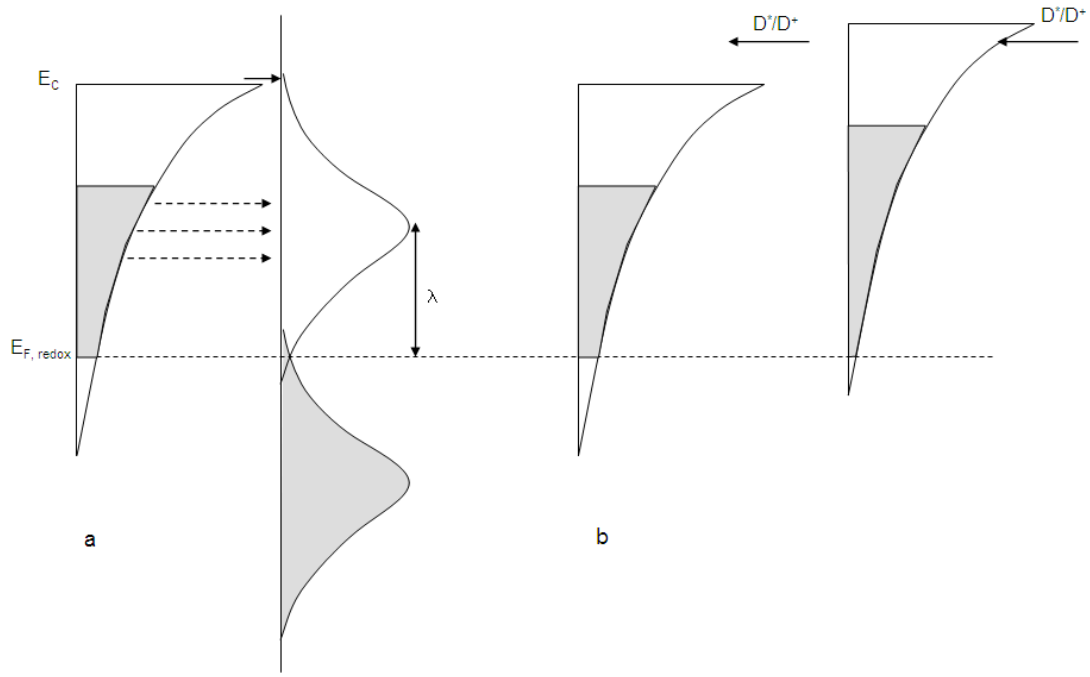

Figure 6.2.7: a) Illustration of back reaction pathways of photo-injected electrons in the TiO_2 with the oxidised species in the electrolyte. The solid arrow indicates back reaction occurring via the conduction band – which is often assumed to be the only pathway – and the dashed arrow indicates electron transfer via surface states, as introduced by Bisquert [24] *et al.*. b) Illustration of the electron injection from the HOMO level of the dye to the TiO_2, in the case where the HOMO level is above the conduction band (left), and once the conduction band has shifted above the HOMO and injection is possible into the intra-bandgap states (right).

No matter which is the physical origin, if we find the free electron concentration to be related to the light intensity raised to the power of *a*, the implication is that in the steady state;

$$\frac{dn_c}{dt} = GI_0 - k_{rec} n_c^{1/a} = 0$$

6.2.15

This signifies that the reaction order, often assumed to be one, is in fact $1/a$. Provided that the electron mobility is constant under operation, the variation of the free electron concentration can be accurately determined by conductivity measurements. The conclusion that the reaction order is not unity will have wide-reaching implications in many areas of DSC characterisation and modelling.

6.3 *Effect of electrolyte composition on the free electron concentration.*

6.3.1 Effect of tert-Butyl Pyridine.

It is well known that the addition of TBP to the electrolyte of DSC improves the cell photovoltage. It is generally accepted that this is because the TBP raises the conduction band position, so that a smaller electron density can lead to a higher photovoltage. Several researchers have suggested[76-77] that the raised conduction band did not fully account for the increased photovoltage at a given light intensity, and that a higher conduction band electron density accounts for the extra photovoltage. In Figure 6.3.1, the free electron concentration, measured by microwave reflectivity, and the trapped electron concentration, obtained from infrared transmission spectroscopy, are shown as a function of photovoltage for cells with basic electrolyte composition 0.5M LiI, 0.05M I_2 in 3-methoxypropionitrile – filled symbols, and with the addition of 0.5M TBP – empty symbols. In both cases, n_t corresponds to the diamonds, while n_c corresponds to the triangles . As expected, the cell with TBP has a higher photovoltage at a given trapped electron density. This is consistent with an upward shift in the conduction band of about 220 meV. It is further noted that there is a slight difference in the β value derived from the slopes; 0.293 for the cell with TBP, and 0.245 for the cell without. This would not be expected if the trap distribution were exponential, and its position were not changing

under operating conditions. Furthermore, Figure 6.3.1 displays the free electron concentration as a function of photovoltage. Broadly speaking, the same trend is observed as for the trapped electron concentration, i.e. at the same photovoltage, the free electron concentration is lower in the cell with TBP.

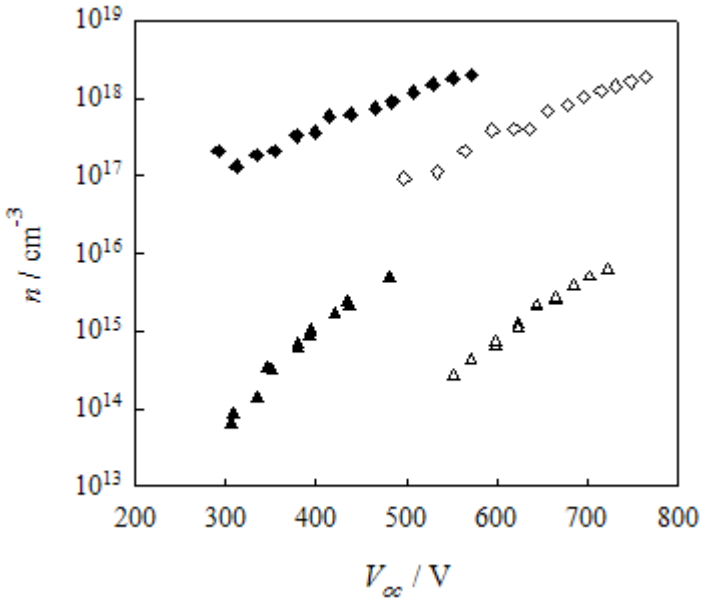

Figure 6.3.1: Trapped (diamonds) and free (triangles) electron densities as a function of photovoltage for cell E23 – without TBP – (filled symbols) and cell E32 – with TBP – (empty symbols).

The same data is plotted against the light intensity at which the microwave measurements were performed, in Figure 6.3.2. The trapped electron density ought to be unchanged by the presence of TBP, unless the electron injection efficiency were changed by the decrease in the relative positions of the HOMO and conduction band, in which case the cell without TBP would be expected to have a higher electron concentration. Instead, the trapped electron concentration in the cell with TBP has been found to be slightly higher. There is a more marked difference between the free electron densities, which was predicted by both Schlichthörl *et al.*[77] and Boschloo *et al.*[76], as a result of observations that the electron lifetime is longer in the presence of TBP, which, in turn, is attributed to a blocking effect. This observation can also explain the slightly higher trapped electron concentration in the presence of TBP, which will also be affected by the longer lifetime.

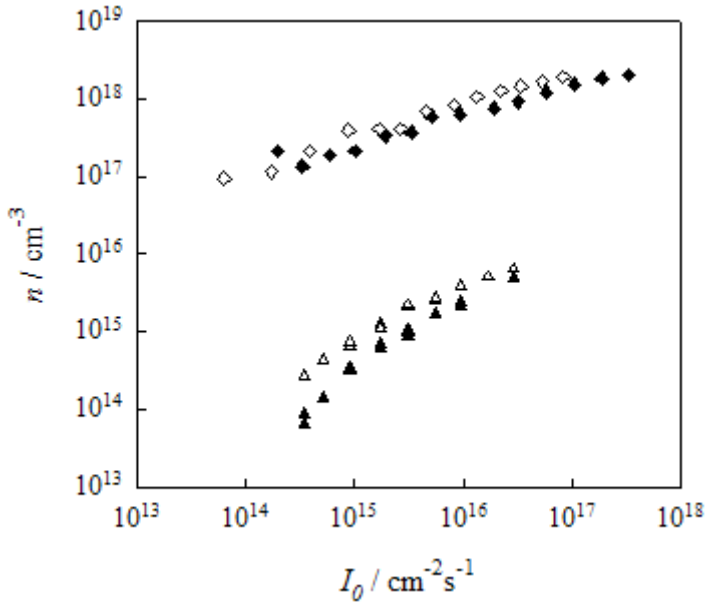

Figure 6.3.2: Electron densities as a function of light intensity. Trapped electron density, n_t (diamonds) and conduction band electron density, n_c (triangles) for cell E23 – without TBP – (filled symbols) and cell E32 – with TBP – (empty symbols).

6.3.2 Steps towards determining the trapping/de-trapping term in the quasi static approximation.

Combined knowledge of the free and trapped electron densities such as the data presented in Figure 6.3.1 may be used to derive an important quantity in the multiple trapping model. If n_t and n_c are taken to be exponential, the derivatives are:

$$\frac{dn_T}{dV} = \frac{\beta n_t}{k_B T}$$

$$\frac{dn_c}{dV} = \frac{n_c}{mk_B T}$$

6.3.1

Which leads to

$$\frac{dn_t}{dn_c} = \beta m \times \frac{n_t}{n_c}$$

6.3.2

According to the quasi-static approximation,

$$\frac{D_n}{D_0} = \frac{1}{1 + \frac{dn_t}{dn_c}}$$

6.3.3

$$\tau_0 = \frac{\tau_n}{1 + \frac{dn_t}{dn_c}}$$

6.3.4

It should therefore be possible to estimate the right hand side of equation 6.3.3 from measurements of free and trapped electron densities, and compare it to the ratio of the apparent electron diffusion coefficient measured by IMPS, and the free electron diffusion coefficient calculated based on the mobility.[38] Likewise, based on knowledge of the free and trapped electron densities and the apparent electron lifetime measured by IMVS, the free electron lifetime can be estimated and compared to the value expected based on measurements of the diffusion length.

Cells were prepared in identical pairs, because the window cells required for the microwave measurements could not be used for experiments in which current is drawn, such as IMPS and infrared spectroscopy at short circuit.

As a consequence of the conclusions we have made regarding the shifting of the TiO_2 conduction band under operation, it is necessary to consider with respect to which variable the derivatives in electron densities should be calculated. If the conduction band is indeed shifting, when plotted versus V_{OC}, the trapped electron density will indicate a broader apparent distribution. If plotted versus $E_C - {}_nE_F$, a more accurate description of the trap distribution should be obtained. Figure 6.3.3 illustrates how the trapped electron density varies with $E_C - {}_nE_F$ when it is calculated from V_{OC} assuming both a fixed and a shifting conduction band. To give an indication of the difference in trap distribution, the temperature coefficient, T_c, calculated assuming a shift in conduction band under operation is 524 K, compared to 874 K for the same cell if the conduction band does not move with respect to the electrolyte Fermi level.

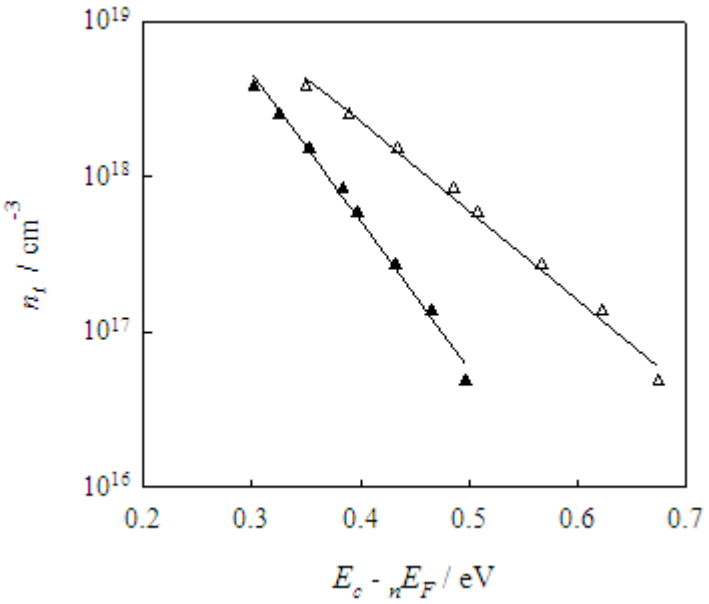

Figure 6.3.3: Trapped electron density plotted as a function of the energetic separation of the quasi Fermi level and the conduction band, assuming a variable (filled symbols), or a constant (empty symbols) position of the conduction band with respect to the redox Fermi level of the electrolyte.

Hence, the derivative featuring in equation 6.3.3 was calculated based upon infrared and microwave data as a function of the cell voltage, and the difference $E_C - {}_nE_F$. IMPS was performed on the corresponding normal cells, and the ratio of the apparent and free electron diffusion coefficient is plotted versus the average internal voltage, if the cell were at short circuit, and the corresponding $E_C - {}_nE_F$. D_0 was taken to be 0.5 cm^{2}s^{-1}, consistent with μ = 20 cm^{2}V^{-1}s^{-1}.

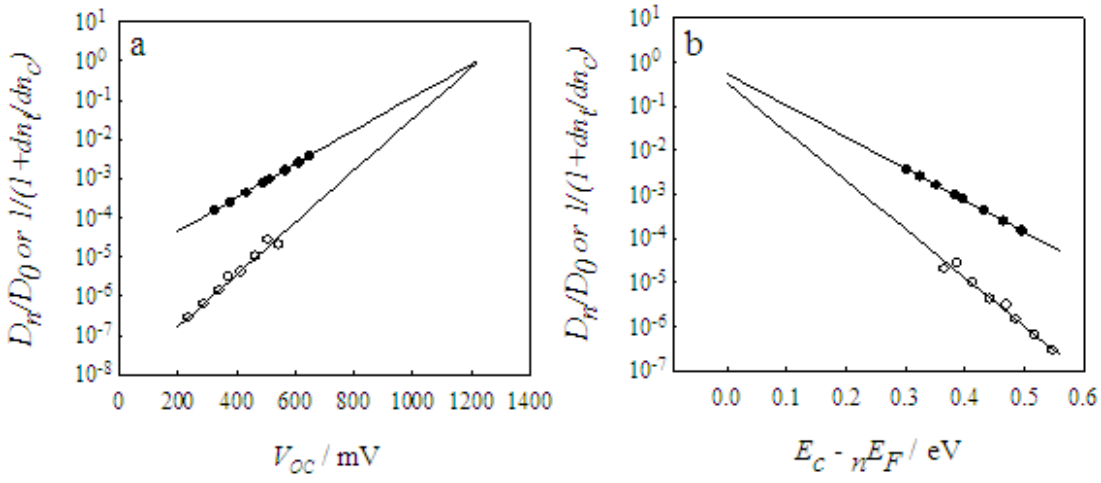

Figure 6.3.4: Left (empty symbols), and right (filled symbols) hand sides of equation 6.3.3 plotted as a function of V_{OC} (a) and $E_C - {}_nE_F$ (b).

It is clear from Figure 6.3.4 that there is a large discrepancy between the estimates of each side of equation 6.3.3. Curiously, there is some sign of consistency in these results, in that when extrapolated to the case where the quasi Fermi level reaches the conduction band, both fits agree that D_n is equal to D_0 – as expected. It is not clear at present whether this is coincidental, or if it is a sign that with some modification of the model, an agreement can be reached.

A similar analysis was carried out on τ_n obtained from IMVS. This time, it was used to estimate τ_0 based on equation 6.3.4, and compare this to the value estimated from the ratio of the square of the diffusion length (calculated from IMVS and IMPS having corrected for the relative position of the equivalent quasi Fermi level) and the free electron diffusion coefficient taken to be 0.5 cm^2s^{-1}. Similarly to Figure 6.3.4, Figure 6.3.5 shows that there is a disagreement of approximately two orders of magnitude between the two estimates.

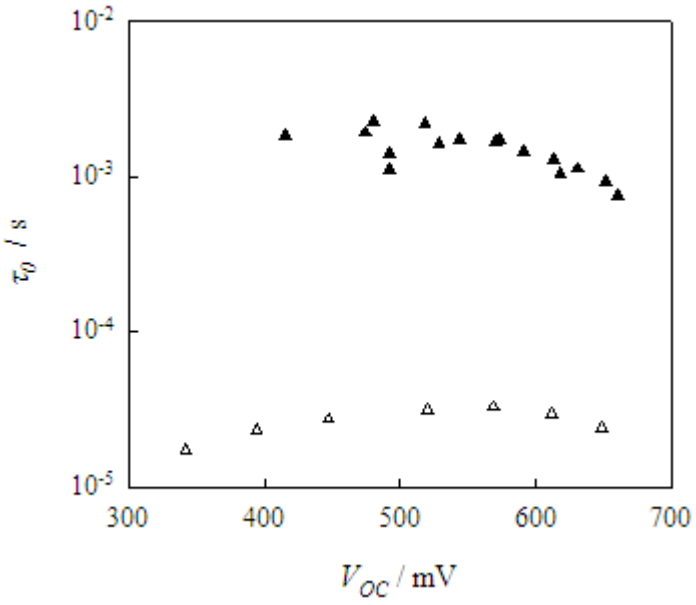

Figure 6.3.5: Estimate of τ_0 from the diffusion length (empty symbols), and from equation 6.3.4 (filled symbols).

It is important at this point to consider all the assumptions on which this model is based. On the one hand, those involved in the estimation of dn_t/dn_c, and on the other in the definition of the *apparent* electron diffusion coefficient and lifetime.

Firstly, it should be noted that equation 6.3.2 is valid only if n_c and n_t are exponential functions of potential. This assumption seems justified in the relatively small range of data obtained, although the slight curvature in the microwave reflectance data is obviously a concern, and may have had an impact on the result. For this reason, data for the lower range of the plots such as in Figure 5.5.6 b) was used, before the onset of the curvature, and the same result was obtained. Furthermore, this analysis requires that not only the slope, but also the absolute values of all the parameters involved are accurately determined. The trapped electron density and the apparent electron diffusion coefficient and lifetime are all well defined experimental parameters, and so shouldn't introduce a large error in the calculation. Measurement of the free electron concentration, on the other hand, is very new, and is therefore subject to a larger uncertainty, not least because there are no previous measurements with which to make comparisons. As discussed in the preceding chapter, there is a large uncertainty in the value taken for the electron mobility, due to the wide range of literature values. However, since the same mobility value is used to calculate n_c from the microwave reflectance, and also to calculate D_0, this does not introduce any inconsistencies in this particular calculation provided the Stokes-Einstein relation is valid. Furthermore it was not possible to correct for the sensitivity factor completely, as discussed in section 6.2.2, so a value of 0.35 Ωcm was used.

Our attention then turns to the underlying assumptions of equations 6.3.3 and 6.3.4. By applying the quasi static approximation to the continuity equations for free and trapped electrons, it can be shown that;[20]

$$\left(1+\frac{\partial n_t}{\partial n_c}\right)\frac{\partial n_c}{\partial t}=\frac{\partial J}{\partial x}$$

6.3.5

where J is the particle flux. Then, by comparing the expression in this equation with Fick's 1st and 2nd laws of diffusion, the apparent electron diffusion coefficient as in equation 6.3.3 is defined assuming back reaction is 1st order in electron concentration. These last two assumptions may not be completely justified, as D_n was measured at short circuit, and shifted to an equivalent V_{OC}. A combined study with laser transients to obtain D_n and τ_n under open circuit conditions would be a good way to ascertain whether this is a contributing factor to the disagreement observed in Figure 6.3.4.. It has also been shown from the photoconductivity measured by both

microwave reflectivity and across a gap between two electrodes that n_c does not scale linearly with light intensity, implying a reaction order which is not one.

One must also take into consideration the differences in the measurements used to obtain D_n, n_c and n_t. D_n and τ_n were measured by dynamic techniques, whereas measurements of n_c and n_t were carried out at steady state. There has already been evidence of disagreement between measurements of L_n by dynamic and steady state techniques.[17, 29]

Although this is put forward as an interesting application of the combined knowledge of n_t and n_c to determine the apparent electron lifetime or diffusion coefficient, it is difficult to reach firm conclusions at this point. Provided the assumptions listed above are justified, it appears that this work could have implications for the multiple trapping model, which may need to be re-assessed.

6.3.3 Effect of the tri-iodide concentration.

A further series of cells was prepared in which the I_2 concentration was varied, keeping the concentration of LiI constant. This lead to electrolytes with compositions 0.5M LiI, xM I_2 in 3-methoxy propionitrile. The electrolyte names were H1 (x=0.05), J1 (x=0.01) and J2 (x=0.02). Since I_3^- originates from the dissociation of I_2, this leads to electrolytes having tri-iodide concentrations of 0.05 M, 0.02 M and 0.01 M.

Provided the back reaction of conduction band electrons with I_3^- is pseudo first order in electron concentration – meaning that $\left[I_3^-\right]$ is a constant – the electron lifetime is given by;

$$\tau_0 = \frac{1}{k\left[I_3^-\right]}.$$

6.3.6

Since the free electron density is expected to depend on the electron lifetime according to equation 6.2.1, the triiodide concentration is expected to be inversely

proportional to the free electron concentration. In order to test this theory, the free electron concentration of the cell with the lowest I_3^- concentration, J1 – which has the highest electron concentration – is divided by 2 and 5, to predict the free electron concentration of the cells with twice and 5 times more concentrated electrolytes – J2 and H1 – respectively. This is illustrated in Figure 6.3.6. The agreement between J1 and J2 is particularly striking. The reason for H1's free electron concentration to deviate at lower light intensities is likely to be due to back reaction via the substrate. This result is tentatively put forward as an argument that back reaction is indeed pseudo-first order in electron concentration. This makes the injection efficiency the more likely candidate to be varying with light intensity, as was discussed in section 6.2.5.

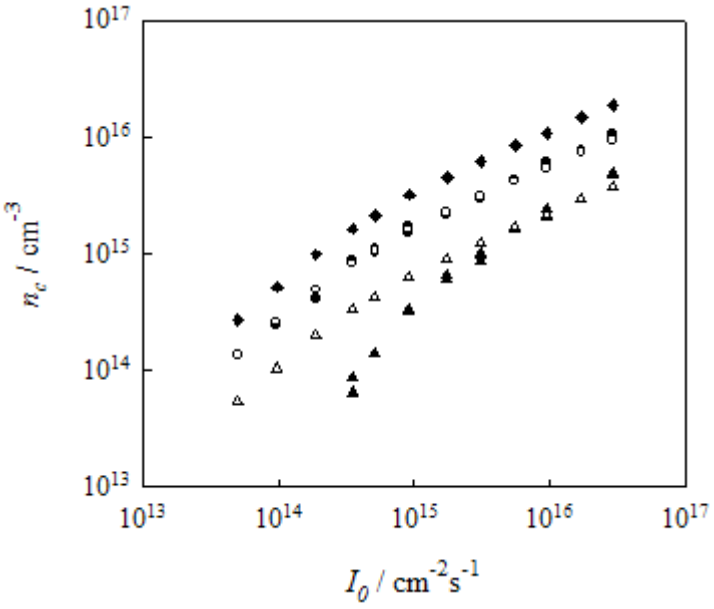

Figure 6.3.6: Filled symbols: free electron concentration for cell made with electrolyte; J1 – diamonds, J2 – circles, H1 – triangles. Empty symbols: free electron concentration of cell made with electrolyte J1 divided by 2 – circles, and divided by 5 – triangles.

6.4 *Frequency resolved microwave conductivity.*

6.4.1 Experimental set up.

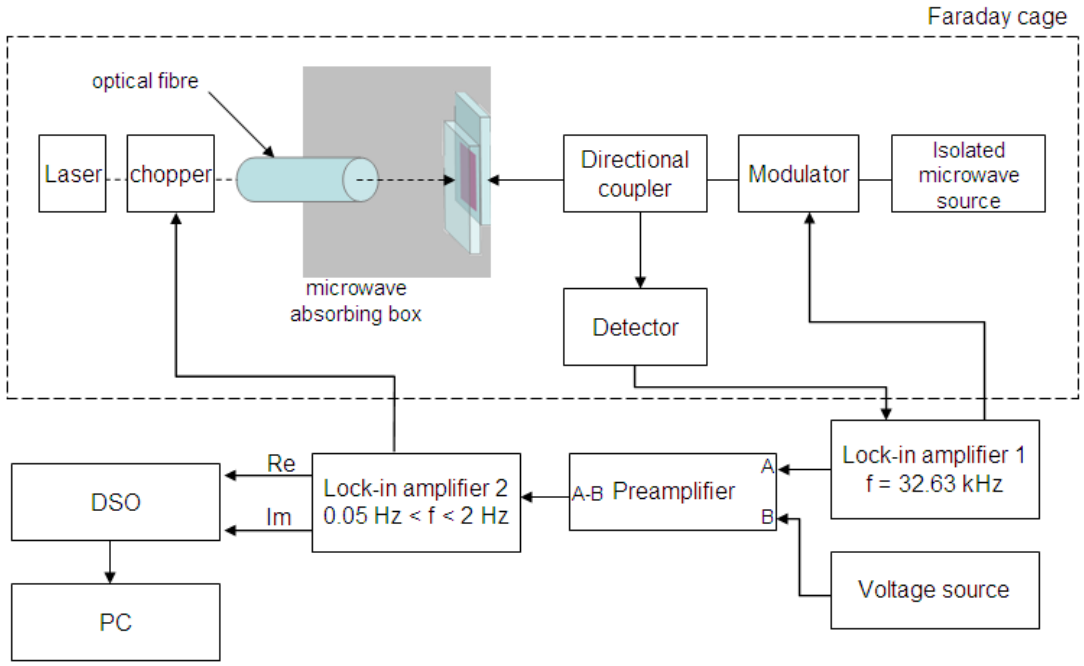

Figure 6.4.1: Experimental set up for frequency-resolved microwave reflectivity measurements.

The setup in Figure 6.4.1 is essentially the same as that described at the end of Chapter 5, with the addition of a means to modulate the incident light intensity. This was achieved by using a second lock in amplifier to drive a chopper, thus modulating the light incident on the cell. The output of the first lock in amplifier, which drives the microwave modulator, is fed into the second. Care was taken so as the time constant of the first lock in amplifier was significantly shorter than the second. The dark microwave reflectivity was subtracted from the output of the first lock in, and was fed into the input of the second, whose reference frequency was driving the chopper. The real and imaginary outputs of this second lock in amplifier were finally averaged on an oscilloscope. These values were then used to construct Nyquist plots – as in Figure 6.4.2 – from which the frequency corresponding to the largest imaginary component was taken to be the relaxation frequency related to electron back reaction.

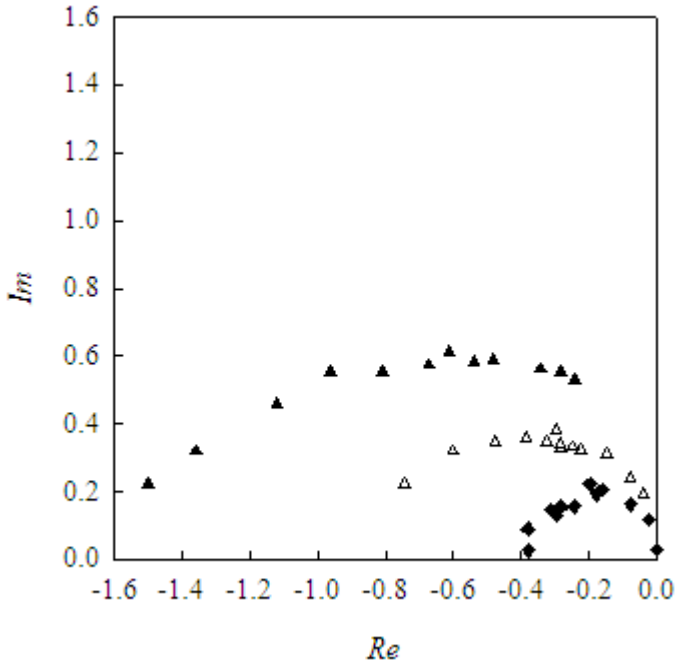

Figure 6.4.2: Nyquist plots obtained at different light intensities. The cell open circuit voltage was 714 mV (filled triangles), 676 mV (empty triangles) and 638 mV (filled diamonds).

6.4.2 Comparison with IMVS.

Since it was only possible to modulate the laser light by 100%, IMVS was performed on an ordinary cell with small and large amplitude modulation, to ensure agreement between the two methods. Figure 6.4.3 shows the agreement between IMVS measured in these ways. There is a slight shift along the voltage axis of ~20 mV, which is likely to be due to the determination of V_{OC} for the large amplitude modulated IMVS. On this graph, the time constant associated with the relaxation of the microwave signal is also shown. It can be seen that the four points which were obtained lie within the range of values measured by IMPS. Since this experiment does not require any absolute value of the free electron concentration to be known, only the time associated with the change in reflectivity, these results can provide encouragement that the microwave reflectivity method is indeed probing the free electrons. However, owing to the experimental difficulty of this measurement, it is not surprising that the trend of the time constant measured by microwave reflectivity does not follow exactly the apparent electron lifetime, but certainly the order of magnitude is correct.

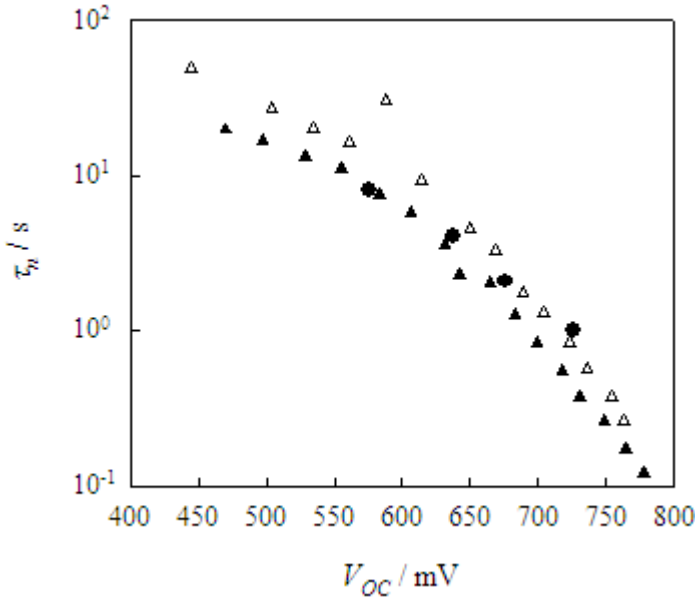

Figure 6.4.3: Apparent electron lifetime measured by small (filled triangles) and large (empty triangles) amplitude IMVS, and frequency-resolved microwave reflectivity (circles).

6.4.3 Possible improvements to the system.

As was mentioned above, the measurement of frequency resolved microwave reflectivity was complicated by experimental limitations, which made measuring lower light intensities impossible, and resulted in rather large uncertainty.

The illumination sources for all intensity modulated experiments in this laboratory are power LEDs, which can be driven with a DC bias and an adjustable sinusoidal modulation. This allows the cell to be modulated at low amplitude, in order to linearise the response. However illumination of the microwave set up is only possible through a fibre optic, since the light has to be brought into the microwave absorbing chamber, therefore the only practical light source is a laser, due to it being focussed. Hence the only means to modulate the incident illumination is by chopping, which results in a modulation depth of 100%. Furthermore sine wave modulation would be preferable to chopped light, as the lock in amplifier is better suited to detecting sine waves. Automating the measurements using, for example, a Solartron frequency response analyser would certainly make the measurements more practical, and may even improve the stability of the measurements.

Although this experiment was carried out simply as a "proof of principle", and the results were limited by the experimental framework available at the time, it has certainly provided more evidence suggesting that microwave reflectivity is successfully probing the free electron density, or at least a quantity proportional to it.

6.5 *Investigation of the free electron concentration at short circuit.*

Having measured the free electron concentration at open circuit, and exposed non-idealities between the free electron concentration and the photovoltage and light intensity, an obvious next step was to attempt the same measurement under short circuit conditions. This would not be trivial, as the etched window in the FTO, necessary for the microwave set up would not allow this. Since the dominant mode in the waveguide is polarised perpendicular to the short side, a discontinuous conductor along this axis would not interfere with microwave propagation. Slits were etched parallel to the long side of the waveguide. The ideal slit width would be narrower than twice the diffusion length, allowing all electrons generated in the areas without FTO to be collected. As the means to produce such an etch was not readily available at the time of this work, an etching pattern was cut out of kapton tape, and slit sizes of around ½ mm were achieved.

The first aim was to show that the strips of conducting FTO did not interfere with the microwave propagation. To this end, pairs of otherwise identical cells with slits (cell S51) and a rectangular window (S52) were made, and the microwave conductivity at open circuit was compared. It can be seen from Figure 6.5.1 that the trend of the variation of free electron concentration with light intensity is similar in both cells, although there is a difference of a factor of approximately two, which may arise from a slight difference in the sensitivity factor. This suggests that the microwaves pass through the strips of conductor reasonably unperturbed.

Secondly the microwave reflectivity was measured when the cell was at short circuit. Unsurprisingly, given the size of the strips, the microwave reflectivity was very similar to that measured at open circuit, as most of the area was in fact not at short circuit. The area of the cell which was un-etched was about 80 mm^2, which was in

good agreement with the short circuit current of the strip cell being *ca.* 80% of the current produced by an identical un-etched cell.

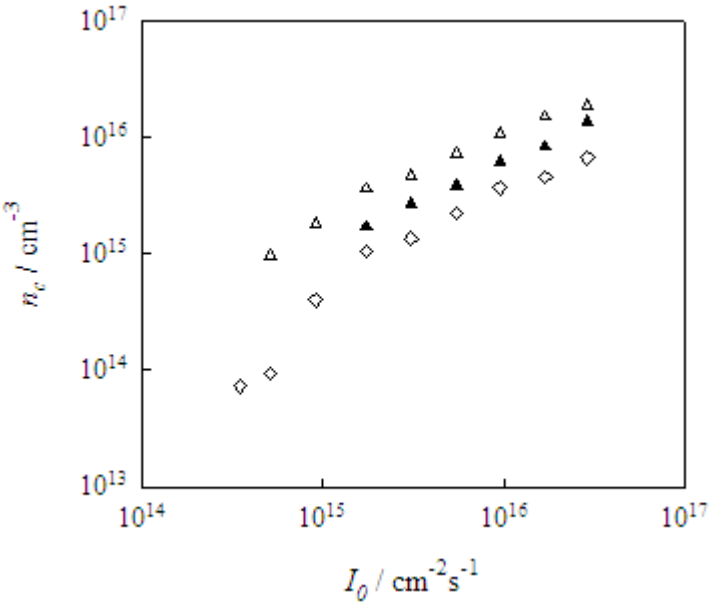

Figure 6.5.1: Free electron concentration as a function of light intensity for a pair of cells with an etched window (empty diamonds) and etched slits (empty triangles) at open circuit. The slit cell was also measured under short circuit conditions (filled triangles).

Planned experiments at NPL will involve scanning a small IR spot across the etched strips, enabling the local quasi Fermi level to be measured. Performed at short circuit with a strip wider than the diffusion length, this will also provide a novel method to obtain the diffusion length.

The prospects for extending this method to measure the free electron concentration under short circuit conditions are good. A finer etching pattern is needed to allow electrons from the etched areas to be extracted. One option could be printed lithography followed by etching with zinc granules and HCl. This may or may not be feasible due to the size of the zinc granules (the use of zinc powder is not possible as it lifts off the surface of FTO on addition of HCl). Another possibility is to use high powered lasers to mechanically score lines in the FTO, or possibly to deposit the FTO through a mask.

Although measurement of the free electron concentration at short circuit was not achieved, the principle was proven, and with suitable developments to the etching

procedure, it should be possible to make a device where the diffusion length exceeds the strip width.

6.6 *Conclusions and outlook.*

In this, and the previous chapter, we have demonstrated the use of two methods to probe the conductivity of porous TiO_2 in a working solar cell; microwave reflectivity, and the measurement of the electrical conductivity across a TiO_2 bridge between two FTO contacts. This has lead to a more detailed understanding of the well-documented non-ideal behaviour of the photovoltage with light intensity, namely that it probably arises as the combination of two effects. Firstly, the free electron concentration is varying with photovoltage in a way which is consistent with a shift in the energetic position of the conduction band relative to the Fermi level in the electrolyte. The second, that the free electron concentration is not linearly dependant on the light intensity, could be a result of either a non-constant free electron lifetime, due to back reaction via surface states, or a non-constant injection efficiency, possibly due to the conduction band moving with respect to the LUMO of the dye, thus changing the driving force for injection. The latter would mean that the supposed shifting conduction band is the physical origin for both non-idealities.

The microwave reflectivity technique was also adapted to provide a proof of principle for two related experiments. Firstly, the incident light was frequency modulated, and a double lock-in setup allowed the measurement of the apparent electron lifetime as a function of photovoltage. The results were compared to measurements obtained by IMVS, and were found to be in reasonable agreement given the experimental imperfections. Secondly, by etching strips in the FTO perpendicular to the dominant microwave mode in the waveguide, it was shown that with more refined etching, it should be possible to measure the free electron concentration under short circuit conditions.

7 Conclusions and outlook.

7.1 *The diffusion length.*

The issue of the most correct manner to obtain the electron diffusion length in DSCs is currently under debate. Kinetic methods, such as the combination of IMVS and IMPS, EIS, or highly time resolves laser-induced photovoltage transients systematically yield larger values than steady state methods such as the comparison of IPCE spectra from front and rear side illumination. Here, we have extended a technique proposed by O'Regan, which allows the determination of the apparent electron diffusion coefficient directly at open circuit from the kinetics of photovoltage rise from a steady state as a response to a short laser pulse. The technique was compared to IMVS and IMPS, and assuming a shift between the quasi Fermi level at open circuit and the average quasi Fermi level at short circuit of ~250 mV, they are in good agreement. It is noted that the assumed shift, although not impossible, is rather large. Since it was, unfortunately, not possible to obtain an independent measurement of the shift for the cells as part of this study, is should be noted that if the real shift were, in fact, smaller, then the predicted L_n from IMVS and IMPS would be smaller than that estimated by the rise time method. No technique is without its drawback, be it experimental (IMPS data is regularly found to exhibit flattened semi-circles) or analytical (accurate fitting of the IPCE spectra becomes impossible when the collection efficiency is high). Perhaps, a combined approach using several methods should be the more sensible way to determine an average diffusion length.

7.2 *Conductivity measurements as a measure of the free electron density.*

The initial aim of this thesis was to measure the free electron concentration using a microwave reflectivity technique. The technique was developed and optimised, although unexpectedly, the variation of the measured change in reflectivity – which was assumed to be proportional to the free electron concentration – did not scale linearly with the light intensity or the photovoltage. It was later realised that when measured across a bridge between two electrodes, the conductivity did vary linearly

with light intensity and photovoltage, indicating that the non-linearity in the microwave measurements were due to the sensitivity factor, *S*, being a function of the conductivity. In principle, this sensitivity factor can be modelled by considering the reflections from the various layers making up a DSC. However, due to the geometry of the experimental apparatus, notably that the sample is not contained in the waveguide, which is neither truly open nor truly terminated, a 3-D model accounting for these complications is needed, and is currently being developed by our collaborators in the Physics Department. A simpler model was used to obtain an estimate of how the sensitivity factor was expected to vary qualitatively, and was in reasonable agreement with an experimental estimate based on the ratio of the change in microwave reflectivity and the conductivity measured on similar cells. The preceding discussion suggests that in the face of the simplicity of the measurement of the conductivity across a bridge, and given the complications ensuing from the microwave method, one might conclude that the microwave reflectivity technique is redundant. However, there may be cases where it is in fact more appropriate, in which case it would be used in conjunction with the gap technique, as a means to calibrate the sensitivity factor. As an example of such a case, measurements of the conductivity at short circuit would be impossible across a gap, whereas preliminary work presented here indicates that this is indeed possible with microwave reflectivity.

7.3 *Non-ideal behaviour in DSCs.*

It is well established in the field of DSCs that the photovoltage is seldom found to vary with light intensity in the manner predicted by the theory presented in chapter 2. An empirical non-ideality factor is routinely added to the Boltzmann distribution function to account for this deviation. Given that the assumptions for this theory lie in the relationship between the free electron density and the light intensity on one hand, and the free electron density and photovoltage on the other hand, measurements of photoconductivity – which is proportional to the free electron density – lends itself well to the study of non-ideality. Provided that the electron mobility can be assumed constant, the conductivity is proportional to the free electron density, and therefore its variations with photovoltage or light intensity have given us insight into the mechanism of non-ideality. It has been concluded that there are in fact two non-idealities, which combine to make up the empirical non-ideality

factor found in the relationship between the photovoltage and the light intensity. The first, which occurs in the relationship between the free electron concentration and the photovoltage is thought to be a result of a movement of the conduction band relative to the redox Fermi level in the electrolyte as the light intensity, and hence the photovoltage of the cell increase. The second, that the free electron density is not proportional to the light intensity, could arise from a non-constant injection efficiency or TiO_2 electron lifetime. It was, however, not possible to distinguish between these as causes for the non-ideality.

8 References

1. Oreskes, N., *Science* **2004,** *306* (5702), 1686-1686.
2. Eisenberg, R.; Nocera, D. G., *Inorganic Chemistry* **2005,** *44* (20), 6799-6801.
3. Kudo, A.; Miseki, Y., *Chemical Society Reviews* **2009,** *38* (1), 253-278.
4. Osterloh, F. E., *Chemistry of Materials* **2008,** *20* (1), 35-54.
5. Wurfel, P., *Physics of Solar Cells*. Wiley: Weinheim, 2005.
6. Nelson, J., *The Physics of Solar Cells*. Imperial College Press: London, 2003.
7. Green, M. A.; Emery, K.; Hishikawa, Y.; Warta, W., *Progress in Photovoltaics* **2009,** *17* (5), 320-326.
8. Scragg, J. J.; Dale, P. J.; Peter, L. M., *Electrochemistry Communications* **2008,** *10* (4), 639-642.
9. Gregg, B. A., *Journal of Physical Chemistry B* **2003,** *107* (20), 4688-4698.
10. Quickenden, T. I.; Bassett, R. L., *Journal of Physical Chemistry* **1981,** *85* (15), 2232-2238.
11. Tennakone, K.; Fernando, C. A. N.; Dewasurendra, M.; Kariapper, M. S., *Journal of Physics D-Applied Physics* **1986,** *19* (9), L191-L194.
12. Oregan, B.; Gratzel, M., *Nature* **1991,** *353* (6346), 737-740.
13. O'Regan, B. C.; Bakker, K.; Kroeze, J.; Smit, H.; Sommeling, P.; Durrant, J. R., *Journal of Physical Chemistry B* **2006,** *110* (34), 17155-17160.
14. Peter, L. M., *Physical Chemistry Chemical Physics* **2007,** *9* (21), 2630-2642.
15. Rowley, J.; Meyer, G. J., *Journal of Physical Chemistry C* **2009,** *113* (43), 18444-18447.
16. Koops, S. E.; O'Regan, B. C.; Barnes, P. R. F.; Durrant, J. R., *Journal of the American Chemical Society* **2009,** *131* (13), 4808-4818.
17. Wang, H. X.; Peter, L. A., *Journal of Physical Chemistry C* **2009,** *113* (42), 18125-18133.
18. Barnes, P. R. F.; Anderson, A. Y.; Koops, S. E.; Durrant, J. R.; O'Regan, B. C., *Journal of Physical Chemistry C* **2009,** *113* (3), 1126-1136.
19. Peter, L. M.; Wijayantha, K. G. U., *Electrochemistry Communications* **1999,** *1* (12), 576-580.
20. Bisquert, J.; Vikhrenko, V. S., *Journal of Physical Chemistry B* **2004,** *108* (7), 2313-2322.
21. Bailes, M.; Cameron, P. J.; Lobato, K.; Peter, L. M., *Journal of Physical Chemistry B* **2005,** *109* (32), 15429-15435.
22. Duffy, N. W.; Peter, L. M.; Rajapakse, R. M. G.; Wijayantha, K. G. U., *Electrochemistry Communications* **2000,** *2* (9), 658-662.
23. Kopidakis, N.; Neale, N. R.; Zhu, K.; van de Lagemaat, J.; Frank, A. J., *Applied Physics Letters* **2005,** *87* (20).
24. Bisquert, J.; Fabregat-Santiago, F.; Mora-Sero, I.; Garcia-Belmonte, G.; Gimenez, S., *Journal of Physical Chemistry C* **2009,** *113* (40), 17278-17290.
25. Sze, S. M., *Physics of Semiconductor Devices*. Wiley: Singapore, 1981.
26. Peter, L. M., *Journal of Physical Chemistry C* **2007,** *111* (18), 6601-6612.
27. Sodergren, S.; Hagfeldt, A.; Olsson, J.; Lindquist, S. E., *Journal of Physical Chemistry* **1994,** *98* (21), 5552-5556.
28. Halme, J.; Boschloo, G.; Hagfeldt, A.; Lund, P., *Journal of Physical Chemistry C* **2008,** *112* (14), 5623-5637.

29. Barnes, P. R. F.; Liu, L. X.; Li, X. E.; Anderson, A. Y.; Kisserwan, H.; Ghaddar, T. H.; Durrant, J. R.; O'Regan, B. C., *Nano Letters* **2009,** *9* (10), 3532-3538.
30. Cameron, P. J.; Peter, L. M.; Hore, S., *Journal of Physical Chemistry B* **2005,** *109* (2), 930-936.
31. Boschloo, G.; Hagfeldt, A., *Journal of Physical Chemistry B* **2005,** *109* (24), 12093-12098.
32. Nguyen, T. T. O.; Peter, L. M.; Wang, H. X., *Journal of Physical Chemistry C* **2009,** *113* (19), 8532-8536.
33. Jennings, J. R.; Ghicov, A.; Peter, L. M.; Schmuki, P.; Walker, A. B., *Journal of the American Chemical Society* **2008,** *130* (40), 13364-13372.
34. Lobato, K.; Peter, L. M.; Wurfel, U., *Journal of Physical Chemistry B* **2006,** *110* (33), 16201-16204.
35. Bisquert, J., *Journal of Physical Chemistry C* **2007,** *111* (46), 17163-17168.
36. Halme, J.; Miettunen, K.; Lund, P., *Journal of Physical Chemistry C* **2008,** *112* (51), 20491-20504.
37. Abayev, I.; Zaban, A.; Fabregat-Santiago, F.; Bisquert, J., *Physica Status Solidi a-Applied Research* **2003,** *196* (1), R4-R6.
38. Forro, L.; Chauvet, O.; Emin, D.; Zuppiroli, L.; Berger, H.; Levy, F., *Journal of Applied Physics* **1994,** *75* (1), 633-635.
39. Hendry, E.; Koeberg, M.; O'Regan, B.; Bonn, M., *Nano Letters* **2006,** *6* (4), 755-759.
40. Turner, G. M.; Beard, M. C.; Schmuttenmaer, C. A., *Journal of Physical Chemistry B* **2002,** *106* (45), 11716-11719.
41. Kroeze, J. E.; Savenije, T. J.; Warman, J. M., *Journal of the American Chemical Society* **2004,** *126* (24), 7608-7618.
42. Hendry, E.; Wang, F.; Shan, J.; Heinz, T. F.; Bonn, M., *Physical Review B* **2004,** *69* (8).
43. Dittrich, T.; Lebedev, E. A.; Weidmann, J., *Physica Status Solidi a-Applied Research* **1998,** *167* (1), R9-R9.
44. Aduda, B. O.; Ravirajan, P.; Choy, K. L.; Nelson, J., *International Journal of Photoenergy* **2004,** *6* (3), 141-147.
45. Petrozza, A.; Groves, C.; Snaith, H. J., *Journal of the American Chemical Society* **2008,** *130* (39), 12912-12920.
46. Ramsa, A.; Jacobs, H.; Brand, F., *Journal of Applied Physics* **1959,** *30* (7), 1054-1060.
47. Deb, S. a. N., BR, *Journal of Applied Physics* **1962,** *33* (4), 1604.
48. Bogomolni, R. A.; Tributsch, H.; Petermann, G.; Klein, M. P., *Journal of Chemical Physics* **1983,** *78* (5), 2578-2584.
49. Kunst, M.; Beck, G.; Tributsch, H., *Journal of the Electrochemical Society* **1984,** *131* (4), 954-956.
50. Kunst, M.; Beck, G., *Journal of Applied Physics* **1986,** *60* (10), 3558-3566.
51. Kunst, M.; Beck, G., *Journal of Applied Physics* **1988,** *63* (4), 1093-1098.
52. Wunsch, F.; Schlichthorl, G.; Tributsch, H., *Journal of Physics D-Applied Physics* **1993,** *26* (11), 2041-2048.
53. Schlichthorl, G.; Peter, L. M., *Journal of the Electrochemical Society* **1995,** *142* (8), 2665-2669.
54. Schlichthorl, G.; Peter, L. M., *Journal of Electroanalytical Chemistry* **1995,** *381* (1-2), 55-61.
55. Schlichthorl, G.; Lewerenz, H. J., *Journal of Electroanalytical Chemistry* **1998,** *443* (1), 9-31.

56. Cass, M. J.; Duffy, N. W.; Kirah, K.; Peter, L. M.; Pennock, S. R.; Ushiroda, S.; Walker, A. B., *Journal of Electroanalytical Chemistry* **2002,** *538*, 191-203.
57. Duffy, N. W.; Kirah, K.; Peter, L. M.; Ushiroda, S., *Zeitschrift Fur Physikalische Chemie-International Journal of Research in Physical Chemistry & Chemical Physics* **2003,** *217* (4), 333-350.
58. Cass, M. J.; Duffy, N. W.; Peter, L. M.; Pennock, S. R.; Ushiroda, S.; Walker, A. B., *Journal of Physical Chemistry B* **2003,** *107* (24), 5857-5863.
59. Cass, M. J.; Duffy, N. W.; Peter, L. M.; Pennock, S. R.; Ushiroda, S.; Walker, A. B., *Journal of Physical Chemistry B* **2003,** *107* (24), 5864-5870.
60. Katoh, R.; Huijser, A.; Hara, K.; Savenije, T. J.; Siebbeles, L. D. A., *Journal of Physical Chemistry C* **2007,** *111* (28), 10741-10746.
61. Dehaas, M. P.; Warman, J. M., *Chemical Physics* **1982,** *73* (1-2), 35-53.
62. Kroeze, J. E.; Savenije, T. J.; Vermeulen, M. J. W.; Warman, J. M., *Journal of Physical Chemistry B* **2003,** *107* (31), 7696-7705.
63. Kroeze, J. E.; Savenije, T. J.; Warman, J. M., *Comptes Rendus Chimie* **2006,** *9* (5-6), 667-675.
64. Beard, M. C.; Turner, G. M.; Schmuttenmaer, C. A., *Journal of Physical Chemistry B* **2002,** *106* (29), 7146-7159.
65. Hecht, E., *Optics*. 4 ed.; Addison Wesley Publishing Company: 2001.
66. Bleaney, B. I.; Bleaney, B., *Electricity and Magnetism*. 3 ed.; Oxford Science Publications: Oxford, 1957; Vol. 1.
67. Horikoshi, S.; Sakai, F.; Kajitani, M.; Abe, M.; Emeline, A. V.; Serpone, N., *Journal of Physical Chemistry C* **2009,** *113* (14), 5649-5657.
68. Dominici, L.; Michelotti, F.; Brown, T. M.; Reale, A.; Di Carlo, A., *Optics Express* **2009,** *17* (12), 10155-10167.
69. Rakhshani, A. E.; Makdisi, Y.; Ramazaniyan, H. A., *Journal of Applied Physics* **1998,** *83* (2), 1049-1057.
70. vonRottkay, K.; Rubin, M., Optical indices of pyrolytic tin-oxide glass. In *Thin Films for Photovoltaic and Related Device Applications*, Ginley, D.; Catalano, A.; Schock, H. W.; Eberspacher, C.; Petersen, T. M.; Wada, T., Eds. 1996; Vol. 426, pp 449-454.
71. Amnerkar, R. H.; Adgaonkar, C. S.; Yawale, S. S.; Yawale, S. P., *Bulletin of Materials Science* **2002,** *25* (5), 431-434.
72. Jain, N.; Brown, B., *Ieee Microwave and Guided Wave Letters* **1997,** *7* (10), 344-346.
73. Agrell, H. G.; Boschloo, G.; Hagfeldt, A., *Journal of Physical Chemistry B* **2004,** *108* (33), 12388-12396.
74. O'Regan, B. C.; Durrant, J. R., *Accounts of Chemical Research* **2009,** *42* (11), 1799-1808.
75. O'Regan, B. C.; Durrant, J. R., *Journal of Physical Chemistry B* **2006,** *110* (17), 8544-8547.
76. Boschloo, G.; Haggman, L.; Hagfeldt, A., *Journal of Physical Chemistry B* **2006,** *110* (26), 13144-13150.
77. Schlichthorl, G.; Huang, S. Y.; Sprague, J.; Frank, A. J., *Journal of Physical Chemistry B* **1997,** *101* (41), 8141-8155.

9 Appendices.

9.1 *Appendix A: glossary of symbols.*

Symbol	Quantity	Unit*
α	Absorption coefficient	cm^{-1}
a	Non-idealitybetween n_c and I_0 (Chaper 6)	
β	Temperature coefficient	
C	Capacitance	F
c	Concentration	Mol L^{-1}
d	Film thickness	μm
D_o	Free electron diffusion coefficient	cm^2s^{-1}
D_n	Apparent electron diffusion coefficient	cm^2s^{-1}
E	Energy	eV
E_c	Conduction band energy	eV
$E_{F,redox}$	Fermi level in the electrolyte	eV
${}_nE_F$	Quasi Fermi level in the TiO_2	eV
ε	Molar extinction coefficient	$Lmol^{-1}cm^{-1}$
ε	Relative permitivity	
ε_0	Permittivity of free space	F cm^{-1}
$f(E)$	Boltzmann distribution function	
FF	Fill factor	
$g(E)$	Density of states function	$cm^{-3}eV^{-1}$
η_{inj}	Injection efficiency	
η_{col}	Collection efficiency	
η_{LH}	Light harvesting efficiency	
I_0	Light intensity	$cm^{-2}s^{-1}$
I_{SC}	Short circuit current	A
j	Imaginary number	
j	Flux	$cm^{-2}s^{-1}$
k_B	Boltzmann constant	eVK^{-1}
k	Reaction rate constant	

L_n	Diffusion length	cm
λ	Wavelength	nm
μ	Mobility	$cm^2V^{-1}s^{-1}$
m	Empirical on-ideality factor in Boltzmann distribution function	
N_c	Density of conduction band states	cm^{-3}
n_c	Density of conduction band electrons	cm^{-3}
n_c^0	Density of conduction band states in the dark	cm^{-3}
N_t	Density of trap states	cm^{-3}
n_t	Density of trapped electrons	cm^{-3}
P_{in}	Incident power	W
P_r	Reflected microwave power	W
q	Elementary charge	C
Q	Charge	C
R	Microwave reflectance	
σ	Conductivity	S/m
S	Microwave sensitivity factor	Ωcm
τ_{trans}	Transport time	s
T	Absolute temperature	K
T_c	Characteristic temperature	K
τ_0	Free electron lifetime	s
τ_n	Apparent electron lifetime	s
V	Voltage	V
V_{OC}	Open circuit voltage	V
υ	Reaction rate	s^{-1}
ω	Frequency	Hz
ξ	IMPS factor	

* unless otherwise stated

9.2 *Appendix B: Parameters used in modelling in Figure 5.3.5.*

Medium	Conductivity S/m	Relative dielectric constant	Thickness
Glass	0	7	1 mm
Air	0	1	
Electrolyte	$8x10^{-2}$	36	12 μm
FTO	10^2	4	200 nm
TiO_2	variable	30	13 μm

9.3 *Appendix C: Non ideality factors in Chapter 6.*

cell	m from $\log\left(\frac{\Delta P_r}{P_r}\right)$ versus V_{OC}	a from $\log\left(\frac{\Delta P_r}{P_r}\right)$ versus $\log(I_0)$	a*m	m from V_{OC} versus $\log(I_0)$
L31	1.878	0.7868	1.47761	1.495
E23	1.563	0.9267	1.448432	1.448
E32	2.046	0.6977	1.427494	1.43
12	1.867	1.0458	1.952509	1.959
L11	1.672	0.9703	1.622342	1.64
E22	1.733	0.8273	1.433711	1.44
52	1.702	0.8678	1.476996	1.493
S52	1.34	1.0265	1.37551	1.382
S51	1.823	0.7262	1.323863	1.332
E21	2.057	0.6447	1.326148	1.4
E41	2.173	0.6244	1.356821	1.28
Cell 5	1.95	0.89	1.73	1.73

9.4 *Appendix D: Additional information on cells in chapters 4, 5 and 6.*

cell	Chapter	Colloid	Film thickness	electrolyte	IPCE/efficiency
L2	4	Solaronix HT	4 μm	L	IPCE = 45% at 510 nm.
L31	5 & 6	Dyesol	13.5 μm	H1	Not measured
E23	5 & 6	Dyesol	13.5 μm	H1	Not measured
E32	5 & 6	Dyesol	13.5 μm	H2	Not measured
12	5 & 6	Dyesol	13.5 μm	H2	Not measured
L11	5 & 6	Dyesol	13.5 μm	H3	Not measured
E22	5 & 6	Dyesol	13.5 μm	H3	Not measured
52	5 & 6	Dyesol	13.5 μm	H4	Not measured
S52	5 & 6	Dyesol	13.5 μm	H4	Not measured
S51	5 & 6	Dyesol	13.5 μm	H4	Not measured
E21	5 & 6	Dyesol	13.5 μm	J1	Not measured
E41	5 & 6	Dyesol	13.5 μm	J2	Not measured
Cell 5	6	Dyesol	13.5 μm	H2	Not measured

The IPCE and efficiency of the cells presented in Chapters 5 and 6 were not measured. However a cell made in the same way, with electrolyte H4 had a peak IPCE of 60 % and an efficiency of 2.9% at one Sun.

The Dyesol paste used was: DSC-18T NR

The electrolyte compositions are:

- Electrolyte L: 0.03M I_2, 0,6M propyl methyl imidazolium iodide, 0.5M tert-butyl pyridine, 0.1M guanidinium thiocyanate in 85:15 acetonitrile:valeronitrile

- Electrolyte H1: 0.5M LiI, 0.05M I_2 in 3-methoxy propionitrile
- Electrolyte H3: 0.1M LiI, 0.01M I_2 in 3-methoxy propionitrile
- Electrolyte H2: 0.5M LiI, 0.05M I_2 0.5M TBP in 3-methoxy propionitrile
- Electrolyte H4: 0.1M LiI, 0.01M I_2 0.5M TBP in 3-methoxy propionitrile
- Electrolyte J1: 0.5M LiI, 0.01M I_2 in 3-methoxy propionitrile
- Electrolyte J2: 0.5M LiI, 0.02M I_2 in 3-methoxy propionitrile